Chapter 1

Introduction

1.1 Glass Formation

Glass is a liquid that has lost its ability to flow, although structurally, the two states are indistinguishable. Upon cooling to temperatures below its melting point, a liquid can solidify as a crystal or form a glass. Thermodynamically, a periodic crystal has lower energy compared to glass. However, in some cases, the liquid atoms can easily assemble into non-crystalline packing modes, especially when the time available to form a periodic structure becomes a factor. A liquid cooled below its melting point does not crystallize spontaneously because of an activation barrier to nucleation which arises from the competition between volume and interfacial free energies. The level of undercooling depends on the height of the activation barrier. Figure 1.1 schematically shows the cooling curves for three different levels of undercooling. In case (a), the liquid undercools a little until nucleation is triggered and the liquid is raised to the melting temperature. This is followed by isothermal crystallization until all of the liquid is transformed into crystal. In case (b), the liquid is hypercooled, i.e., the amount of heat released is not enough to raise the sample to the melting temperature from such a deeply undercooled state. In the extreme case as shown by curve (c), the liquid bypasses crystallization completely and passes through glass transition, at which point it falls out of equilibrium and becomes solid-like. The glass transition temperature is not a constant

of the material, but rather is a function of experimental conditions. The slower the cooling rate, the lower will be the value of the glass transition temperature [1].

At the melting temperature, the first derivatives of the Gibbs free energy (such as volume, entropy, and enthalpy) are discontinuous. At the glass transition temperature, these thermodynamic variables are continuous but exhibit a change in slope, so there is discontinuity in their derivatives. These derivative quantities are defined as other important thermodynamic variables such as thermal expansion coefficient ($\alpha=\partial \ln V/\partial T$) and specific heat ($Cp=\partial H/\partial T$). The specific volume and specific heat as a function of temperature are shown schematically in Figure 1.2. If crystallization is suppressed, the liquid volume decreases until the atoms are frozen into position during glass transition. The thermal contraction of the glass is almost the same as the crystal because atomic rearrangement similar to the liquid cannot take place. Therefore the thermal expansion coefficients of the glass and the crystal are similar and smaller in value compared to the liquid as shown in Figure 1.2 (a). The specific heat of the undercooled liquid rapidly decreases from liquid-like values to crystal-like values. This abrupt change in specific heat as shown in Figure 1.2 (b) is regarded by most people as the signature of glass transition. Understanding the properties of undercooled liquid is key to understanding the glass formation process, recognized as one of the most challenging unsolved problems in solid state theory [2].

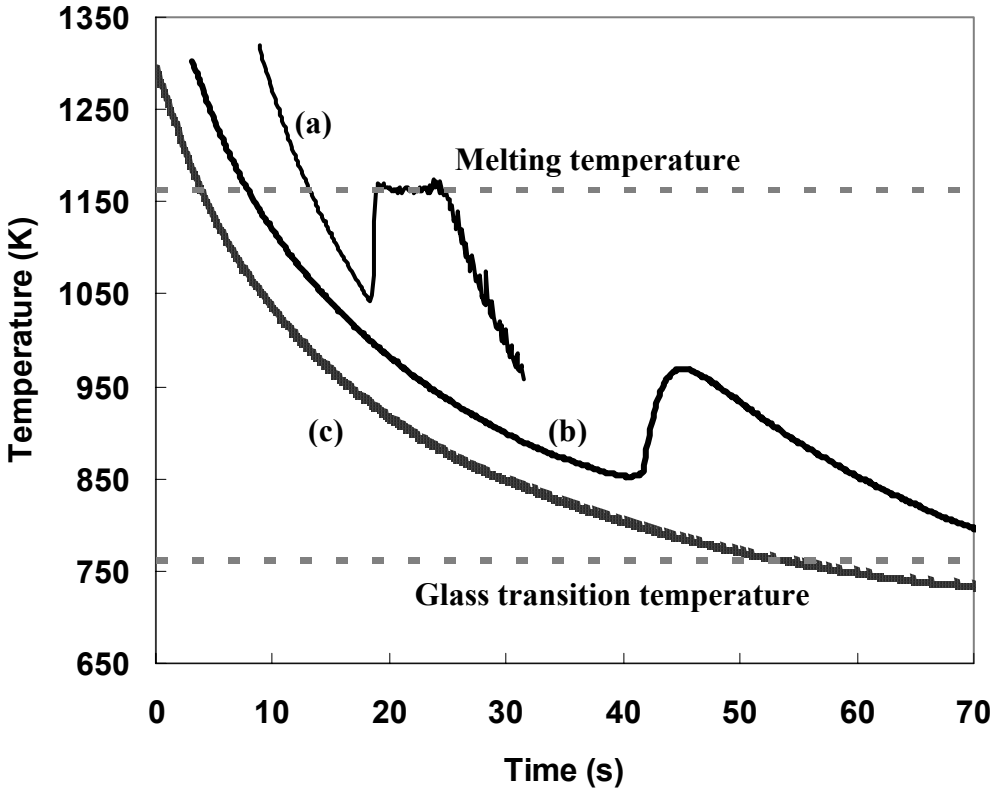

Figure 1.1: Cooling curves showing (a) undercooling followed by isothermal crystallization, (b) hypercooling, and (c) vitrification. The melting and glass transition temperatures are shown by the dotted lines.

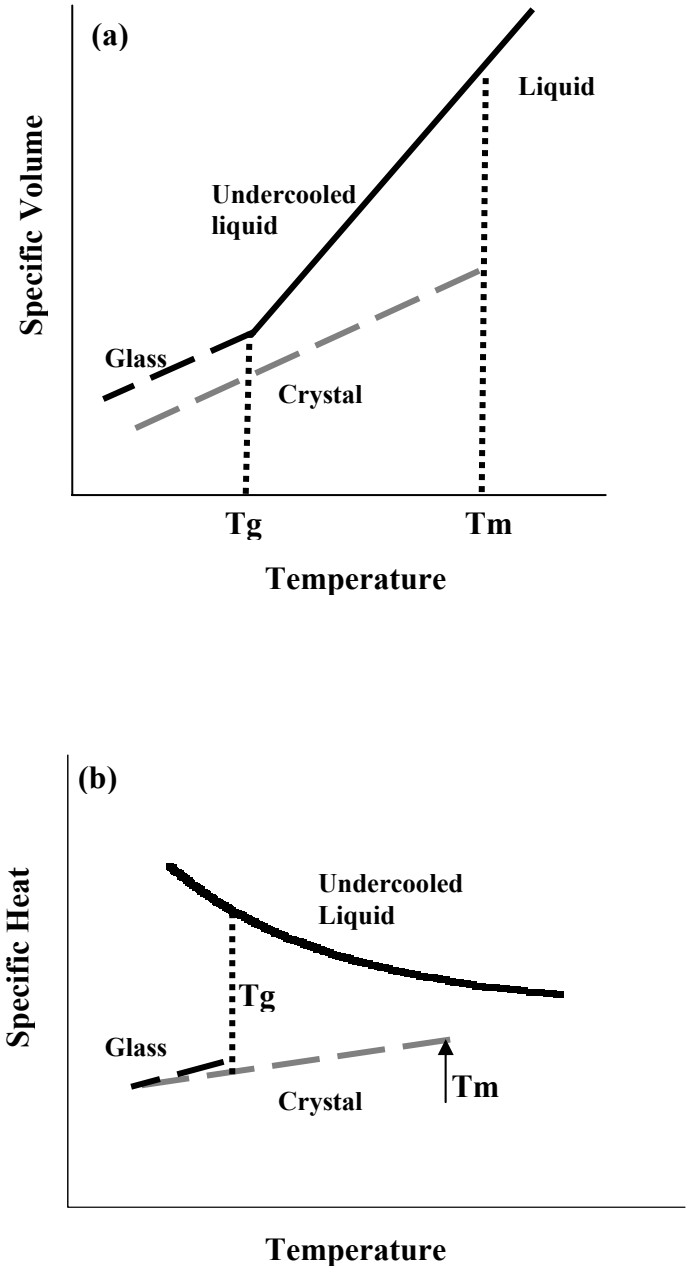

Figure 1.2: Dependence of (a) specific volume and (b) specific heat on temperature in the liquid, crystal and glass states.

1.2 Bulk Metallic Glasses

Turnbull demonstrated in the 1950s that deep undercooling could be achieved in a number of pure metals if heterogeneous nucleation is avoided [3]. In 1960, Klement, Willens, and Duwez [4] at Caltech first reported the vitrification of a binary metallic alloy by rapid quenching technique with a cooling rate of the order of 10^6 K/s. In the early 1970s, Chen and co-workers [5] used suction-casting techniques to form millimeter-diameter amorphous rods of Pd-Cu-Si with cooling rates of the order of 10^3 K/s. These are considered to be the first examples of bulk metallic glasses (BMGs). In the early 1990s, Inoue and his coworkers [6] found bulk glass forming compositions near deep eutectics in a number of systems such as La-Ni-Al, Mg-Cu-Y and Zr-Cu-Ni-Al. These alloy systems have critical cooling rates of 100 K/s. Building on the work of Inoue, Peker and Johnson [7] at Caltech discovered exceptional bulk glass formers in the Zr-Ti-Cu-Ni-Be system. A particular alloy in this system with composition $Zr_{41.2}Ti_{13.8}Cu_{12.5}Ni_{10}Be_{22.5}$ (Vit1) has a critical cooling rate of 1 K/s and has been extensively studied [7]. This alloy can be cast by conventional casting methods in the form of fully amorphous rods of diameter 5 to 10 cm, making it an attractive candidate for many structural applications. Other zirconium based bulk metallic glasses have been found recently in the Zr-Ti(Nb)-Cu-Ni-Al by Lin and Johnson [8]. Two notable compositions in these systems are $Zr_{57}Cu_{15.4}Ni_{12.6}Al_{10}Nb_5$ (Vit106) and $Zr_{52.5}Cu_{17.9}Ni_{14.6}Al_{10}Ti_5$ (Vit105), which can be cast as glassy ingots 1 cm thick. Structural applications of amorphous alloys were rather

limited until the development of bulk metallic glasses by Johnson at Caltech [7] and Inoue at Tohoku University [6].

Bulk metallic glasses have unique mechanical properties such as high strength, high elastic strain limit, and superior corrosion resistance which make them interesting as engineering materials [9]. Vit1 shows a tensile strength of 1.9 GPa, an elastic strain limit of 2% and plain strain fracture toughness, K_{1C}, in the range of 20 to 55 MPa $m^{1/2}$ [9]. The strength of the glassy alloys versus the elastic limit compared to other structural materials is shown in Figure 1.3. Since the elastic-strain limit of the metallic glasses exceeds 2%, the maximum stored elastic energy density is much more than useful crystalline metals. This property makes metallic glasses suitable for a number of applications in sporting equipment such as baseball bats and golf clubs, to name a few [9]. Bulk metallic glasses are also useful as kinetic energy penetrators due to their "self-sharpening" behavior.

Important limiting factors of BMGs in structural applications are their limited plasticity and tendency for shear localization. Plastic deformation in crystalline materials is achieved by the movement of dislocations that have definite slip systems. However, the lack of slip systems or other plastic deformation mechanisms in amorphous systems make them susceptible to shear localization and catastrophic failure. To overcome this problem, research efforts have been directed to the fabrication of metallic-glass composites. A variety of composite materials have been fabricated by direct introduction of a reinforcing crystalline solid into a glass forming melt [10,11] as well as by nucleation of an *in situ* ductile phase in an amorphous matrix [12,13]. These composites show much higher toughness and ductility compared to the monolithic BMGs [10-13].

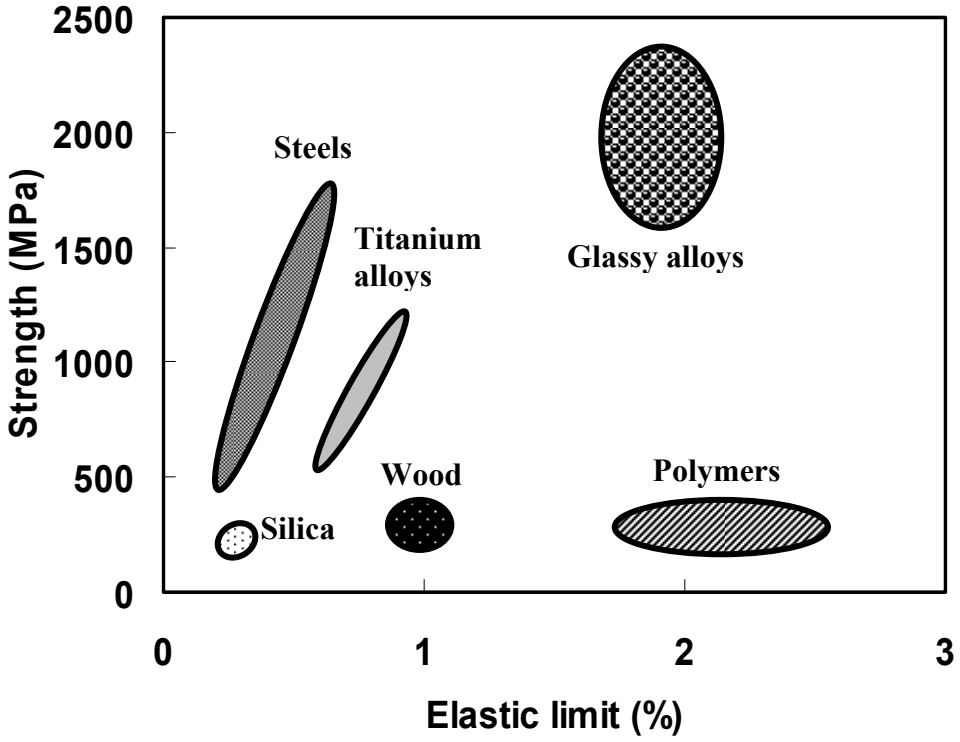

Figure 1.3: Strength versus elastic limit of glassy alloys compared to other structural materials.

1.3 Motivation and Objectives

The search for new and improved bulk metallic glass (BMG) forming alloys continues at an ever-increasing pace as more engineering applications are identified for this novel class of materials. To aid in this search, much effort has been directed towards understanding the correlations between the thermophysical properties of these complex multi-component systems and their glass forming ability (GFA). Earlier studies involving simple binary alloys (e.g., Au-Si [4]) which required very high cooling rates (10^5-10^6 K/s) to form glass, have paved the way for higher order systems with exceptional glass forming ability, that can be vitrified by cooling rates of the order of 1 K/s [6-9]. Earlier, Turnbull [14] predicted that the ratio of glass transition temperature to the melting temperature of a good glass former should be around 2/3, and this has led to the search of glass forming compositions close to deep eutectics. However, identification of comprehensive predictive indicators of glass forming ability based on thermodynamic and kinetic studies will greatly aid in the systematic search for new glass forming compositions.

The exceptional stability against crystallization of bulk glass forming melts has provided a unique opportunity to study their thermophysical properties in the deeply undercooled state. Some of the thermodynamic and kinetic studies that have been done in the past include specific heat [15-17], Gibbs free energy difference between liquid and crystal [17-19], viscosity [1,20,21], atomic diffusion coefficient [20,22], and specific volume [23,24]. However, most of these studies are limited to the temperature range

close to glass-transition. There is limited data at high temperatures mainly because these glass forming systems consist of highly reactive elements such as Ni, Ti and Zr which limit the applicability of conventional measurement techniques [25]. Therefore, no systematic study involving high temperature thermophysical properties has been carried out to date. Nonetheless, comparative studies of thermophysical properties at high-temperatures for a wide spectrum of glass formers is of utmost importance in assessing the glass forming trend of existing BMGs, as well as for developing new alloy systems.

The glass forming ability of a BMG is quantified by the critical cooling rate to bypass crystallization upon cooling from the stable melt. This can be measured from the time-temperature-transformation (TTT) curve of the alloy which describes the transformation kinetics from undercooled liquid to crystal in an isothermal experiment. The TTT curves for two of the best known bulk metallic glass formers, $Zr_{41.2}Ti_{13.8}Cu_{12.5}Ni_{10}Be_{22.5}$ (Vit1) [26] and $Pd_{43}Ni_{10}Cu_{27}P_{20}$ [27], have been obtained earlier. Though these studies provided remarkable insights into their crystallization behavior, no attempts have been made to correlate the thermophysical properties with the crystallization time scales. Such studies would require the simultaneous measurement of TTT curves and thermophysical properties for a number of BMGs. Moreover, it is critical to identify the heterogeneous influences on TTT curves to understand the intrinsic crystallization behavior and optimize processing conditions. There are only a limited number of studies in this regard.

High vacuum containerless measurement techniques are ideal for investigating TTT curves and thermophysical properties of BMGs, particularly at high temperatures because there is no risk of reaction with container walls. However, there are only a

limited number of studies [23,26] involving bulk metallic glasses that have been carried out utilizing the unique advantages of containerless techniques. Deep undercooling of the melt can be achieved by containerless processing because heterogeneous nucleation induced by container walls or environment can be eliminated altogether. In particular, the high vacuum electrostatic levitation (HVESL) technique developed by Rhim *et al.* [28] has several advantages over other containerless measurement methods. The principles behind the working of the electrostatic levitator and its advantages are discussed in detail in chapter 2 of this thesis.

The main objectives of this thesis are identification of reliable predictive indicators of glass forming ability based on measurement of thermophysical properties at high temperatures, and the study of intrinsic crystallization behavior of bulk metallic glasses using the electrostatic levitation technique. The study of thermophysical properties includes the measurement and characterization of both kinetic and thermodynamic quantities that affect glass forming ability. To probe the intrinsic crystallization behavior, it is necessary to identify and eliminate the heterogeneous influences on crystallization. The BMGs are chosen from a wide spectrum consisting of very good glass formers as well as poor glass formers.

1.4 Thesis Overview and Key Contributions

The kinetic properties, thermodynamic properties, and intrinsic crystallization behavior for a number of bulk metallic amorphous alloys having widely different glass forming abilities are investigated in this thesis. The measurements are carried out using

the high vacuum electrostatic levitation technique to avoid any heterogeneous nucleation effects from container walls or environment. The principles behind the working of the electrostatic levitator, its advantages, and the noncontact diagnostic techniques are discussed in chapter 2.

The trends in glass formation among five bulk metallic glass forming alloys are investigated within the framework of their measured kinetic and thermodynamic properties which are discussed in chapter 3. The melting temperature viscosity, fragility parameter, and volume change upon crystallization are identified as reliable indicators of glass forming ability based on the study of kinetic properties. The surface tensions of these alloys are measured for the first time and are found in most cases to follow proportional mathematical addition of the surface tension of pure components. The experimentally measured entropies of fusion for a wide range of glass formers show that thermodynamic driving force may not be significant in determining the glass forming ability of these alloys. The specific heat and total hemispherical emissivity obtained from the free radiative cooling curve and sample volume measurement are also discussed.

A pronounced influence of overheating is observed on the undercooling behavior and crystallization time scales of bulk metallic glasses. This overheating effect and its influence on Time-Temperature-Transformation (TTT) curves of the glass forming alloys are discussed in chapter 4. A threshold overheating temperature is found for each alloy, above which there is a drastic increase in the undercooling level and the crystallization times. TTT diagrams are measured for the alloys by overheating above their respective threshold temperatures and are found to be very similar in shape, suggesting that system-specific properties do not play a crucial role in defining crystallization kinetics in these

alloys. The possible mechanisms behind this are also discussed in chapter 4. These TTT curves are important from a practical standpoint because they provide the time-temperature window for commercial processing.

The Time-Temperature-Transformation (TTT) diagrams for novel ternary Zr-Al-Co bulk metallic glasses are measured for the first time over a wide temperature range between their glass transition and melting temperatures, and are discussed in chapter 5. Change in crystallization behavior due to the addition of a small amount of Cu is also investigated. To assist in understanding the crystallization pathways, X-ray diffraction studies are carried out for the alloys after isothermal crystallization at different undercooling levels.

Chapter 6 deals with quantitative correlation between crystal-melt interfacial tension, melt viscosity, and glass forming ability. The TTT diagrams for three alloys are analyzed within the framework of nucleation theory and the crystal-melt interfacial tensions are obtained by fitting of the TTT curves. These alloys are chosen because of their widely different glass forming abilities but otherwise similar properties. The times for crystallization in these alloys are found to scale with the melt viscosities. The influence of icosahedral short-range order of the undercooled liquid on viscosity and interfacial tension are discussed.

The crystallization behavior, microstructure, specific volume, and viscosity of an *in situ* ductile phase reinforced amorphous matrix composite are investigated as a function of the processing temperature and compared with a monolithic BMG in chapter 7. Based on the experimental results, an optimum processing route is suggested.

1.5 References

[1] R. Busch, E. Bakke, and W. L. Johnson, Acta Mater. **46**, 4725 (1998).

[2] P. W. Anderson, Science **267**, 1615 (1995).

[3] D. Turnbull and R. E. Cech, J. Appl. Phys. **21**, 804 (1950).

[4] W. Clement, R. H. Willens, and P. Duwez, Nature **187**, 869 (1960).

[5] H. S. Chen and D. Turnbull, Acta Metall. **17**, 1021 (1969).

[6] A. Inoue, T. Zhang, and T. Masumoto, Mater. Trans. JIM **31**, 177 (1990).

[7] A. Peker and W. L. Johnson, Appl. Phys. Lett. **63**, 2342 (1993).

[8] X. H. Lin and W. L. Johnson, J. Appl. Phys. **78**, 6514 (1995).

[9] W. L. Johnson, MRS Bulletin **10**, 42 (1999).

[10] H. C.-Yim and W. L. Johnson, Appl. Phys. Lett. **71**, 3808 (1997).

[11] R. D. Conner, R. B. Dandliker, and W. L. Johnson, Acta Mater. **46**, 6089 (1998).

[12] C. C. Hays, C. P. Kim, and W. L. Johnson, Phys. Rev. Lett. **84**, 2901 (2000).

[13] C. P. Kim, Ph.D. Thesis, California Institute of Technology (2001).

[14] D. Turnbull, Contemp. Phys. **473**, 10 (1969).

[15] R. Busch and W. L. Johnson, Appl. Phys. Lett. **72**, 2695 (1998).

[16] I.-R. Lu, G. Wilde, G. P. Gorler, and R. Willnecker, J. Non-Cryst. Solids **250-252**, 577 (1999).

[17] Z. P. Lu, X. Hu, and Y. Li, Intermetallics **8**, 477 (2000).

[18] S. C. Glade, R. Busch, D. S. Lee, W. L. Johnson, R. K. Wunderlich, and H. J. Fecht, J. Appl. Phys. **87**, 7242 (2000).

[19] R. Busch, Y. J. Kim, and W. L. Johnson, J. Appl. Phys. **77**, 4039 (1995).

[20] A. Masuhr, T. A. Waniuk, R. Busch, and W. L. Johnson, Phys. Rev. Lett. **82**, 2290 (1999).

[21] Y. Kawamura and A. Inoue, Appl. Phys. Lett. 77, 1114 (2000).

[22] U. Geyer, S. Schneider, W. L. Johnson, Y. Qiu, T. A. Tombrello, and M. P. Macht, Phys. Rev. Lett. **75**, 2364 (1995).

[23] K. Ohsaka, S. K. Chung, W. K. Rhim, A. Peker, D. Scruggs, and W. L. Johnson, Appl. Phys. Lett. **70**, 726 (1997).

[24] I. R. Lu, G. P. Gorler, and R. Willnecker, Appl. Phys. Lett. **80**, 4534 (2002).

[25] T. Iida and R. I. L. Guthrie, *The Physical Properties of Liquid Metals* (Clarendon, Oxford; 1988).

[26] Y. J. Kim, R. Busch, W. L. Johnson, A. J. Rulison, and W. K. Rhim, Appl. Phys. Lett. **68**, 1057 (1996).

[27] J. Schroers, Y. Wu, R. Busch, and W. L. Johnson, Acta Mater. **49**, 2773 (2001).

[28] W. K. Rhim, S. K. Chung, D. Barber, K. F. Man, G. Gutt, A. Rulison, and R. E. Spjut, Rev. Sci. Instrum. **64**, 2961 (1993).

Chapter 2

Experimental Approach: Electrostatic Levitator and Noncontact Diagnostic Techniques

2.1 Introduction

Investigation of liquid thermophysical properties by containerless measurement techniques enables the observation of intrinsic behavior because of the removal of the disturbing influences of container walls and impurities. Numerous types of levitators have been developed [1] which include acoustic [2], aero-acoustic [3], electromagnetic [4], electrodynamic [5], and electrostatic levitators [6], each having its own unique capabilities. In particular, the high-vacuum electrostatic levitation (HVESL) technique developed by Rhim *et al.* [6] has several advantages over other containerless measurement methods: (i) sample heating and levitation are decoupled, thus allowing the sample temperature to be varied over a wide range; (ii) the feedback control provides quiescent sample positioning; and (iii) there is no severe distortion of the liquid drop as is common in electromagnetic levitation, thus allowing accurate volume measurement. The HVESL can be employed for obtaining viscosity and surface tension of the melt simultaneously using the drop oscillation technique, described later in detail. By this technique, both the surface tension and viscosity can be obtained from a single transient signal, thereby eliminating uncertainties introduced from different measurement techniques. Also, a single axisymmetric mode can be excited in an almost spherical

sample, making the data analysis unambiguous. Because all of the heating sources can be blocked without affecting sample levitation, the specific heat over total hemispherical emissivity can be obtained from the free radiative cooling curve and volume of the sample.

In this investigation, the electrostatic levitation technique was used for the measurement and characterization of crystallization behavior and thermophysical properties of bulk metallic glasses. The unique advantages of this technique outlined above allowed the measurements to be carried out in the deep undercooled liquid state. Moreover, this enabled the probing of intrinsic behavior because there was no risk of contamination or chemical reaction. The principles, hardware, and the diagnostic techniques involved in this method are discussed in the following sections.

2.2 Levitation Principles and Hardware

In High Vacuum Electrostatic Levitator (HVESL) [6], a sample (sphere ~ 2 mm diameter) is levitated between a pair of parallel-disk electrodes spaced about 10 mm apart. According to Earnshaw's theorem [7], there is no three-dimensional electrostatic potential minimum. So in an electrostatic levitator, the sample is positioned through active feedback-controlled electrostatic fields that are generated using properly positioned electrodes. A schematic diagram of the High Vacuum Electrostatic Levitator is shown in Figure 2.1. The electrode assembly is housed in a stainless steel vacuum chamber which is evacuated to 10^{-8} torr. The vacuum system used to achieve this high level of vacuum consists of a roughing diaphragm pump, a turbo-molecular pump, and a

getter pump. Two orthogonal He-Ne lasers, together with two position detectors, provide the three-dimensional position information that is used by a computer to generate the feedback signal. The schematic of the electrode assembly is shown in Figure 2.2. The assembly consists of a top electrode, a bottom electrode and two pairs of side electrodes. The top and bottom electrodes provide vertical positioning, while the side electrodes are placed orthogonally for lateral positioning of the sample. The bottom electrode is connected to a high voltage amplifier which generates an oscillating electric field to induce drop oscillation for viscosity and surface tension measurement.

Three sample-charging methods are employed for electrostatic positioning of the sample: capacitive, photoelectric and thermionic. Capacitive charging is used for launching the sample by increasing the top electrode potential until the electrical contact of the sample with the bottom electrode is broken. A 1 kW UV-rich xenon arc lamp provides initial photoelectric charging and heating. This is followed by heating with a continuous wave (CW) Nd-YAG laser operating at 1.064 μm with maximum output power of 200 W. By splitting the YAG laser beam into four beams of equal intensity in a tetrahedral arrangement, the temperature gradient in the sample is greatly reduced (Figure 2.2). The maximum temperature difference on the sample surface for the four-beam configuration is estimated to be less than 1K for a sample temperature of around 1000 K. At close to the melting temperature, thermionic emission from the sample becomes the dominant charging mechanism and the desired temperature is achieved by using just the YAG laser while the xenon lamp is completely turned off. The temperature is measured remotely using a two-color pyrometer with a nominal sensitivity range of 650-1650 K. A detailed description of the ESL facility is given in an earlier publication [6].

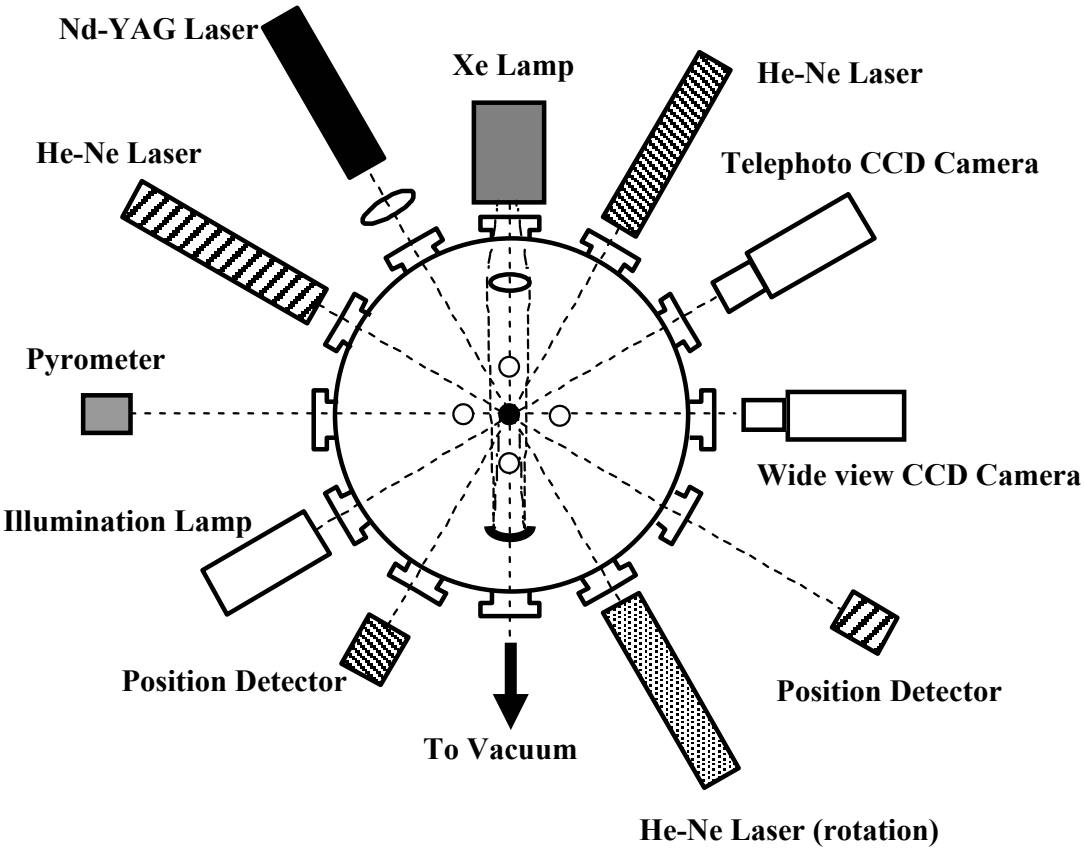

Figure 2.1: Schematic diagram of the High Vacuum Electrostatic Levitator (HVESL) showing the different components.

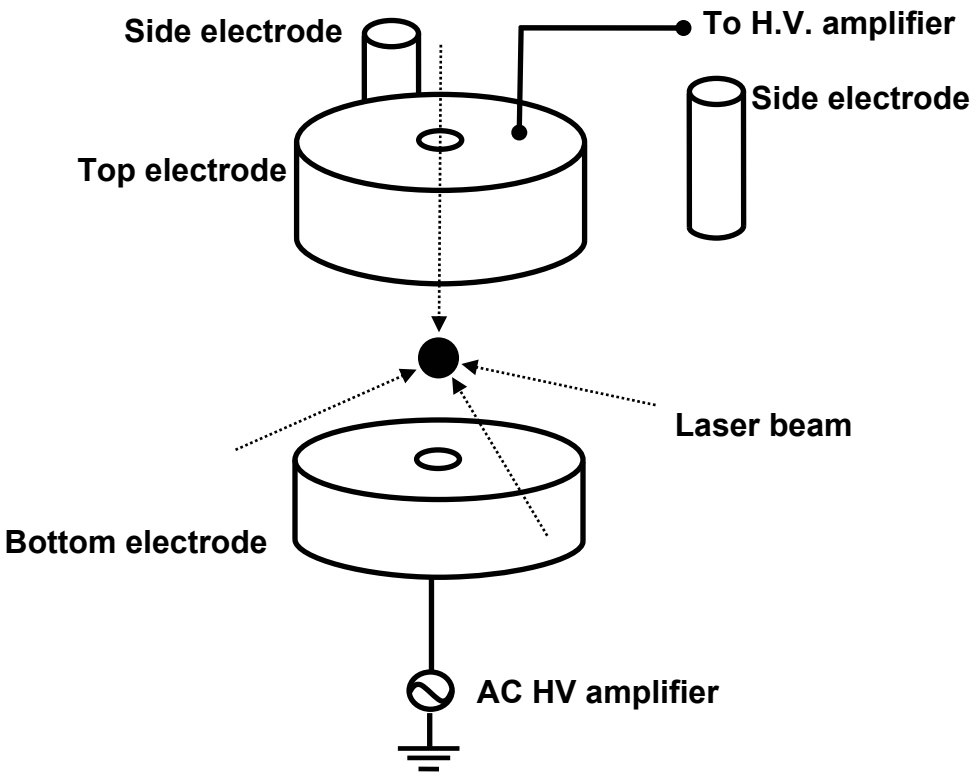

Figure 2.2: Schematic diagram of the electrode assembly showing tetrahedral laser heating arrangement. The top and bottom electrodes control the sample position along the vertical direction, while the two orthogonal side electrodes around the top electrode control the sample position in the horizontal directions. The bottom electrode is connected to a high-voltage amplifier which generates an oscillating electric field to induce drop oscillation.

2.3 Noncontact Diagnostic Techniques to Measure Thermophysical Properties

2.3.1 Specific Volume Measurement by Image Capture and Digitization

The sample images are captured by a charge coupled device (CCD) video camera with a telescopic head. The sample image for one of the alloys is shown in Figure 2.3. The edge points of the sample images are fitted with Legendre polynomials through sixth order. Finally the sample volumes are obtained by calibrating with stainless steel spheres of known volume. The specific volume (V_{SP}) and thermal expansion coefficient (α) are calculated from the known sample mass (M) and volume (V) as:

$$V_{SP} = \frac{V}{M} \tag{2.1}$$

$$\alpha = \frac{1}{V}\frac{\partial V}{\partial T}. \tag{2.2}$$

A UV-rich halogen lamp for background illumination and a UV-passing filter placed before the camera reduce the camera blooming effect at high temperatures. The detailed volume measurement technique is described elsewhere [8].

2.3.2 Viscosity and Surface Tension Measurement by Drop Oscillation Technique

To measure the viscosity and surface tension, drop oscillations are induced by applying alternating current (AC) voltage to the bottom electrode. The electrode assembly, being axially symmetric, can effectively excite n=2 mode. The levitated drop is backlit by a collimated laser beam, and a photodetector with a narrow slit placed before it

detects signal that is sensitive to the oscillating drop amplitude. An excitation pulse consisting of a given number of sine-wave cycles is applied at the resonant frequency of the drop and the ensuing transient signal is recorded. A typical transient signal obtained by such a process is shown in Figure 2.4. The high-pass filtered data in the time domain along with the Fast Fourier Transform (FFT) based spectrum are used for analysis. The data are assumed to follow the function:

$$y = Ae^{-t/\tau}\sin\left(2\pi ft + \phi\right), \tag{2.3}$$

where A is the amplitude, t is the time, τ is the decay time constant, f is the resonant frequency, and ϕ is a constant phase factor. The decay time and frequency are obtained by fitting the signal with this equation.

Viscosity (η) of the liquid drop is calculated from the decay time constant (τ) of free oscillation that follows the excitation pulse and is given as [9,10]:

$$\eta = \frac{\rho r^2}{5\tau}, \tag{2.4}$$

where, ρ is the density and r is the radius of the spherical drop. Surface tension (σ) of the oscillating liquid drop is calculated from its resonant oscillation frequency ($\omega=2\pi f$) [11]:

$$\sigma = \frac{\omega^2 \rho r^3}{8}, \tag{2.5}$$

where, ρ is the density and r is the radius of the liquid drop. This value of surface tension is corrected to take into account the charge distribution on the sample surface and the non-sphericity in sample shape [10]. A detailed description of the viscosity and surface tension measurement technique is given elsewhere [10].

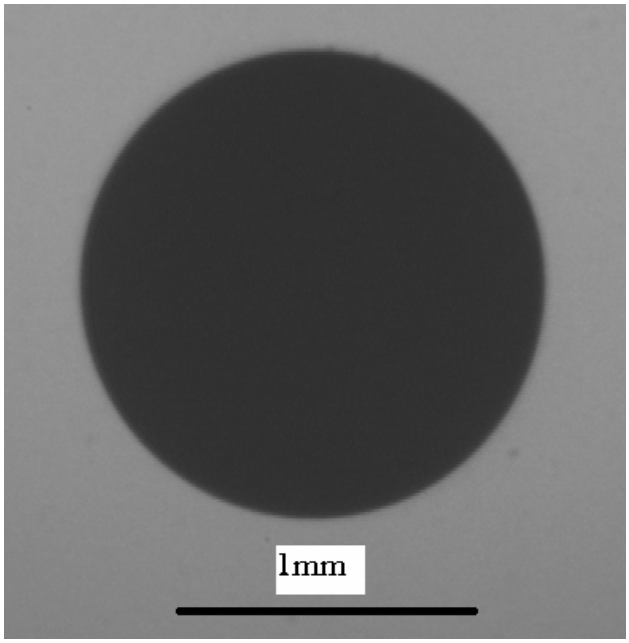

Figure 2.3: A typical side view of a levitated molten sample from which the specific volume is extracted by Legendre polynomial fitting.

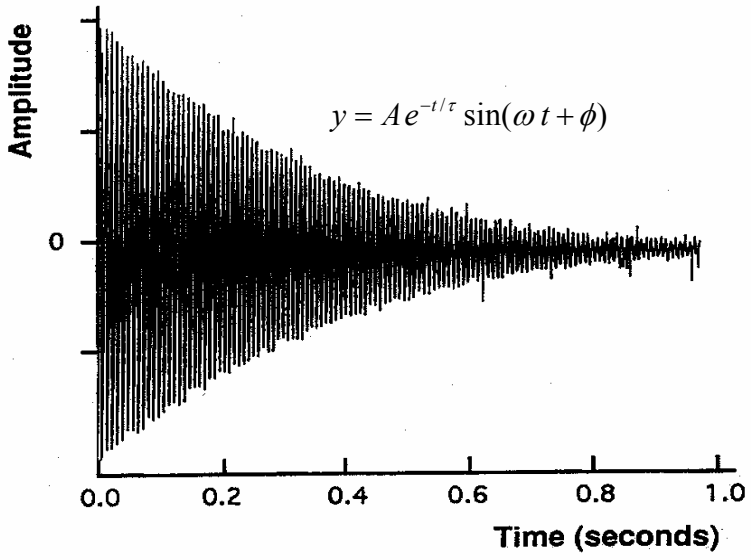

Figure 2.4: Typical transient oscillation of a levitated drop. The signal is fitted with a function which is the product of a decaying exponential and a sinusoidal wave.

2.3.3 Specific Heat and Total Hemispherical Emissivity

In the ESL, heating and levitation are decoupled. Therefore, when all the heating sources are blocked, the sample cools from high temperature in a purely radiative way following the heat transfer equation:

$$\frac{m}{M} C_P \frac{dT}{dt} = -\sigma_{SB} \varepsilon_T A (T^4 - T_S^4), \tag{2.6}$$

where m is the sample mass, M is the molecular weight, C_P is the constant pressure specific heat, T is the sample temperature, T_S is the ambient temperature, σ_{SB} is the Stefan-Boltzmann constant (5.6705×10^{-8} W·m^{-2}·K^{-4}), A is the surface area of the sample, and ε_T is the total hemispherical emissivity. This can be rewritten as:

$$\frac{C_P}{\varepsilon_T} = -\frac{\sigma_{SB} A (T^4 - T_S^4)}{\frac{m}{M}\frac{dT}{dt}}. \tag{2.7}$$

Since all the parameters on the right hand side of the equation can be determined from temperature and volume measurements, C_P/ε_T can be obtained. This equation is the basis for determining the specific heat by the ESL technique if the total hemispherical emissivity is known, and vice-versa [12].

2.3.4 Measurement of Time-Temperature-Transformation Curves

To investigate crystallization behavior, samples are levitated and melted using a Nd-YAG laser. For undercooling experiments, the samples are allowed to free cool in vacuum from the molten state by turning off the laser. Free cooling vitrifies some of the good glass formers. However, the poor glass formers crystallize at a certain level of

undercooling as observed by recalescence - the sharp rise in temperature due to the release of the latent heat of fusion. Isothermal experiments are performed to determine the TTT diagram. The molten sample is cooled to a predetermined temperature by turning off the laser which is subsequently turned back on at a preset power to maintain an isothermal temperature. Figure 2.5 shows a cooling curve obtained by free radiative cooling of a sample in the ESL. There is no heat release event during the entire cooling process and the sample vitrifies. The schedule of constructing a TTT diagram is also shown in Figure 2.5. Prior to each isothermal measurement, the alloy is subjected to melting and radiative cooling to ensure proper fluxing. The overheating has a pronounced influence on the undercooling behavior and crystallization time scales [13]. The TTT curve gives a summary of time for crystallization after isothermal annealing at different temperatures. The starting of the isothermal anneal time at each temperature is used as the time origin (t=0) for the TTT curves. The temperature is monitored using a two-color pyrometer. The temperature fluctuations are within ±2 K during the isothermal treatment for the TTT curve measurement.

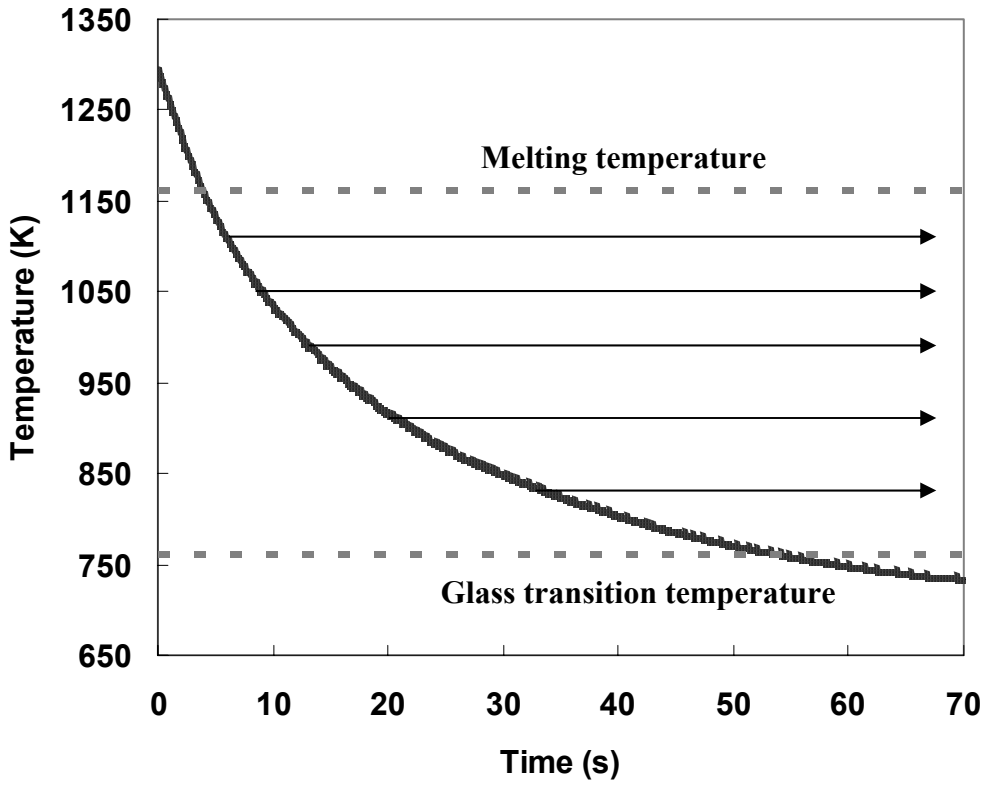

Figure 2.5: Free radiative cooling in the ESL showing glass formation. The schedules for isothermal measurements to determine a TTT diagram are shown by arrows in the plot.

2.4 References

[1] E. H. Brandt, Science **243**, 349 (1989).

[2] Y. Tian, R. G. Holt, and R. E. Apfel, Rev. Sci. Instrum. **66**, 3349 (1995).

[3] J. K. R. Weber, D. S. Hampton, D. R. Merkley, C. A. Rey, M. M. Zatarski, and P. C. Nordine, Rev. Sci. Instrum. **65**, 456 (1994).

[4] J. Szekely, E. Schwartz, and R. Hyers, J. Metals 47, 50 (1995).

[5] *Aerosol Measurement*, edited by K. Willeke and P. A. Baron (Van Nostrand Reinhold, New York, 1993).

[6] W. K. Rhim, S. K. Chung, D. Barber, K. F. Man, G. Gutt, A. Rulison, and R. E. Spjut, Rev. Sci. Instrum. **64**, 2961 (1993).

[7] S. A. Stratton, *Electromagnetic Theory*, McGraw-Hill, New York, 1941.

[8] S. K. Chung, D. B. Thiessen, and W. K. Rhim, Rev. Sci. Instrum. **67**, 3175 (1996).

[9] H. Lamb, *Hydrodynamics*, 6th ed., Cambridge University Press, Cambridge, 1932.

[10] W. K. Rhim, K. Ohsaka, P.-F. Paradis, and R. E. Spjut, Rev. Sci. Instrum. **70**, 2796 (1999).

[11] J. W. S. Rayleigh, Phil. Mag. **14**, 184 (1882).

[12] A. J. Rulison, and W. K. Rhim, Rev. Sci. Instrum. **65**, 695 (1994).

[13] S. Mukherjee, Z. Zhou, J. Schroers, W. L. Johnson, and W. K. Rhim, Appl. Phys. Lett. **84**, 5010 (2004).

Chapter 3

Influence of Kinetic and Thermodynamic Properties on Glass Forming Ability

Abstract

The trends in glass formation among bulk metallic glass forming alloys of widely differing glass forming abilities are investigated within the framework of their measured kinetic and thermodynamic properties. The kinetic properties, viscosity and free volume, are found to have the most definite influence on their glass forming ability. On the other hand the thermodynamics do not play a major role. The glass forming melts show orders of magnitude higher viscosity compared to pure metals. Among the glass forming alloys, the better glass former has higher melting-temperature viscosity, higher fragility, and shows a smaller change in volume upon crystallization compared to a poorer glass former. The experimentally measured entropies of fusion for a wide range of glass-formers are almost similar, indicating that thermodynamic driving force may not be significant in determining the glass-forming ability of these alloys. The other measured thermophysical properties, surface tension and specific heat, do not show any strong correlation with glass forming ability.

Keywords: Bulk metallic glass; Viscosity; Specific volume; Free Volume; Surface tension; Specific heat; Entropy of fusion

3.1 Introduction

The kinetic properties that are important in the study of metallic glasses include specific volume and viscosity. The study of volume change of the atoms, as well as the associated unoccupied free volume with temperature, is of utmost importance because a small variation in the free volume can induce large changes in the flow behavior [1]. Measurement of specific volume for alloys and comparison with an ideal mixture of the constituents gives an indication of the nature of interaction between the constituent elements. Viscosity is a kinetic parameter that describes the time scale for structural rearrangement of the liquid atoms in an undercooled state to form a crystal nucleus. Thus, viscosity determines the crystallization kinetics of an undercooled melt and has special significance in the study of glass forming systems. Moreover, study of the strong-fragile behavior [2] of bulk metallic glass (BMG) melts is critical in understanding the factors affecting glass forming ability. Although viscosity data close to the glass transition region exists for quite a few BMGs, only a limited amount of data is available for the high temperature region. Viscosity data around the melting temperature of a BMG is much more difficult to obtain because these glass forming systems consist of highly reactive elements such as Ni, Ti and Zr that limit the applicability of conventional methods. Sophisticated custom-made equipment [3,4], as well as levitation experiments [5], were used to explore the viscosity in the region around the melting temperature. Because of limited viscosity data close to the melting point, no systematic study involving high temperature viscosity has been reported for BMGs with different glass forming ability

(GFA). From a practical standpoint, the measurement of both high temperature viscosity and specific volume are important for optimization of processing conditions such as in casting and composite infiltration.

Surface tension is another important thermophysical property that is vital in understanding the nature of liquids. While viscosity portrays the bulk characteristics of the melt, surface tension gives information about the surface. Particularly, the surface tension of alloys is vital for studying segregation effects and the extent of Marangoni flow which is important for diffusion studies [6]. A number of phenomenological models have been proposed to estimate the surface tension for liquid metals from their viscosity. Reasonable agreement has been found with experiments for pure metals [7]. These models have been used to estimate the surface tension of alloys where they could not be measured directly [8] without testing the validity of extending them to multi-component systems. These estimates for multi-component systems may be misleading, and this necessitates the experimental determination of reliable surface tension data for alloys and investigation of their correlation with viscosity. Although surface tension data for pure metals is available in the literature [7], they are scarce for binary alloys, and in the case of complex glass forming systems, a nearly complete lack of data is evident.

Knowledge of specific heat is required for quantitative evaluation of the thermodynamic driving force for crystallization. Thus it has special significance in the study of glass forming systems. The driving force for crystallization can be approximated by the Gibbs free energy difference (ΔG) between the supercooled liquid and crystal. ΔG can be calculated from the enthalpy of fusion and the difference in specific heat (ΔC_P) between the supercooled liquid and crystal.

In this chapter, the influences of kinetic and thermodynamic properties on glass forming ability are investigated. For this purpose, five bulk amorphous alloys with widely differing glass forming abilities were chosen. The kinetic properties studied are viscosity and specific volume. The glass forming alloys are classified according to their strong-fragile behavior [2] of viscosity. The correlations between surface tension and viscosity of bulk metallic glasses are explored and compared with pure metals. To investigate the thermodynamics, specific heat and entropy of fusion are measured and their role in the glass formation process is discussed. All of the measurements are made using the electrostatic levitation technique to avoid heterogeneous influences of containers.

3.2 Experimental Details

In this study, alloy systems were chosen that have widely differing glass forming abilities. This makes them suitable for a comparative study and helps in identifying the influence of thermophysical properties on their glass forming ability. The alloys investigated in order of decreasing glass forming ability are: $Zr_{41.2}Ti_{13.8}Cu_{12.5}Ni_{10}Be_{22.5}$ (Vit1), $Zr_{57}Cu_{15.4}Ni_{12.6}Al_{10}Nb_5$ (Vit106), $Zr_{55}Al_{20}Co_{25}$ (ZrAlCo), $Zr_{52.5}Cu_{17.9}Ni_{14.6}Al_{10}Ti_5$ (Vit105), and $Ni_{59.5}Nb_{40.5}$ eutectic alloy (NiNb). The samples were prepared from high purity starting materials in an arc-melter. The glass transition temperatures (T_g), and the liquidus temperatures (T_L) were obtained for the alloys by heating with a rate of 0.33 Ks^{-1} in a Differential Scanning Calorimeter (DSC). The T_g, T_L, and T_g/T_L values for the alloys investigated in this study are summarized in Table 3.1.

Table 3.1: Characteristic temperatures and critical cooling rates

BMG	T_g (K)	T_L (K)	T_g/T_L	$\Delta T/T_L$ (%)	Rc (K s^{-1})
Vit1	620	993	0.624	Vitrified	2*
Vit106	682	1115	0.612	Vitrified	10*
ZrAlCo	753	1323	0.569	Vitrified	17*
Vit105	675	1090	0.619	21	25#
NiNb	920	1448	0.635	9	250#

* Measured from TTT curve
# Estimated from the critical casting thickness to form fully amorphous plates

Typical free radiative cooling curves obtained for the five alloys are shown in Figure 3.1. Vit1, Vit106, and ZrAlCo could be vitrified by free cooling in the ESL, while Vit105 and NiNb eutectic alloy crystallized after a certain degree of undercooling. The maximum undercooling achieved for Vit105 was 230 K, and that for the NiNb eutectic alloy was 130 K. The maximum undercooling as a percentage of the liquidus temperature ($\Delta T/T_L$) and the critical cooling rates to vitrify (Rc) the samples are shown in Table 3.1. The critical cooling rates vary more than two orders of magnitude for the five alloys, indicating their widely differing glass forming abilities. Vit1 is the best glass former and NiNb is the worst among the five alloys investigated. The critical cooling rates for Vit1, Vit106, and ZrAlCo were measured from their respective time-temperature-transformation (TTT) curves [9,10] and will be discussed later, while those of Vit105 and NiNb were estimated from critical casting thickness to form fully amorphous plates [11,12]. The details of measurement techniques for the different thermophysical properties are discussed in chapter 2. The trends in glass formation are analyzed within the framework of the measured thermophysical properties.

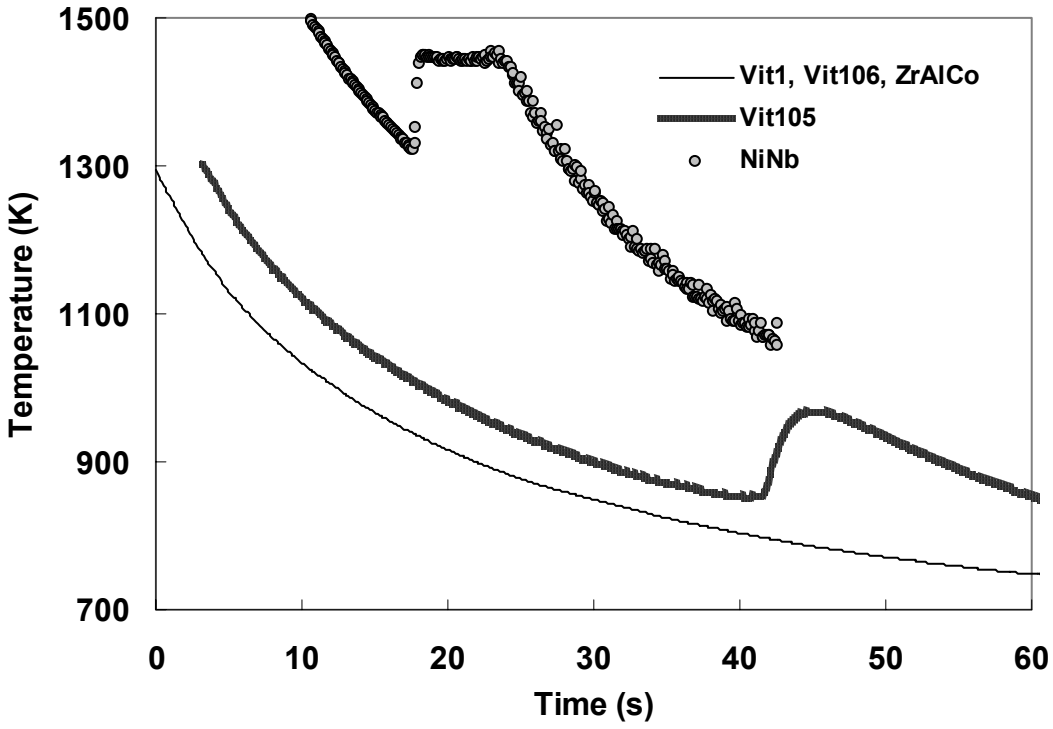

Figure 3.1: Free radiative cooling curves for Vit1, Vit106, ZrAlCo, Vit105, and NiNb. Vit1, Vit106, and ZrAlCo could be vitrified by free radiative cooling in the ESL. However, Vit105 and NiNb crystallized after certain undercooling.

3.3 Results and Discussion

3.3.1 Specific volume

The simultaneously measured specific volume and cooling curve for one of the alloys, Vit105, are shown in Figure 3.2. On the temperature-time curve, crystallization is evidenced by recalescence - the sharp rise in temperature due to the release of the latent heat of fusion. However, at this large undercooling, the heat released during recalescence is insufficient to raise the sample to the melting temperature. On the volume-time curve, crystallization is evidenced by the discontinuous decreases in the sample volume. The noise level in the volume data for the crystal is about twice that of the liquid due to slight deformation of the sample upon crystallization. The liquid and crystal specific volumes can be extracted separately and plotted as a function of temperature. For alloys that vitrified upon free radiative cooling, crystalline specific volume was measured after the sample was crystallized entirely by heating it up from glass transition temperature.

The liquid and crystal specific volumes plotted as a function of temperature are shown in Figure 3.3 for one of the alloys (ZrAlCo) that could be vitrified by free radiative cooling in the ESL. The measurement accuracy as shown for ZrAlCo is representative of the results for all other alloys obtained in this study. The measurement accuracy of liquid specific volume is estimated to be within ± 0.1% and of the crystal, is about twice that. The specific volume $V(T)$ at a temperature T is fit with an equation of the form:

$$V(T) = V^m[1 + \alpha(T - T^m)] \tag{3.1}$$

where α is the volume expansion coefficient, T^m is the melting (or liquidus) temperature and V^m is the specific volume at the melting (or liquidus) temperature. The liquid and crystalline specific volumes at the liquidus temperatures (V_{Liq}^m, V_{Cry}^m) and the volume expansion coefficients (α_{Liq}, α_{Cry}) for the five alloys are summarized in Table 3.2. The volume change of the liquid upon crystallization expressed as a percentage of the crystal volume ($\Delta V^m/V_{Cry}^m$) at the liquidus temperature is shown in the last column of Table 3.2.

Table 3.2: Specific volume and thermal expansion coefficient

BMG	V_{Liq}^m ($cm^3\ g^{-1}$)	α_{Liq} ($10^{-5}\ K^{-1}$)	V_{Cry}^m ($cm^3\ g^{-1}$)	α_{Cry} ($10^{-5}\ K^{-1}$)	$\Delta V^m/V_{Cry}^m$ (%)
Vit1	0.1668	5.334	0.1650	4.52	1.09
Vit106	0.1502	5.329	0.1468	3.29	2.32
ZrAlCo	0.1672	5.790	0.1637	3.06	2.14
Vit105	0.1559	5.846	0.1525	4.06	2.23
NiNb	0.1199	6.812	0.116	---	3.36

The specific volume data in Table 3.2 show that the best glass former (Vit1) has the smallest change in volume (1.09%) upon crystallization, while the worst glass former ($Ni_{59.5}Nb_{40.5}$) has the largest volume change (3.36%). Recently, Shen et al [13] reported a similar trend during crystallization of amorphous alloys in the Pd-Ni-Cu-P system upon heating in the supercooled liquid region. They found that alloys having the smallest density difference between amorphous and crystalline states revealed the largest supercooled liquid region [13] and larger supercooled liquid regions correlate with better GFA. This implies that the denser the packing of atoms in the glass compared to the corresponding crystal, the better the glass forming ability which is in fact, the trend we observe in this study.

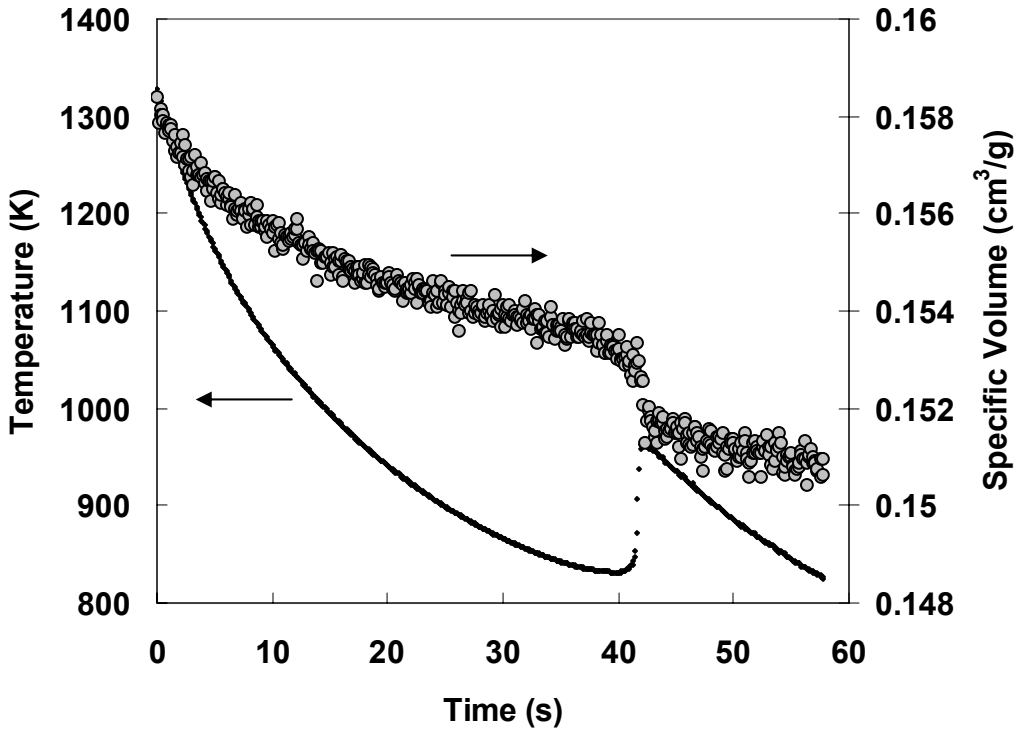

Figure 3.2: Simultaneous measurement of cooling curve and specific volume for Vit105 showing the discontinuous change in volume during recalescence.

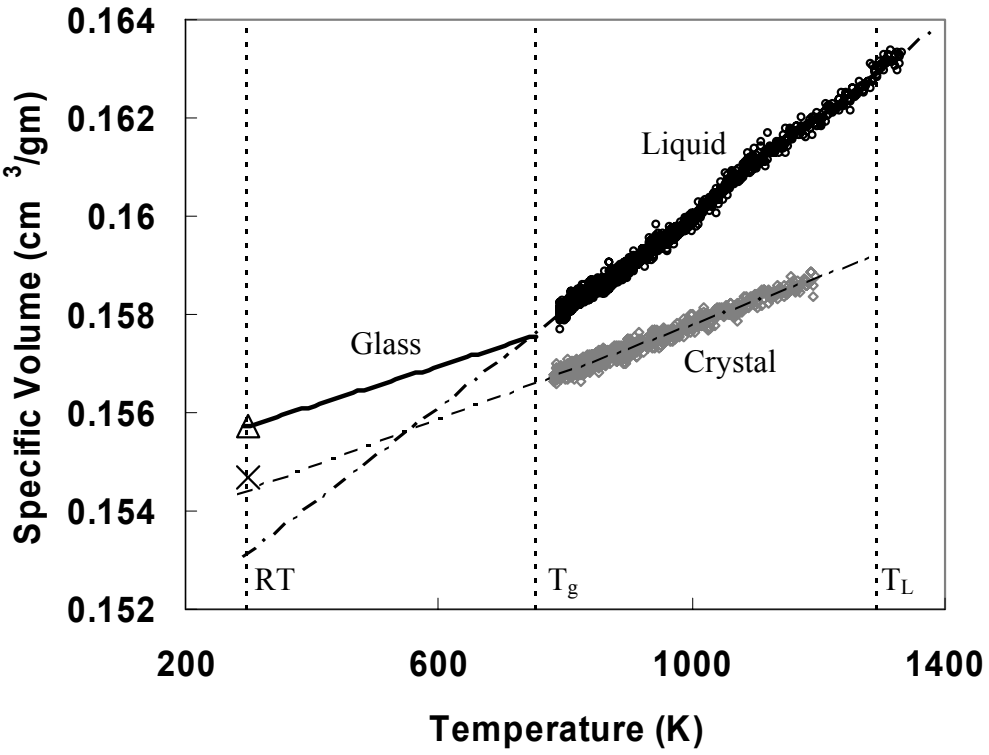

Figure 3.3: Specific volumes of the liquid and crystal as a function of temperature for $Zr_{55}Al_{20}Co_{25}$ (ZrAlCo). Room temperature (RT) specific volumes of the glass (Δ) and the crystal (×) are also indicated in the figure. A straight line (solid line in the figure) connecting the RT amorphous specific volume to the liquid specific volume at the calorimetric glass transition temperature was used to obtain the volume expansion coefficient of the glass. Room temperature (RT), glass transition temperature (T_g), and liquidus temperature (T_L) are indicated by vertical dotted lines in the figure.

3.3.2 Viscosity

The viscosities measured for four of the alloys using the drop oscillation technique are shown in Figure 3.4 with the temperature axis normalized by their respective liquidus temperatures. The viscosities of Vit105 are almost in the same range as Vit106 and hence, are not indicated. The viscosities for two of the constituent pure metals, Cu and Ni, are also shown for comparison [14]. The bulk glass forming alloys show two orders of magnitude higher viscosity compared to pure metals. Among the bulk glass forming alloys, the better glass formers show higher melting temperature viscosity. The critical cooling rates (*Rc*) are indicated alongside the viscosities in Figure 3.4. Thus, this study demonstrates that the high viscosity of bulk glass forming melts plays a decisive role in determining their superior glass forming ability, as seen from the smaller critical cooling rates for vitrification.

Noise level of the measured viscosity is larger at lower temperature because of the increased resistance to oscillation. The maximum viscosity measured was about 200 mPa·s. The average error in viscosity measurement from the decay times at the low temperature end is estimated to be within ± 5%. The range of temperature over which the viscosities were measured and the melting temperature viscosity (η_m) are shown in Table 3.3. The relatively low viscosity of the NiNb alloy made viscosity measurements possible, down to about 60 K undercooling. The viscosity of Vit1 close to the liquidus temperature was measured by Masuhr et al [3] using a Couette viscometer, and viscosities close to T_g were measured by Waniuk et al [15] using the three-point beam bending method. For the range of oscillation frequencies used in this study, the viscosity

of Vit1 was found to be non-Newtonian below 1300 K, as discussed in the Appendix. The viscosities for Vit1 are found to be lower for measurements done with higher resonance frequency, indicating that higher strain rate of deformation leads to lowering of the viscosity. However, for the range in strain rate used during drop oscillation in the ESL, the other alloys investigated in this study did not show non-Newtonian behavior. For Vit106, viscosity close to T_g was determined from the measured flow stresses.

Table 3.3: Melting temperature viscosity and VFT fitting parameters

BMG	Temp. range (K)	η_m (mPa·s)	η_o (mPa·s)	D	T_o (K)
Vit1	1118 – 1278	4835	0.001	23.8	390.0
Vit106	1120 – 1360	200	0.015	11.3	524.7
ZrAlCo	1280 – 1480	100	0.006	12.2	576.0
Vit105	1095 – 1360	180	0.01	11.6	521.0
NiNb	1390 – 1690	45	0.06	5.6	800.0

Within Angell's fragility concept, viscosity of liquids has been correlated with their GFA [2]. Use of glass transition temperature (T_g) as the scaling temperature for viscosity allows for classification of liquids according to their "strong-fragile" behavior. Strong liquids show close to Arrhenius temperature dependence of viscosity and form stable glasses. Fragile liquids, on the other hand, show low viscosity at the melting temperature, only to rise sharply close to the glass transition and form glasses that are unstable with respect to crystallization. The fragility behavior shows a correlation with GFA for BMGs with all metallic constituents [15,16]. However, the behavior of metal-metalloid BMGs such as Pd-Ni-Cu-P does not follow the same trend [17]. The difference in fragility behavior for these two classes of alloys has been attributed to the difference in their liquid structure [18].

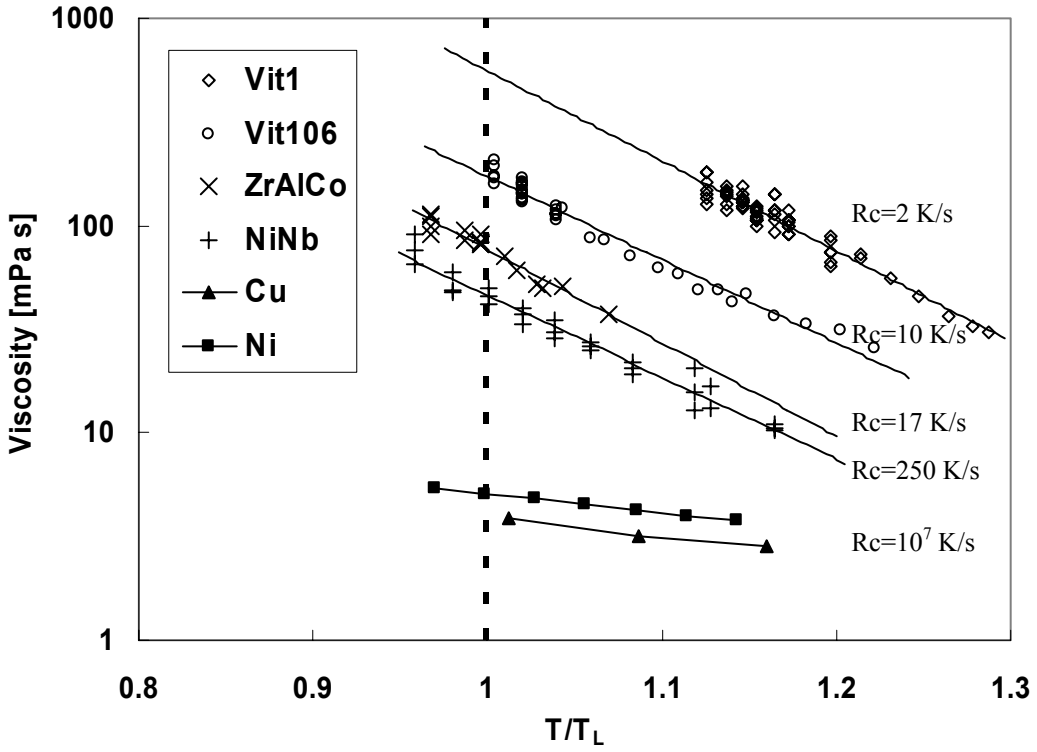

Figure 3.4: Viscosity for the alloys investigated in this study with temperature axis normalized by their respective liquidus temperatures. Viscosity for the pure metals Ni and Cu (obtained from Reference 14) are also indicated. The critical cooling rates for vitrification (Rc) are indicated alongside the viscosity data. The alloys with higher melting temperature viscosity show lower critical cooling rate for vitrification.

Figure 3.5 is the fragility plot for the alloys investigated in this study. Also shown in the figure are the viscosities of silica (SiO_2) [2] which is a canonical example of a strong glass showing Arrhenius temperature dependence of viscosity. The alloys with behavior similar to silica are strong liquids. These strong liquids have a built in resistance to structural change, and their radial distribution function shows little reorganization with wide temperature fluctuations [2]. On the other hand, alloy melts with strong non-Arrhenius temperature dependence of viscosity are termed as fragile liquids. These fragile liquids show large variation in particle orientation and coordination states with slightest provocation from thermal fluctuations [2]. The viscosity values for ZrAlCo and Vit105 are in the same range as Vit106 and are not indicated. This investigation (Figure 3.5), as well as other previous investigations [2,15-17], have shown that the viscosity of most alloy melts, with metallic as well as non-metallic constituents, approaches 10^{15} mPa·s at the calorimetric glass transition temperature. This is the value assumed for the viscosity of ZrAlCo, Vit105 and NiNb at their glass transition temperatures. The viscosities measured in this study were fitted (as shown in Figure 3.5) with the Vogel-Fulcher-Tammann (VFT) equation [2,15-17]:

$$\eta = \eta_o \exp\left(\frac{DT_o}{T - T_o}\right), \tag{3.2}$$

where T_o is referred to as the VFT temperature, D is called the "fragility parameter" and η_o is the high temperature limit of viscosity. The three parameters are summarized in Table 3.3 for all the alloys.

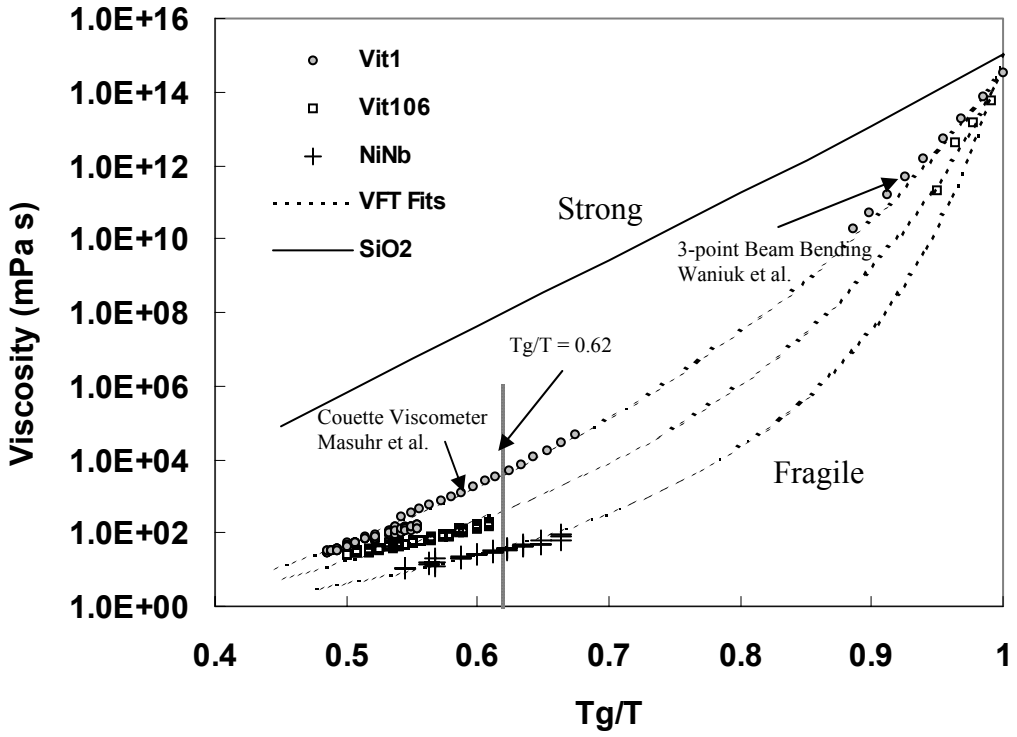

Figure 3.5: Fragility plot of viscosity for Vit1, Vit106 and NiNb. Viscosity data for SiO_2 is taken from Ref [2]. Viscosity data for Vit1 measured by Waniuk et al. [15] and Masuhr et al. [3] are indicated by arrows. All the remaining data points are measured in this study. The liquidus temperature for the three alloys is indicated by the vertical line at T_g/T=0.62. The best fits to the experimental data by Vogel-Fulcher-Tammann (VFT) relation [Equation (3.2)] are indicated by the dotted lines.

A stronger liquid has a higher value of the fragility parameter. The best glass former (Vit1) has the highest value of fragility parameter (D = 23.8), while the worst glass former (NiNb) is found to be most fragile (D = 5.6). Vit1 is therefore a much stronger liquid compared to the NiNb eutectic alloy, and this strong liquid behavior contributes towards better GFA of Vit1. The fragility parameters for ZrAlCo, Vit106, and Vit105 are very close to each other (D = 11.8 ± 0.5), showing their similar GFA. Silica has a fragility parameter of about 100. Thus, stronger metallic glass melts are found to be better glass formers as well. The ratio of glass transition temperature to the liquidus temperature for the alloys investigated in this study is close to 0.62. The liquidus temperature is indicated by a line at T_g/T = 0.62 in Figure 3.5. The best glass former (Vit1) has about two orders of magnitude higher viscosity compared to the worst glass former (NiNb) at their respective liquidus temperatures. The viscosities of Vit106, ZrAlCo, and Vit105 are intermediate between those of Vit1 and NiNb. Thus, this study demonstrates that both the strong liquid behavior and high melting temperature viscosity increase the propensity for glass formation.

3.3.3 Correlation Between Viscosity and Free Volume

Viscosity is correlated with the free volume of the liquid in the Cohen-Grest model as [19]:

$$\eta = \eta_0 \exp\left(bv_o / v_f\right) \tag{3.3}$$

where, v_f denotes the average free volume per atom, and bv_o the critical volume for flow. According to equation (3.3), larger viscosity corresponds to smaller free volume, which

in turn, corresponds to denser packing of atoms in the liquid state. Therefore a high viscosity liquid will show a smaller change in volume upon crystallization.

Figure 3.6 shows viscosity versus volume change upon crystallization for several eutectic (or close to eutectic) alloys and pure metals at the melting temperature, including the alloys investigated in this study. The constituent elements (Ti, Zr, Cu, Ni, Al) which have face-centered cubic (FCC) and hexagonal close-packed (HCP) crystal structures, show large volume changes upon crystallization [7,20], compared to the higher order eutectic alloys investigated in this study or reported elsewhere [21,22]. Also, the viscosities of pure metals [7] are orders of magnitude lower compared to the higher order alloys. It is clear that smaller critical cooling rate is observed for alloys with higher melting temperature viscosity, which translates to a smaller volume change upon crystallization [23]. This suggests that high temperature viscosity and free volume that govern the crystallization kinetics close to the melting temperature have a pronounced influence on the critical cooling rate for vitrification. As shown in Figure 3.6, all the data points can be reasonably fitted with the equation: $\eta_m = 0.98\times\exp[9.76\times V_{Cry}^m/\Delta V^m]$ mPa·s, which is of the same form as equation (3.3) with v_f/v_o being proportional to $\Delta V^m/V_{Cry}^m$. Thus, the melting temperature viscosity is correlated with excess volume in the liquid for a wide variety of alloys and pure metals. These results are consistent with the Cohen-Grest free volume theory [19] because a smaller change in volume upon crystallization implies little free volume in the liquid and correspondingly lower atomic mobility, which leads to higher viscosity.

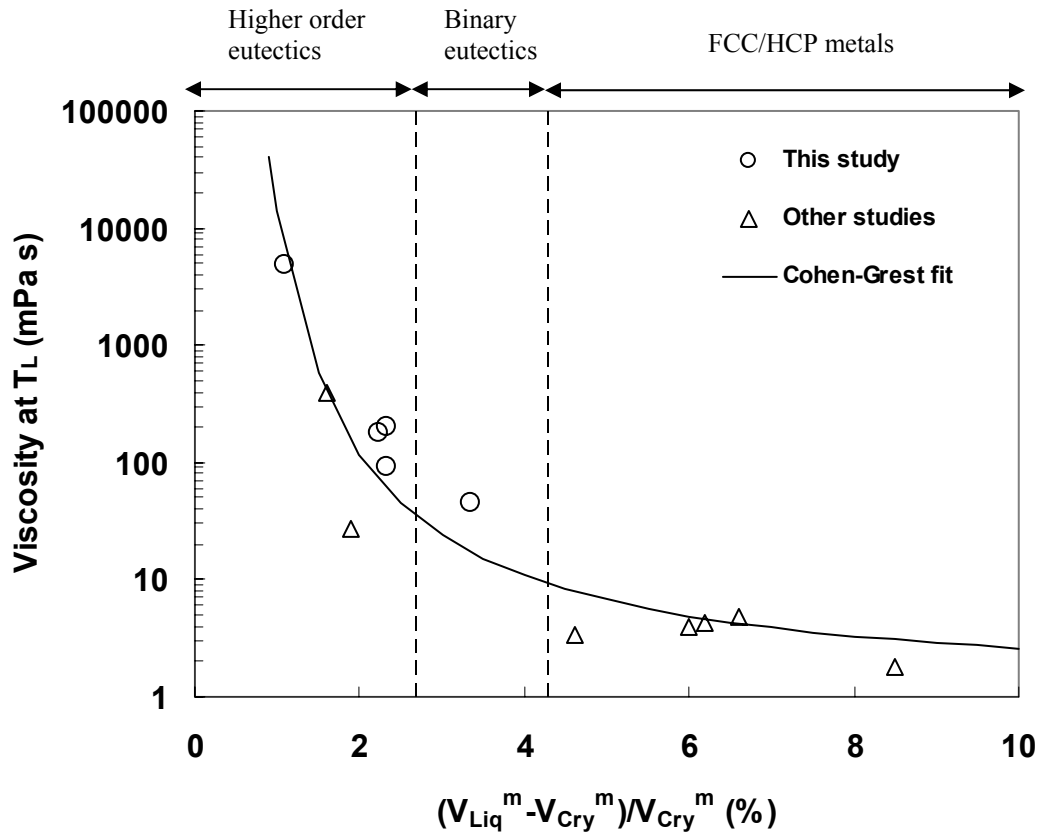

Figure 3.6: Viscosity at liquidus temperature versus the volume change upon crystallization for several eutectic alloys and pure metals. In order of increasing volume change, the data points are for: Vit1 [present work], $Pd_{43}Ni_{27}Cu_{10}P_{20}$ [17,22], $Pd_{40}Ni_{40}P_{20}$ [4,21], Vit105 [present work], Vit106 [present work], $Zr_{55}Al_{20}Co_{25}$ [present work], NiNb [present work], and pure metals (Ti, Zr, Cu, Ni, Al [7,20]). Cohen-Grest free volume fit [19] is indicated.

Comparing equations (3.2) and (3.3), the free volume of the liquid can be expressed in terms of its fragility parameter as:

$$\frac{v_f}{v_o} = \frac{b}{D}\left(\frac{T - T_o}{T_o}\right). \tag{3.4}$$

Cohen and Turnbull [24], in their "free volume" theory for liquids and glasses, proposed that diffusion occurs when redistribution of free volume opens up a void of critical volume (v_o). The parameter b in equation (3.4) corrects for the overlap of free volume. Taking v_o as the limiting specific volume of the liquid at T_o, Cohen and Turnbull [24] found the parameter b to be in the range 0.66 to 0.86 for van der Waals liquids and 0.1 to 0.4 for most pure liquid metals. So the critical volume for flow in case of liquid metals is much smaller (of the order of the ion core volume) compared to van der Waals liquids (of the order of atomic volume). Figure 3.7 shows the percentage of free volume for the three alloys, Vit1, Vit106, and NiNb expressed as a function of the temperature normalized by T_o. Using a value of $b \sim 0.2$, the free volumes for the three alloys at their liquidus temperatures (indicated by arrows in Figure 3.7) agree closely with the experimental values, $\Delta V^m/V_{Cry}{}^m$ given in Table 3.2. Thus, the parameter "b" is almost the same for the three alloys and is within the range found by Cohen and Turnbull [24] for pure metals. In this picture, a stronger liquid can be viewed as one in which the rate of free volume change with temperature is smaller. Thus, better glass formers have smaller free volume at their melting temperatures and also show smaller change in free volume with change in temperature.

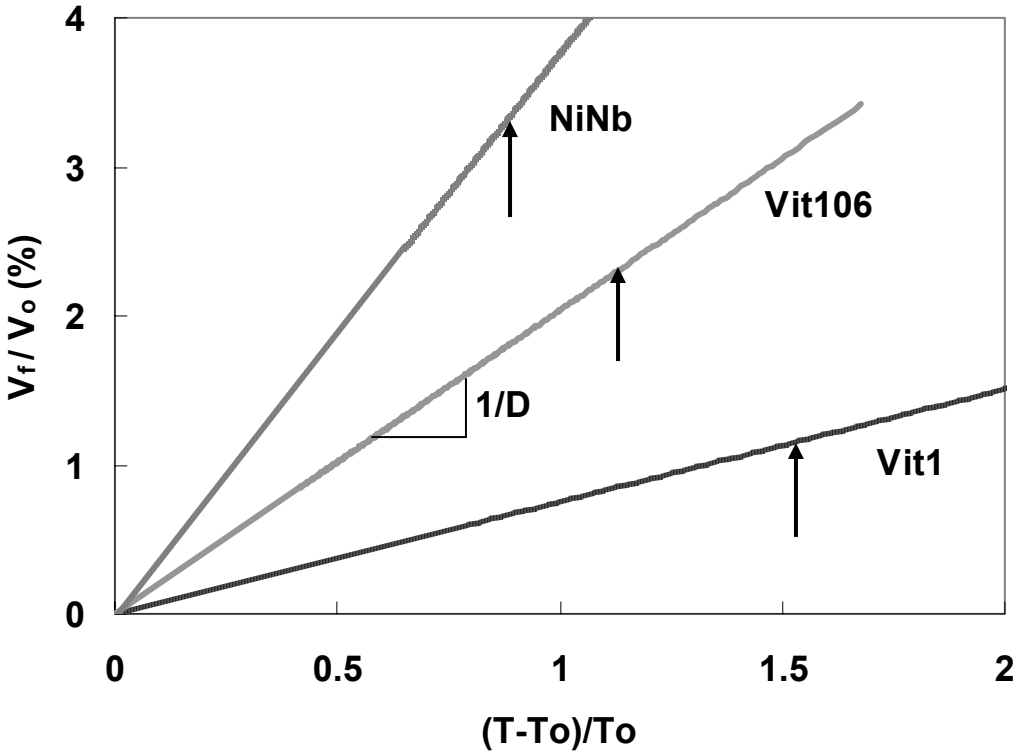

Figure 3.7: Free volume of the glass forming alloys expressed as a percentage. The parameter "*b*" in Equation (3.4) is about 0.2 for all the alloys. The slope of the free volume curves is inversely proportional to the fragility (*D*) of the melt. The liquidus temperatures for the alloys are marked with arrows.

3.3.4 Surface Tension and Its Correlation with Viscosity

Surface tension was obtained for the five glass forming alloys: Vit1, Vit106, ZrAlCo, $Ni_{60}Nb_{34.8}Sn_{5.2}$ (NiNbSn), and NiNb. Surface tension for the ternary alloy, $Ni_{60}Nb_{34.8}Sn_{5.2}$ (NiNbSn) that is obtained by a small addition of tin to the NiNb eutectic alloy, is investigated to understand the surface segregation behavior of tin. The surface tensions for the alloys investigated in this study are shown in Figure 3.8. Except for the NiNb binary alloy that shows a positive temperature gradient of surface tension, the other four alloys show almost constant values over the temperature range investigated [25]. The surface tension of a liquid should decrease with rising temperature because at the critical temperature, the surface between liquid phase and gas phase disappears and the surface tension is reduced to zero. Negative temperature gradient for surface tension has been found for almost all of the pure metals [7] and the values for two of the constituent elements, Cu and Ni, are shown in Figure 3.8. Positive temperature gradient of surface tension has been reported for another deep-eutectic binary alloy, $Ni_{36}Zr_{64}$ [26]. The anomalous positive temperature gradient of surface tension in some alloys may be due to surface segregation of low surface tension element with increasing undercooling. The temperature dependence of surface tension in NiNb alloy suggests that there will be a considerable amount of Marangoni flow if there are temperature gradients in the sample. However, Marangoni flow will not be significant in the other bulk glass forming alloys, making them suitable for diffusion studies.

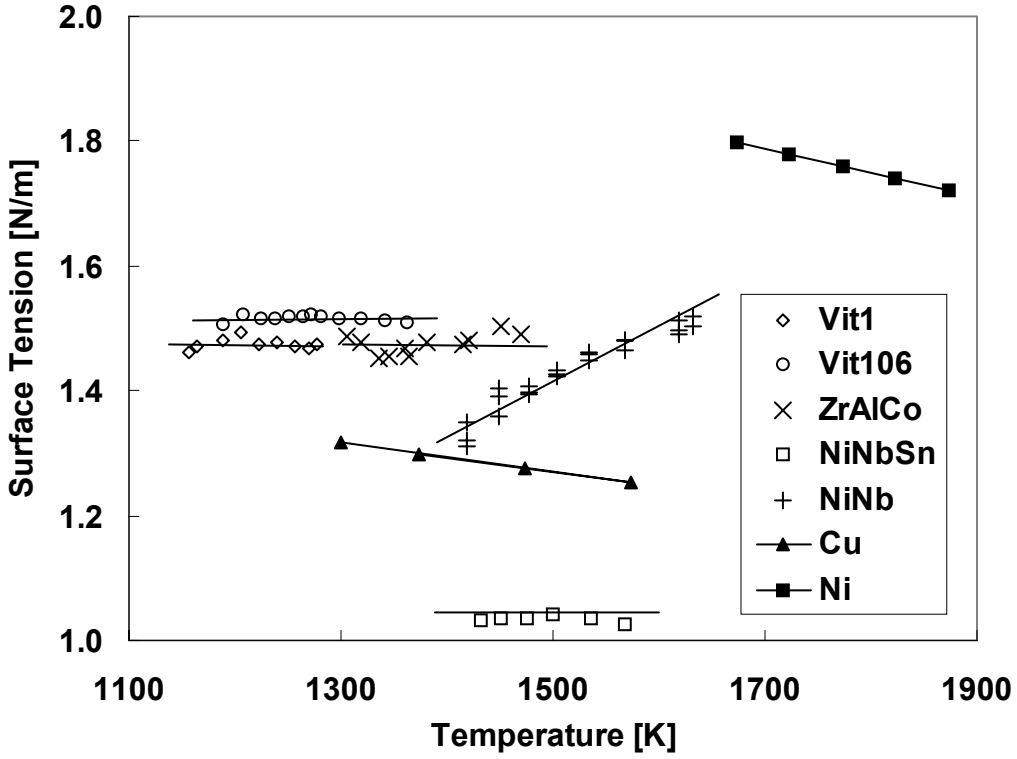

Figure 3.8: Surface tension for the alloys investigated in this study. The surface tension for the pure metals Ni and Cu (obtained from Reference [7]) are also indicated.

The surface tension of most binary liquid mixtures shows negative deviation from the value obtained by assuming the rule of mixtures of pure components' surface tension [7]. This has been attributed to the enrichment of the liquid surface with the component of lower surface tension to minimize the total energy. To evaluate the possible surface segregation effects, surface tension at the melting (or liquidus) temperatures (σ_m) of the alloys investigated in this study are compared with the proportional mathematical addition of pure components' surface tension, as shown in Table 3.4. While the three zirconium-based alloys (Vit1, Vit106 and ZrAlCo) show small deviations from the rule of mixtures, NiNb and NiNbSn show large deviations. The considerably large negative deviation of 52% in the case of NiNbSn shows a significant degree of surface segregation of Sn which has a very low surface tension of 0.56 N/m.

Table 3.4: Surface tension values obtained experimentally and from the rule of mixtures

BMG	σ_m [N m^{-1}] (Experiment)	σ_m [N m^{-1}] (Rule of mixtures)	% deviation
Vit1	1.47	1.49	-1.35
Vit106	1.51	1.45	+4.05
ZrAlCo	1.47	1.44	+2.06
NiNbSn	1.04	1.76	-51.43
NiNb	1.36	1.83	-29.47

The segregation behavior in binary Ag-Sn alloy melts has been investigated theoretically by solving the grand partition functions for the bulk and the surface within the framework of compound formation model [27]. The theoretical results agree well with the experimental finding for Ag-Sn alloys [28], showing pronounced surface segregation of Sn atoms for all bulk concentrations between 0 and 100% Sn. The low surface tension values for NiNbSn observed in this study support this surface segregation

behavior of Sn. The total error involved in the surface tension value is estimated to be within ±5%, and the deviations observed for the zirconium-based alloys are within the experimental uncertainty.

Based on the hard sphere model, a relationship between surface tension (σ) and viscosity (η) was derived for pure metals, making use of the fact that both surface tension and viscosity can be expressed as integrals over the product of inter-atomic forces and the pair distribution function [29,30]:

$$\frac{\sigma}{\eta} = \frac{15}{16}\sqrt{\frac{kT}{m}}, \tag{3.5}$$

where m is the molecular weight, k is the Boltzmann's constant, and T is the temperature. Figure 3.9 shows $(\sigma/\eta)\times(m/T_L)^{1/2}$ plotted versus the square root of temperature normalized by the liquidus temperature (T_L). The correlation has been found to be true for a number of transition and noble metals within 10-20% (shown for Ni and Cu in Figure 3.9) [29]. However, for the complex multi-component alloys, the disparity is by orders of magnitude as shown in Figure 3.9. Equation (3.5) has been derived for pure metals with atoms of a single species and does not take into account the surface segregation and alloying effects that are very important for multi-component systems. In the case of alloys, this approach may be thought of as an effective medium approximation. However, this study shows that such an approximation fails to explain the experimental results. Thus, equation (3.5) is not suitable to estimate viscosity from surface tension and vice-versa for alloys, as done in earlier publications [8].

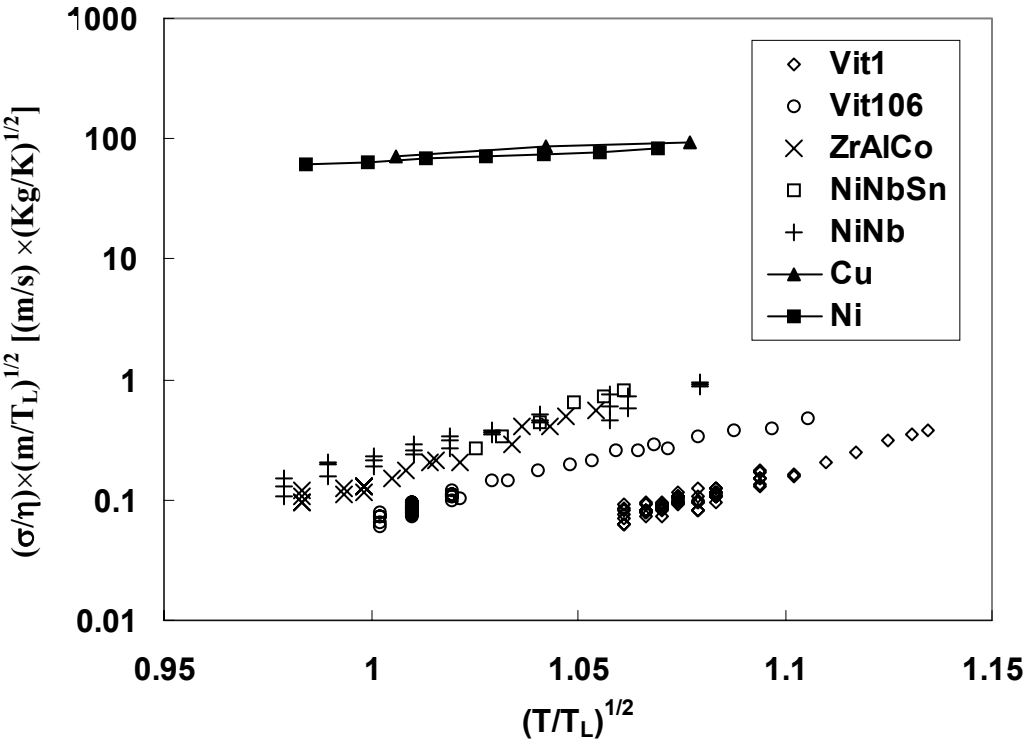

Figure 3.9: Correlation between surface tension and viscosity based on the hard-sphere model for pure metals shows disparity by orders of magnitude in the case of glass forming alloys.

3.3.5 Specific Heat and Total Hemispherical Emissivity

The specific heat (C_P) over total hemispherical emissivity (ε_T) for the three alloys, Vit1, Vit106, and NiNb, were calculated using Equation (2.7) as described in section 2.3.3 from the cooling curves and the specific volume data. The specific heat of the binary eutectic alloy, $Ni_{59.5}Nb_{40.5}$ (NiNb), was measured by AC modulation calorimetry in the TEMPUS (Tiegelfreies ElektroMagnetisches Prozessieren Unter Schwerelosigkeit) electromagnetic levitation facility on board the Space Shuttle Columbia during the International Microgravity Laboratory Mission 2 (IML-2) [31]. Using the eutectic temperature C_P value for NiNb obtained from the TEMPUS experiment, ε_T was determined to be 0.27. Assuming that ε_T remains constant over a few hundred degrees around the melting temperature, the values for the liquid specific heat of the Ni-Nb binary alloy were calculated and are shown in Figure 3.10. As the liquid specific heat and the total hemispherical emissivity of the binary eutectic alloy are known independently, the enthalpy of fusion can be calculated using the relation [32]:

$$h_{f,bin} = \int_{T_u}^{T_{e,bin}} C_{P,bin}(T)dT + \frac{\varepsilon_{T,bin}\sigma_{SB}(T_{e,bin}{}^4 - T_S{}^4)}{m/M}\int_{t=0}^{t=t_p} A(t)dt \qquad (3.6)$$

where T_u is the temperature at maximum undercooling (1322 K), $T_{e,bin}$ is the eutectic temperature (1448 K), T_S is the ambient temperature (taken to be 300 K), $A(t)$ is the time dependent area which was obtained from the sample images, and t_p is the duration of the isothermal plateau, about 5 seconds in this case (see Figure 3.1). The first term in the expression for enthalpy of fusion comes from the undercooled part, and the second term comes from the isothermal part. Using the liquid specific heat and a constant value for the

total hemispherical emissivity (ε_T = 0.27), the enthalpy of fusion was calculated to be 13.6 kJ/mol. The entropy of fusion was calculated by dividing the enthalpy of fusion with the eutectic temperature (1448 K). It was found to have a value of 1.13R $JK^{-1}mol^{-1}$, where R is the Universal gas constant.

The specific heats of Vit1 and Vit106 are shown in Figure 3.10 and were obtained in this study by assuming constant values of total hemispherical emissivities of 0.23 and 0.34, respectively. The specific heats for Vit1 and Vit106 obtained earlier by DSC measurements are also shown for comparison [33,34]. The sharp rise in the ESL values with increasing undercooling compared to the DSC measurements may be due to inaccuracy of measurements by the pyrometer at low temperatures, or the temperature dependence of total hemispherical emissivity. At temperatures close to the glass transition, DSC data is likely to be more accurate because of precise temperature measurement.

The liquid specific heats for the three alloys were fitted with equations of the form [35]:

$$C_P = 3R + AT + BT^{-2} \quad J\ mol^{-1}K^{-1}, \tag{3.7}$$

where R is the Universal gas constant (R = 8.314 J/g atom/K), and, A and B are two constants. The constant term, 3R is the Dulong-Petit value for the constant volume specific heat. The linear temperature term (AT) comes from the difference between the constant pressure specific heat and the constant volume specific heat (C_P-C_V = α^2VT/κ, where α is the volume expansion coefficient, V is the molar volume, and κ is the isothermal compressibility) and also the electronic contribution to the specific heat. The B/T^2 term was earlier used as an empirical fit to the liquid specific heat data [35].

However, recently this temperature dependence has been derived to be a fundamental property of the liquid stemming from the Gaussian energy landscape of the liquid atoms [36]. The parameters A and B for the three alloys are listed in Table 3.5.

The enthalpies of fusion for a number of glass forming alloys obtained in this study as well as other previous studies [33,34,37] are plotted against their melting temperatures in Figure 3.11. The results for a few of the constituent metals [7] are also indicated. It is clear from Figure 3.11 that the glass forming alloys follow Richard's rule [7], an empirical rule which states that the entropy of fusion (ΔS_f) for most pure metals is around 1.06R J/K/mol where R is the Universal gas constant. The melting temperature for the alloys was taken to be the point corresponding to the peak in the DSC curve. The error bar in Figure 3.11 represents the melting interval (between the solidus and liquidus temperatures). It was previously stated that the entropy of fusion (ΔS_f) should be an indicator of glass forming ability [33], with better glass formers showing smaller entropy of fusion because the thermodynamic driving force for crystallization is directly proportional to ΔS_f. However, the experimentally measured entropies of fusion for a wide range of glass formers do not support this argument, as shown in Figure 3.11. This illustrates that the thermodynamic driving force may not be significant in determining the glass forming ability of an alloy.

Table 3.5: Total hemispherical emissivity, specific heat parameters and entropy of fusion

BMG	ε_T	A **(JK^{-2}mol^{-1})**	B **(JKmol^{-1})**	ΔS_f **(JK^{-1}mol^{-1})**
Vit1	0.23	0.0036	1.09×10^{7}	1.04R
Vit106	0.34	0.0074	8.85×10^{6}	1.02R
NiNb	0.27	0.0044	3.54×10^{7}	1.13R

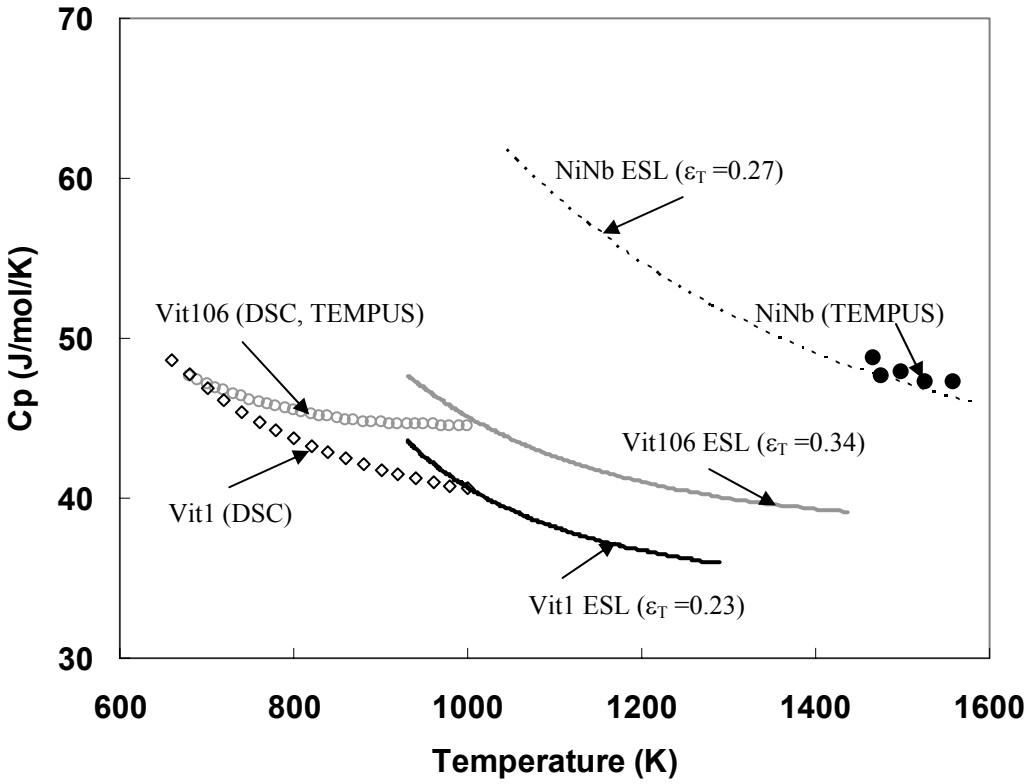

Figure 3.10: Liquid specific heat for Vit1, Vit106 and NiNb obtained in the present ESL study using constant values for total hemispherical emissivities that are indicated within parentheses. The specific heats of NiNb as obtained earlier from TEMPUS experiments are shown by the solid circles [31]. Specific heats for Vit1 and Vit106 as obtained in earlier studies using DSC are indicated by open diamonds and open circles, respectively [33,34].

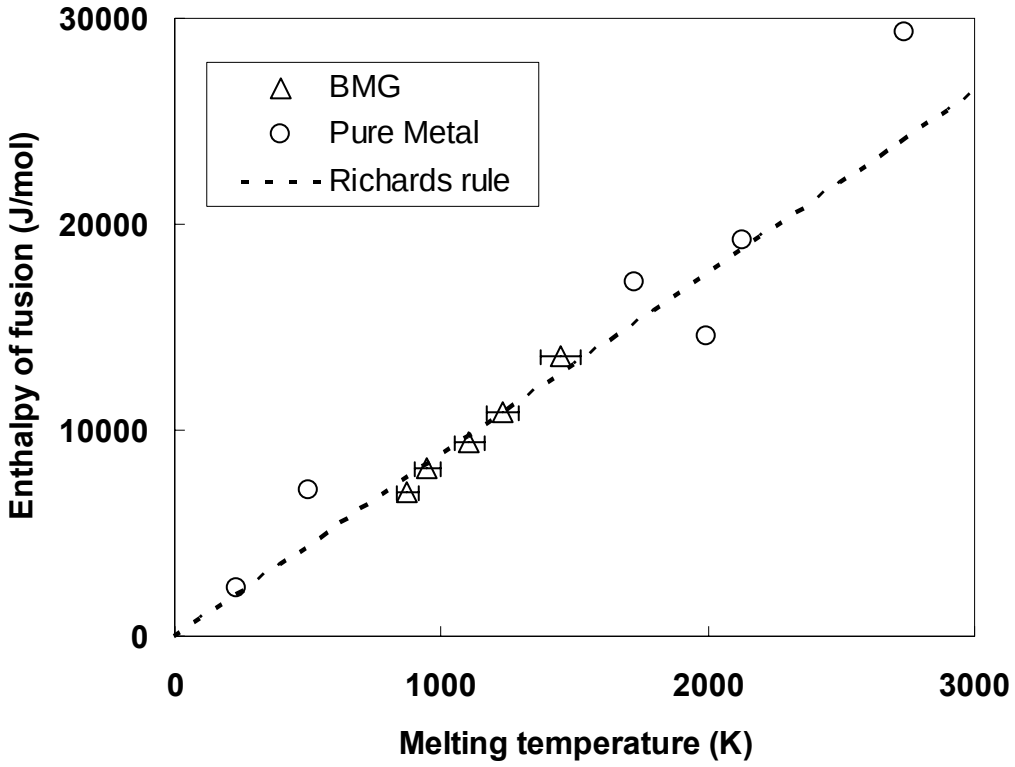

Figure 3.11: Enthalpy of fusion versus the melting temperature for a number of BMGs and pure metals. In order of increasing melting temperatures, the metals (open circles) are Hg, Sn, Ni, Ti, Zr, and Nb [7]. In order of increasing melting temperatures, the BMGs (open triangles) are $Pd_{43}Ni_{10}Cu_{27}P_{20}$ [37], Vit1 [33], Vit106 [34], ZrAlCo [present work], and NiNb [present work]. Richard's rule is shown by the dotted line. The error bar in temperature for some of the alloys indicates the melting interval (between solidus and liquidus temperatures).

3.4 Conclusions

Based on the results discussed in this chapter, the following conclusions can be drawn regarding the role of kinetic and thermodynamic properties on the glass-forming ability of bulk metallic glass-forming alloys:

(1) The high temperature viscosity and free volume of the glass forming melts that determine the kinetics of these systems have the most pronounced influence on their critical cooling rates for vitrification. The viscosities were measured using the drop-oscillation technique, while the specific volumes were obtained by image capture, digitization and Legendre polynomial fitting. The glass forming melts show orders of magnitude higher viscosity compared to pure metals. The better glass former has higher viscosity at its liquidus temperature and shows a smaller change in volume upon crystallization compared to a poorer glass former. The viscosity at the melting temperature is correlated with volume change upon crystallization in accordance with Cohen-Grest free-volume theory for a large variety of alloys.

(2) Classification of the bulk metallic glass forming melts according to their "strong-fragile" behavior shows that the stronger liquid is a better glass former compared to a fragile liquid. The glass transition temperature was used as the scaling temperature for viscosity and the data were fitted with Vogel-Fulcher-Tammann (VFT) equation to obtain the fragility parameters (D). The best glass former has much higher value of fragility parameter (D_{Vit1} = 23.8) compared to the worst

glass former (D_{NiNb} = 5.6). Therefore Vit1 is a much stronger liquid compared to the NiNb eutectic alloy and the temperature dependence of viscosity for Vit1 is closer to Arrhenius behavior.

(3) High temperature surface tensions for bulk metallic glass forming alloys, measured for the first time using the drop oscillation technique, do not show any correlation with glass forming ability. The surface tension follows proportional mathematical addition of pure components' surface tension except when some of the constituent elements have much lower surface tension. In such cases, there is surface segregation of the low surface tension elements as found for tin in the Ni-Nb-Sn ternary alloy. Correlations between surface tension and viscosity for pure metals based on the hard sphere model are found to be inapplicable to the complex multi-component systems.

(4) The experimentally measured entropies of fusion for a wide range of glass formers follow Richard's rule similar to pure metals, showing that the thermodynamic driving force may not be significant in determining the glass forming ability of these alloys. The specific heat and total hemispherical emissivity were determined for the three alloys, Vit1, Vit106 and NiNb, from their cooling curves and specific volume data. The total hemispherical emissivity was found to be in the range 0.23 to 0.34.

3.5 References

[1] P. S. Steif, F. Spaepen, and J. W. Hutchinson, Acta Mater. **30**, 447 (1982).

[2] C. A. Angell, Science **267**, 1924 (1995).

[3] A. Masuhr, T. A. Waniuk, R. Busch, and W. L. Johnson, Phys. Rev. Lett. **82**, 2290 (1999).

[4] K. H. Tsang, S. K. Lee, and H. W. Kui, J. Appl. Phys. **70**, 4837 (1991).

[5] I. Egry, G. Lohofer, I. Seyhan, S. Schneider, and B. Feuerbacher, Appl. Phys. Lett. **73**, 462 (1998).

[6] X. J. Han and B. Wei, Philos. Mag. **83**, 1511 (2003).

[7] T. Iida and R. I. L. Guthrie, *The Physical Properties of Liquid Metals* (Clarendon, Oxford; 1988).

[8] H. P. Wang, C. D. Cao, B. Wei, Appl. Phys. Lett. **84**, 4062 (2004).

[9] S. Mukherjee, Z. Zhou, J. Schroers, W. L. Johnson, and W. K. Rhim, Appl. Phys. Lett. **84**, 5010 (2004).

[10] S. Mukherjee, H. –G. Kang, W. L. Johnson, and W. K. Rhim, Phys. Rev. B **70**, 174205 (2004).

[11] X. H. Lin and W. L. Johnson, J. Appl. Phys. **78**, 6514 (1995).

[12] S. Mukherjee, Z. Zhou, W. L. Johnson, and W. K. Rhim, J. Non-Cryst. Solids **337**, 21 (2004).

[13] T. D. Shen, U. Harms, and R. B. Schwarz, Appl. Phys. Lett. **83**, 4512 (2003).

[14] I. Egry, Scr. Met. Mater. **28**, 1273 (1993).

[15] T. A. Waniuk, R. Busch, A. Masuhr, and W. L. Johnson, Acta Mater. **46**, 5229 (1998).

[16] R. Busch, E. Bakke, and W. L. Johnson, Acta Mater, **46**, 4725 (1998).

[17] G. J. Fan, H.-J. Fecht, and E. J. Lavernia, Appl. Phys. Lett. **84**, 487 (2004).

[18] G. J. Fan, R. K. Wunderlich, and H.-J. Fecht, Mat. Res. Soc. Symp. Proc. **754**, CC5.9.1 (2003).

[19] M. H. Cohen and G. S. Grest, Phys. Rev. B **20**, 1077 (1979).

[20] A. Buch, *Pure metals properties*, Materials Park (OH), ASM International, 1999.

[21] K. C. Chow, S. Wong, and H. W. Kui, J. Appl. Phys. **74**, 5410 (1993).

[22] I. R. Lu, G. P. Gorler, and R. Willnecker, Appl. Phys. Lett. **80**, 4534 (2002).

[23] S. Mukherjee, J. Schroers, Z. Zhou, W. L. Johnson, and W. K. Rhim, Acta Mater. **52**, 3689 (2004).

[24] M. H. Cohen and D. Turnbull, J. Chem. Phys. **31**, 1164 (1959).

[25] S. Mukherjee, W. L. Johnson, and W. K. Rhim, Appl. Phys. Lett. **86**, 014104 (2005).

[26] I. Egry, G. Lohofer, E. Gorges, and G. Jacobs, J. Phys.: Condens. Matter **8**, 9363 (1996).

[27] L. C. Prasad, R. N. Singh, V. N. Singh, and G. P. Singh, J. Phys. Chem. B **102**, 921 (1998).

[28] J. Lauermann, G. Metzger, and F. Z. Sauerwal, Phys. Chem. **216**, 42 (1961).

[29] I. Egry, Scr. Met. Mater. **28**, 1273 (1993).

[30] M. Shimoji, Adv. Phys. **16**, 705 (1967).

[31] Team TEMPUS, *Materials and fluids under low gravity*, edited by L. Ratke, H. Walter and B. Feuerbacher, 233 (Springer, Berlin, 1996).

[32] A. J. Rulison, and W. K. Rhim, Rev. Sci. Instrum. **65**, 695 (1994).

[33] R. Busch, Y. J. Kim, and W. L. Johnson, J. Appl. Phys. **77**, 4039 (1995).

[34] S. C. Glade, R. Busch, D. S. Lee, W. L. Johnson, R. K. Wunderlich, and H. J. Fecht, J. Appl. Phys. **87**, 7242 (2000).

[35] O. Kubaschewski, C. B. Alcock, and P. J. Spencer, *Materials Thermochemistry*, 6th ed. (Pergamon, New York, 1993).

[36] W. L. Johnson, private communication.

[37] I. –R. Lu, G. Wilde, G. P. Gorler, and R. Willnecker, J. Non-Cryst. Solids **250-252**, 577 (1999).

Chapter 4

Overheating Threshold and Its Influence on TTT Curves of Bulk Metallic Glasses

Abstract

A pronounced effect of overheating is observed on the crystallization behavior of three bulk metallic glasses: $Zr_{41.2}Ti_{13.8}Cu_{12.5}Ni_{10}Be_{22.5}$ (Vit1), $Zr_{57}Cu_{15.4}Ni_{12.6}Al_{10}Nb_5$ (Vit106), and $Zr_{52.5}Cu_{17.9}Ni_{14.6}Al_{10}Ti_5$ (Vit105). A threshold overheating temperature is found for each of the three alloys, above which there is a drastic increase in the undercooling level and the crystallization times. This effect is attributed to oxide particles acting as heterogeneous nucleation sites, unless dissolved by overheating above their melting points. Time-Temperature-Transformation (TTT) diagrams are measured for the three alloys by overheating above their respective threshold temperatures. The TTT curves for Vit1 and Vit106 are very similar in shape and scale with their respective glass transition temperatures, suggesting that system-specific properties do not play a crucial role in defining crystallization kinetics in these alloys. The critical cooling rates to vitrify the alloys are determined from the TTT curves to be about 2 K/s for Vit1 and 10 K/s for Vit106. All the measurements are carried out using the electrostatic levitation technique to avoid any heterogeneous nucleation effects from container walls or environment.

Keywords: Isothermal Crystallization; Overheating; Undercooling; Nucleation

4.1 Introduction

Bulk glass forming alloys are distinguished from each other by their critical cooling rates for vitrification. The critical cooling rate can be directly measured from the Time-Temperature-Transformation (TTT) curve, which describes the transformation kinetics from undercooled liquid to crystal in an isothermal experiment. From a practical standpoint, the TTT curves provide the temperature-time window for processing of bulk glass forming alloys without undesirable crystallization effects. The shape and position of the TTT curve in the temperature-time space is determined by the intrinsic nucleation and growth mechanism. Therefore, TTT curves provide insight into the crystallization behavior of bulk metallic glasses (BMGs). However, the intrinsic nucleation effects may be overshadowed by extraneous influences that may change the position and shape of the TTT curve. To obtain the intrinsic crystallization timescales, it is imperative to identify and eliminate any of these heterogeneous influences [1,2]. To that effect, high vacuum containerless processing methods are ideal for the study of crystallization behavior of BMGs because they eliminate surface nucleation effects induced by container walls or environment.

The TTT curve for one of the best known bulk metallic glass formers, $Zr_{41.2}Ti_{13.8}Cu_{12.5}Ni_{10}Be_{22.5}$ (Vit1), was obtained using an electrostatic levitator (ESL) by Kim *et al.* [3]. The TTT curve was found to have "nose" temperature of 850 K and "nose" time of about 50 seconds. While the ESL study of Vit1 provided remarkable insights into its crystallization behavior, there are still some open questions about the

influence of heterogeneous effects on the crystallization timescales. The effect of oxygen content on TTT curve was investigated by Lin *et al.* [4] for another Zr-based BMG, $Zr_{52.5}Cu_{17.9}Ni_{14.6}Al_{10}Ti_5$ (Vit105). They observed that the critical cooling rate of Vit105 increased several orders of magnitude with the increase in oxygen content. So far, the study by Lin *et al.* [4] is the only one to have addressed heterogeneous influences on TTT curves.

In this chapter, the pronounced influence of overheating on the crystallization behavior for three bulk metallic glasses are discussed. The alloys investigated are: $Zr_{41.2}Ti_{13.8}Cu_{12.5}Ni_{10}Be_{22.5}$ (Vit1), $Zr_{57}Cu_{15.4}Ni_{12.6}Al_{10}Nb_5$ (Vit106), and $Zr_{52.5}Cu_{17.9}Ni_{14.6}Al_{10}Ti_5$ (Vit105). A threshold overheating temperature is found for each of the three alloys, above which there is a drastic increase in the undercooling level and the crystallization times. Possible mechanisms for explaining this behavior, in particular the influence of oxygen on glass forming ability, are discussed. Time-Temperature-Transformation (TTT) diagrams were measured for the three alloys by overheating above their respective threshold temperatures. The measurements are carried out in a high vacuum electrostatic levitator (HVESL) which is described in chapter 2.

4.2 Results and Discussion

The methodology behind the measurement of undercooling behavior and TTT curves is discussed in chapter 2. Figure 4.1 (a) is the summary of the maximum undercooling level achieved with different overheating temperatures for Vit105. The cooling curves obtained from different levels of overheating are shown in part (b) of

Figure 4.1. Crystallization is evidenced by recalescence - the sharp rise in temperature due to the release of the latent heat of fusion. Samples cooled from below 1140 K showed very small undercooling. Samples cooled from temperatures between 1150 K and 1220 K showed larger undercooling (~ 60 K) and recalesced back to the solidus temperature to form an isothermal plateau until the entire sample crystallized. A step increase in the undercooling level to a significantly larger value (~ 220 K) was observed when the samples were overheated above 1225 K. At this point, it should be mentioned that the sample has to be overheated each time above the threshold temperature of 1225 K to achieve deep undercooling. It is not sufficient to overheat just once for all subsequent undercooling studies.

The effect of overheating on Vit106 is summarized in Figure 4.2. As the overheating temperature was raised, crystallization, which initially appeared as a sharp rise in temperature, gradually reduced to small humps. Finally, for overheating above 1410 K, the hump in the cooling curve disappeared altogether and the temperature-time profile suggests that the material solidified in an amorphous structure, confirmed by DSC measurements.

To study the effect of overheating on the TTT curve for Vit1, the sample was isothermally annealed at 830 K (close to the nose temperature in the previous ESL study [3]) and the time for crystallization was noted as a function of sample overheating. When the sample was overheated below 1250 K, crystallization time was about 30 seconds. However, the crystallization time increased to about 130 seconds for overheating above 1300 K, as shown in Figure 4.3.

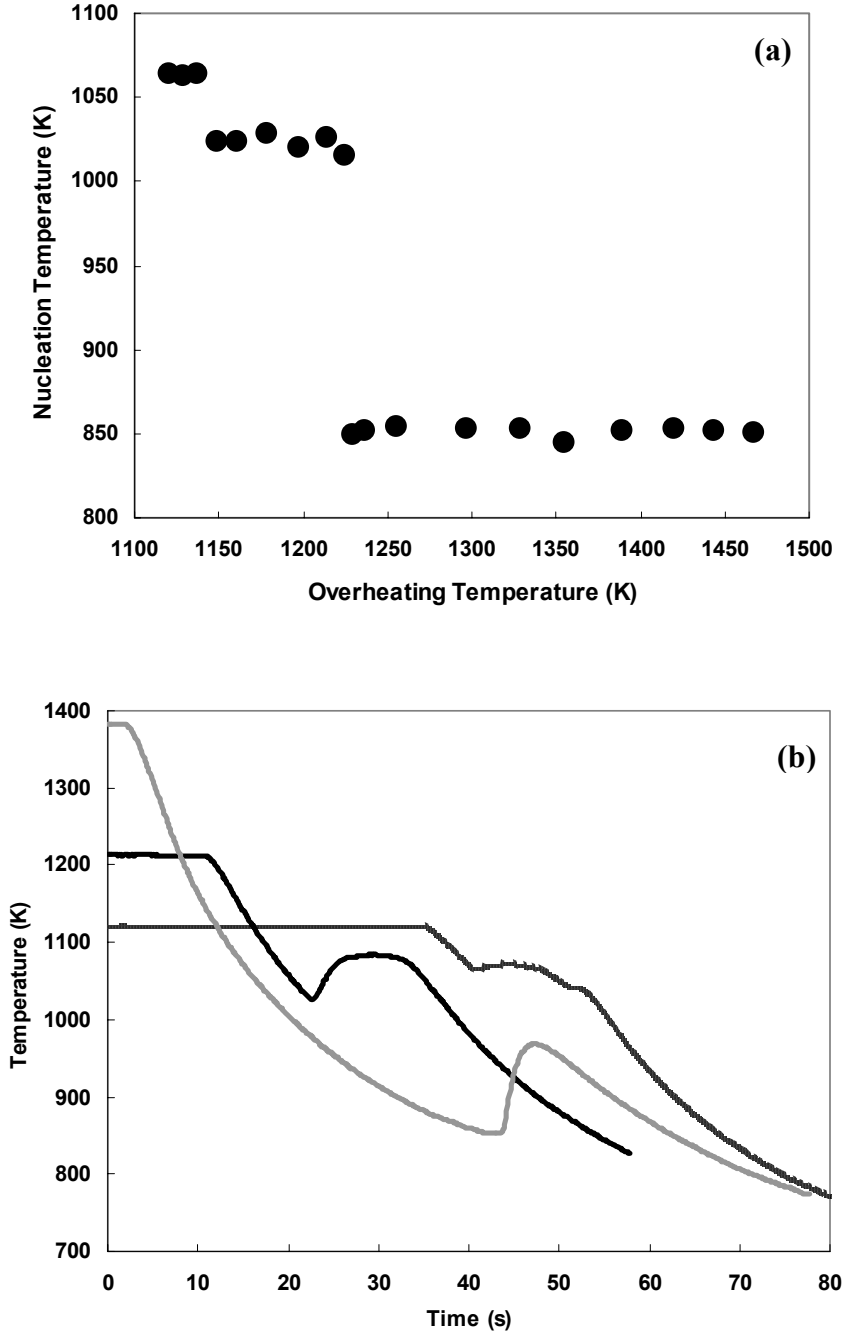

Figure 4.1: (a) Nucleation temperature versus overheating temperature for $Zr_{52.5}Cu_{17.9}Ni_{14.6}Al_{10}Ti_5$ (Vit105); (b) cooling curves obtained from different levels of overheating in which the temperature at time $t = 0$ s shows the level of overheating.

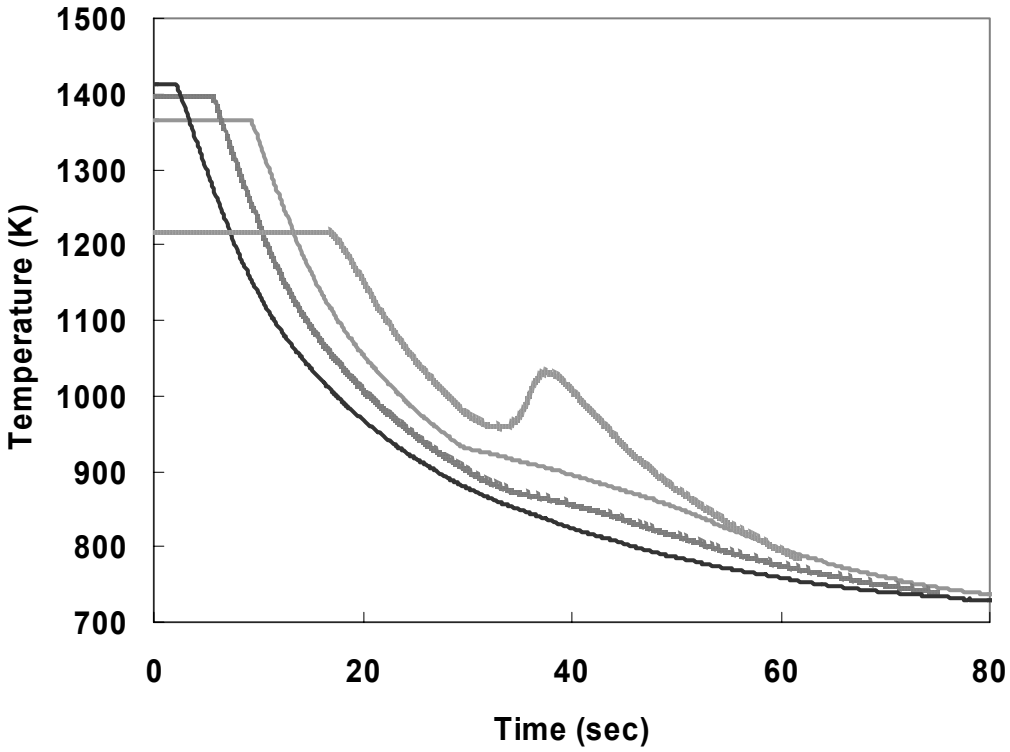

Figure 4.2: The cooling curves obtained for $Zr_{57}Cu_{15.4}Ni_{12.6}Al_{10}Nb_5$ (Vit106) with different levels of overheating. The alloy vitrifies for overheating above the threshold temperature of 1410 K.

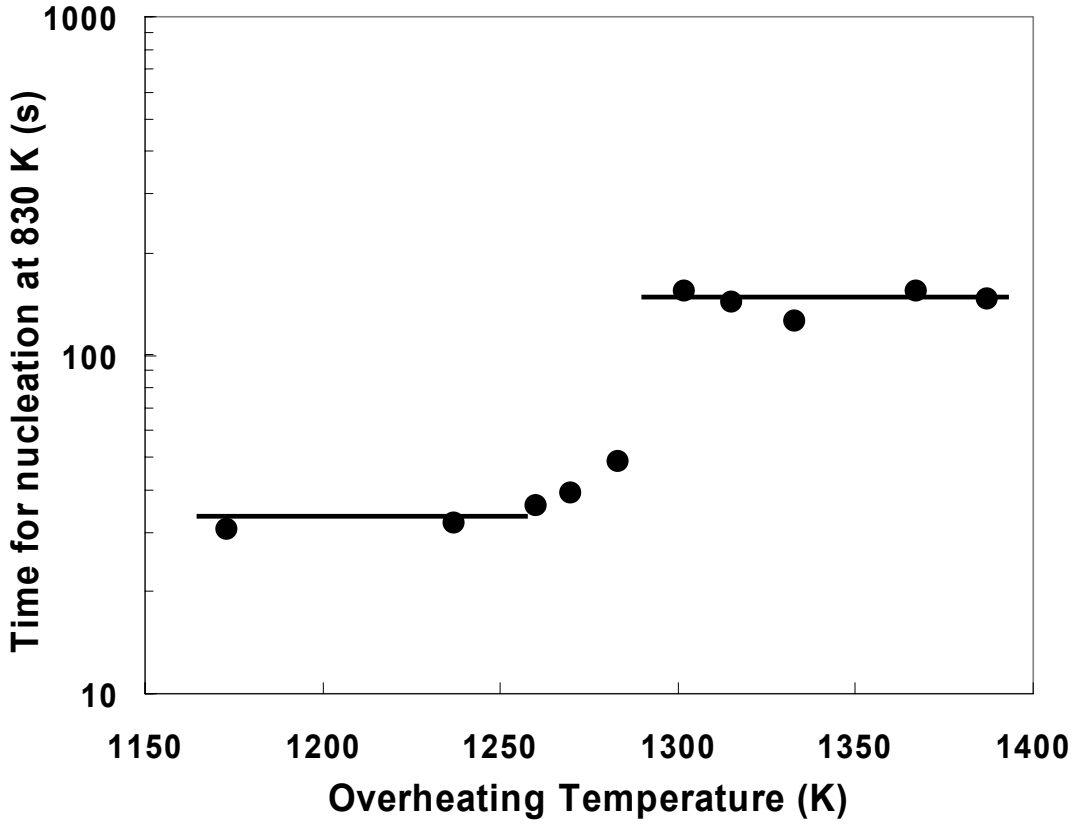

Figure 4.3: Isothermal (830 K) annealing times until crystallization as a function of different levels of overheating for $Zr_{41.2}Ti_{13.8}Cu_{12.5}Ni_{10}Be_{22.5}$ (Vit1).

After the identification of the critical overheating temperatures (1225 K for Vit105, 1410 K for Vit106, and 1300 K for Vit1), TTT curves were measured for the three alloys by cooling them from above their respective threshold temperatures. The crystallization behavior of Vit1 at four different levels of undercooling is indicated in Figure 4.4. For isothermal anneal at a temperature of 850 K as shown by curve (a) which corresponds to an undercooling of 143 K, crystallization occurs after about 350 seconds as observed by the single, sharp recalescence. For deeper undercoolings at isothermal temperatures of 755 K and 740 K, two step and broad recalescence events were observed as shown by curves (c) and (d). The crystallization behaviors of Vit106 and Vit105 were very similar to Vit1, except that for deep undercoolings, only a single broad recalescence event was observed instead of two steps. The measured TTT curves are shown in Figure 4.5. The starting of the isothermal anneal time at each temperature was used as the time origin (t=0) for the TTT curves. The TTT curves for Vit1 and Vit106 show the expected "C" shape. For Vit1, the nose temperature and nose time are 800 K and 70 seconds, respectively. The nose temperature is about 50 K lower, the nose time about 20 seconds longer, and the TTT curve is much narrower compared to the previous ESL study by Kim *et al.* [3]. The entire TTT curve for Vit106 was obtained for the first time with a nose temperature of 880 K and nose time of 5 seconds. For Vit105, only the upper part of the TTT curve could be obtained, even with heating the sample above the critical overheating temperature. The samples crystallized instantly for temperatures below 860 K. The critical cooling rate is estimated to be 25 K/s for Vit105.

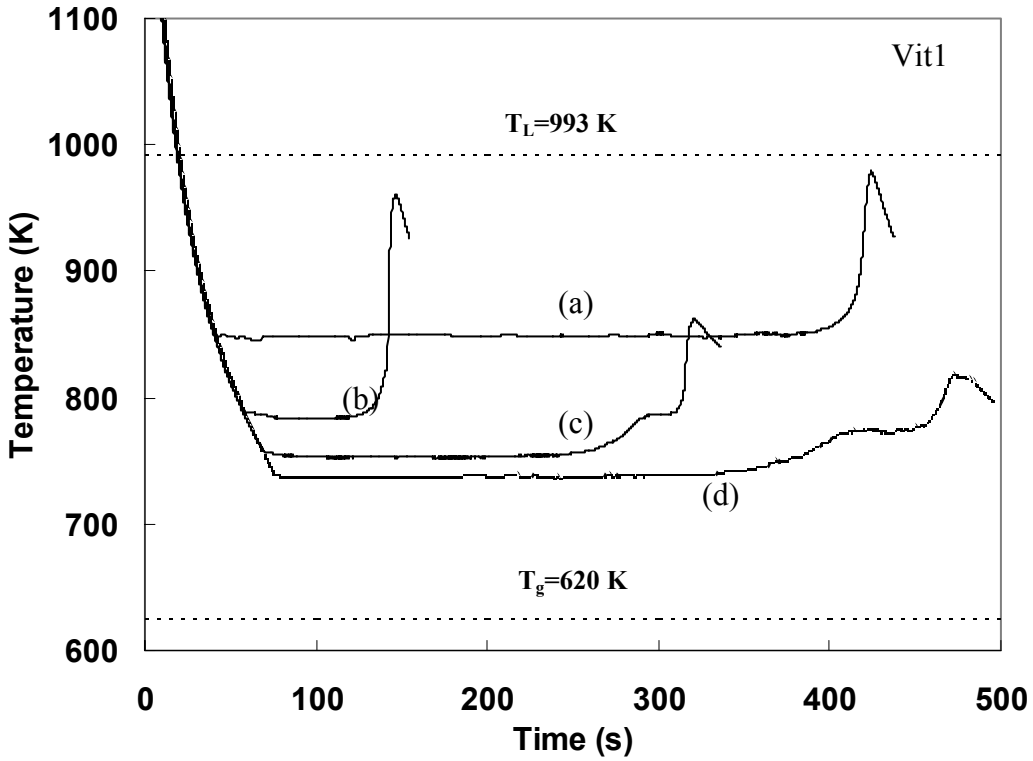

Figure 4.4: Crystallization of $Zr_{41.2}Ti_{13.8}Cu_{12.5}Ni_{10}Be_{22.5}$ (Vit1) during isothermal annealing at (a) 850 K, (b) 785 K, (c) 755 K, and (d) 740 K. Single sharp recalescence is seen for shallow undercoolings while two-step, broad recalescence events are observed at deep undercooling levels.

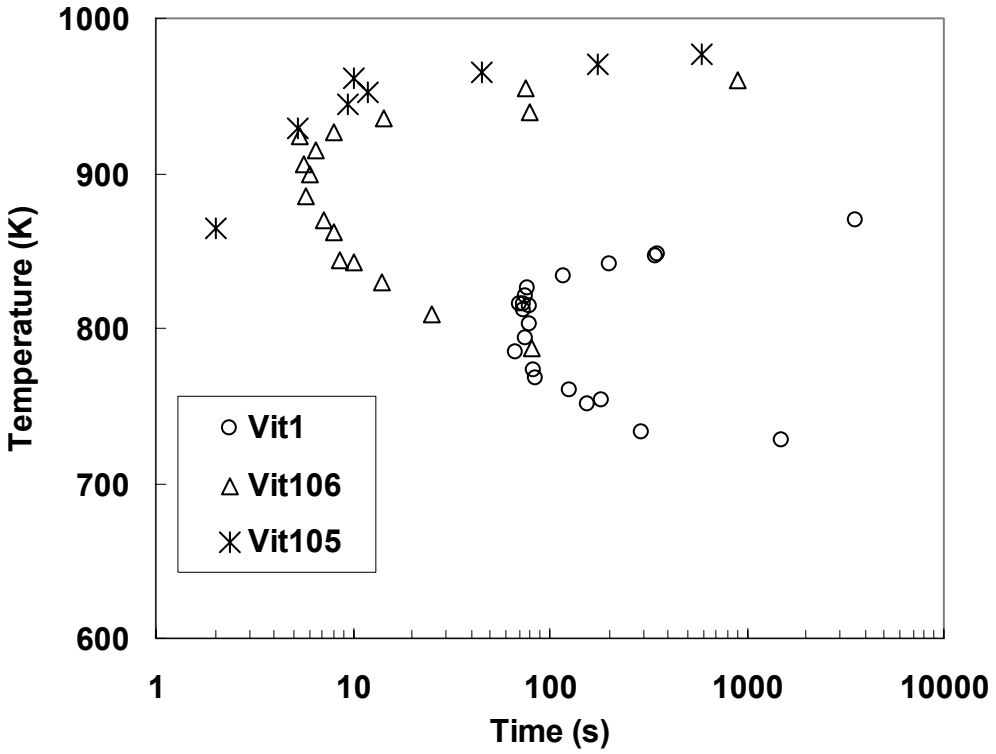

Figure 4.5: Time-Temperature-Transformation (TTT) curves for $Zr_{52.5}Cu_{17.9}Ni_{14.6}Al_{10}Ti_5$ (Vit105), $Zr_{57}Cu_{15.4}Ni_{12.6}Al_{10}Nb_5$ (Vit106), and $Zr_{41.2}Ti_{13.8}Cu_{12.5}Ni_{10}Be_{22.5}$ (Vit1). Vit1 and Vit106 could be vitrified by free radiative cooling of mm scale liquid droplets in the ESL, while Vit105 could not be vitrified.

A pronounced influence of overheating is observed on the undercooling levels and the crystallization times for all the three BMGs: Vit105, Vit106 and Vit1. A threshold overheating temperature is observed, above which there is a drastic change in the crystallization kinetics. Prior to each undercooling experiment, the sample has to be heated above the threshold temperature. This suggests that heterogeneities acting as nucleation sites are dissolved by heating above the threshold temperature and re-form during crystallization of the liquid sample (dynamic heterogeneous nucleation). This dynamic nucleation behavior is illustrated in Figure 4.6. If the liquid is cooled from a temperature below the threshold overheating temperature the heterogeneous sites are never dissolved and induce the crystallization process (static heterogeneous nucleation as shown in Figure 4.6). This leads to smaller undercoolings and shorter crystallization times. Static and dynamic heterogeneous nucleation, as seen in this study, was observed in different grades of pure zirconium, suggesting that these are rather ubiquitous phenomena limiting the undercooling level of pure zirconium and its alloys [5].

In an earlier investigation on Vit1, it was found that crystallization changes from a nucleation-controlled mechanism at high temperatures to a growth controlled mechanism at low temperatures [6]. Impurities acting as heterogeneous sites strongly affect the nucleation process, but have negligible influence on the growth process. Therefore, reduction of heterogeneous influences will be reflected more in the upper part of the TTT curve which is nucleation controlled. This in turn will cause the nose of the TTT curve to be at a lower temperature and shifted towards longer crystallization time. Indeed, the nose of the TTT curve for Vit1 obtained after overheating above the threshold

temperature in this study is lower by 50 K and shifted to the right compared to the previous ESL study [3].

In the earlier ESL investigation of Vit1 [3], a small recalescence event was observed in the free radiative cooling curve below 800 K. This was attributed to the decomposition of the undercooled liquid with respect to Zr and Be. However, it was found in the present study that by cooling the Vit1 melt from above the critical over-heating temperature of 1300 K, the anomaly in the cooling curve disappeared altogether, just as in Vit106. This suggests that the slight hump in the cooling curve observed in the previous study may have been a signature of heterogeneous nucleation which is suppressed by higher overheating. Phase separation behavior of Vit1 was investigated in earlier studies using small angle neutron scattering (SANS). A classic spinodal decomposition behavior was found by Schneider *et al.* [7] with a spinodal temperature of 670 K. The lowest temperature for the TTT curve measurement of Vit1 in this study was 730 K, which is 60 K above the spinodal temperature. Therefore, the shape of our TTT curve was most likely unaffected by the phase separation behavior.

The role of oxygen content on the crystallization behavior of Vit105 was investigated by Lin *et al.* [4]. They found that the crystallization timescales decreased significantly with the increase in oxygen content of the alloy. Liu *et al.* [8] investigated the influence of oxygen impurity and micro-alloying on the glass forming ability of Vit105. They concluded that the glass forming ability was limited not by phase separation behavior, but rather, by heterogeneous nucleation triggered by oxygen-induced nuclei. They used scanning transmission electron microscopy to identify the heterogeneous nucleation sites as Zr_4Ni_2O particles [8]. Micro-alloying was found to alleviate the

detrimental effects of oxygen. Kundig *et al.* [9] reported significant improvement in glass forming ability of Vit105 by adding 0.03% to 0.06% Sc to the melt before casting. They attributed this improvement to the binding of Sc to oxygen in the melt, thereby suppressing the formation of crystallization catalyzing oxides. The high affinity of zirconium for oxygen [10] and all the aforementioned experimental results [4,8,9] suggest that the overheating effects we see for all the Zr-based BMGs in this study can be explained by oxide particles acting as heterogeneous sites. The threshold overheating temperature most likely corresponds to the melting point of this oxide phase.

To compare the TTT curves of Vit1 and Vit106, the temperatures in the TTT curves are normalized by the glass transition temperature and time-axis is normalized by the nose time of each alloy. The normalized plot is shown in Figure 4.7. The nose temperatures (T_n) for the two alloys bear a constant ratio with their respective glass transition temperatures ($T_n/T_g \sim 1.3$). The shapes of the TTT curves are very similar for the two alloys on the normalized plot. However, the nose time for Vit106 is about 5 seconds, while that of Vit1 is 70 seconds - more than an order of magnitude larger. The critical cooling rates to vitrify the alloys as determined from the TTT curves are about 2 K/s for Vit1 and 10 K/s for Vit106. The similarity in shapes of the two TTT curves both above and below the nose suggests that once the heterogeneous influences are suppressed, system-specific properties like the primary phase do not play a crucial role in defining crystallization kinetics in these alloys [11]. The times for crystallization scale with some underlying property of these liquids.

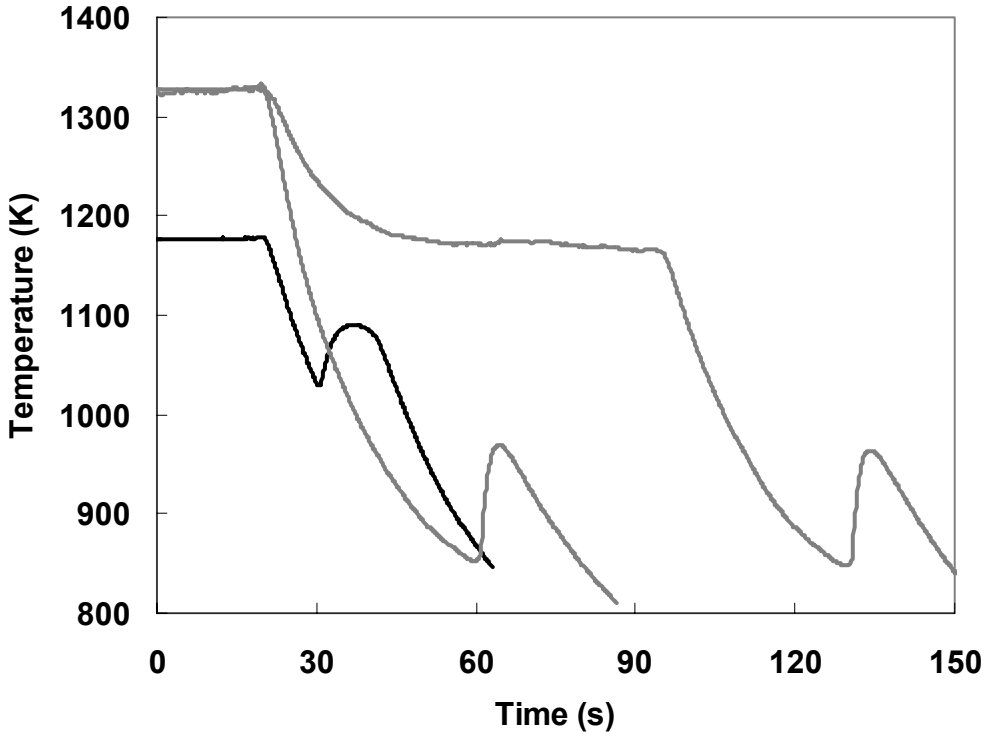

Figure 4.6: Static (black line) and dynamic (grey lines) heterogeneous nucleation in $Zr_{52.5}Cu_{17.9}Ni_{14.6}Al_{10}Ti_5$ (Vit105). Once dissolved, the heterogeneous sites have to re-form in order to trigger nucleation. The sample has memory of the superheat temperature as indicated by the two-step cooling process.

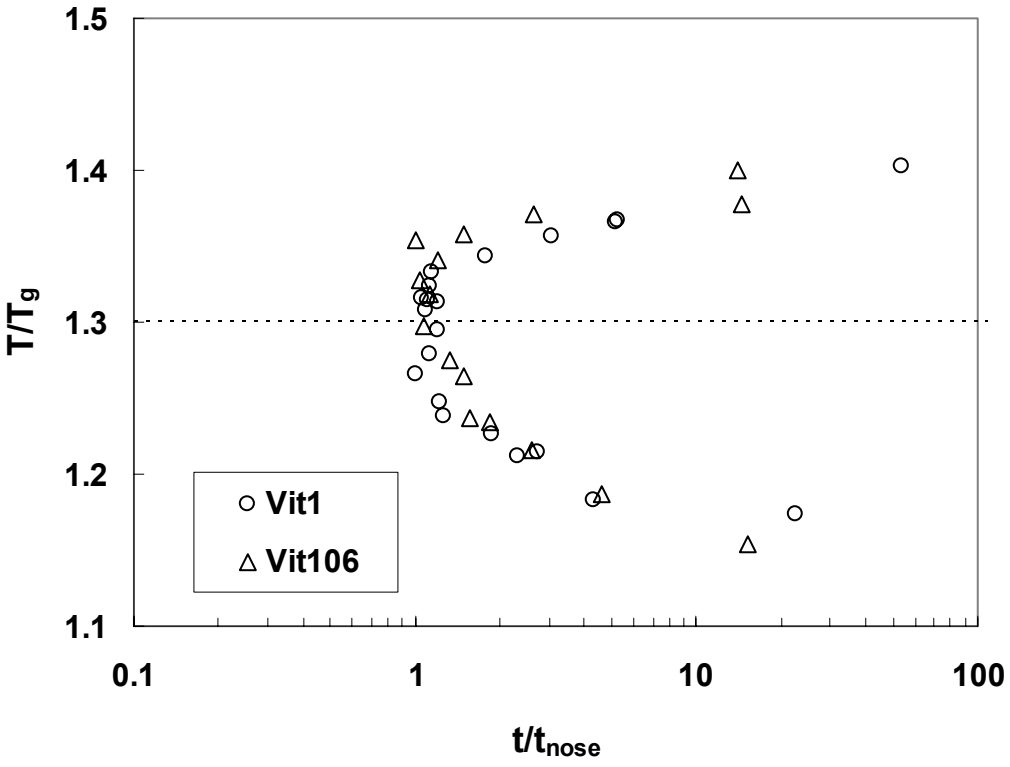

Figure 4.7: TTT curves for Vit1 and Vit106 with temperature axis normalized by glass transition temperature and time axis normalized by the nose times. The similarity in TTT curves, both above and below the nose suggests that crystallization kinetics is independent of system-specific properties.

4.3 Conclusions

From the study of heterogeneous influences on undercooling behavior and TTT curves of the three bulk metallic glasses, $Zr_{41.2}Ti_{13.8}Cu_{12.5}Ni_{10}Be_{22.5}$ (Vit1), $Zr_{57}Cu_{15.4}Ni_{12.6}Al_{10}Nb_5$ (Vit106), and $Zr_{52.5}Cu_{17.9}Ni_{14.6}Al_{10}Ti_5$ (Vit105), the following conclusions can be drawn:

(1) There is a pronounced effect of overheating on the crystallization behavior of bulk metallic glasses. A threshold overheating temperature is found for each of the three alloys, above which there is a drastic increase in the undercooling level and the crystallization times. The critical overheating temperatures are 1225 K for Vit105, 1410 K for Vit106, and 1300 K for Vit1. This overheating threshold most likely corresponds to the melting point of an oxide phase which triggers heterogeneous nucleation unless dissolved.

(2) Time-Temperature-Transformation (TTT) diagrams obtained for the three alloys by overheating above their respective threshold temperatures reflect their intrinsic crystallization timescales. The critical cooling rate for vitrification, as determined from the TTT curves, is about 2 K/s for Vit1 and 10 K/s for Vit106. For Vit105, only the upper part of the TTT curve could be obtained because the samples crystallized instantly for temperatures below 860 K. The critical cooling rate for Vit105 is estimated to be 25 K/s, based on the maximum casting thickness to produce fully amorphous structure.

(3) Reduction of heterogeneous influences is reflected more in the upper part of the TTT curve which is nucleation controlled. Impurities acting as heterogeneous

sites strongly affect the nucleation process, but have negligible influence on the growth process. This explains the lowering of the nose temperature and increase of the nose time for the TTT curve of Vit1 compared to previous studies.

(4) Despite a large difference in critical cooling rates, the TTT curves for Vit1 and Vit106 are very similar in shape and scale with their respective glass transition temperatures. The nose temperatures (T_n) for the two alloys bear a constant ratio with their respective glass transition temperatures ($T_n/T_g \sim 1.3$). This suggests that the times for crystallization are independent of system specific properties and scale with some underlying characteristic of these liquids.

4.4 References

[1] T. D. Shen and R. B. Schwarz, Appl. Phys. Lett. **75**, 49 (1999).

[2] J. Schroers, Y. Wu, and W. L. Johnson, Phil. Mag. **82**, 1207 (2002).

[3] Y. J. Kim, R. Busch, W. L. Johnson, A. J. Rulison, and W. K. Rhim, Appl. Phys. Lett. **68**, 1057 (1996).

[4] X. H. Lin, W. L. Johnson, and W. K. Rhim, Mater. Trans. JIM **38**, 473 (1997).

[5] A. J. Rulison, W. K. Rhim, R. Bayuzick, W. Hofmeister, and C. Morton, Acta Mater. **45**, 1237 (1997).

[6] J. Schroers, R. Busch, and W.L. Johnson, Appl. Phys. Lett. **76**, 2343 (2000).

[7] S. Schneider, P. Thiyagarajan, U. Geyer, and W. L. Johnson, Physica B **241-243**, 918 (1998).

[8] C. T. Liu, M. F. Chisholm, and M. K. Miller, Intermetallics **10**, 1105 (2002).

[9] A. A. Kundig, D. Lepori, A. J. Perry, S. Rossmann, A. Blatter, A. Dommann, and P. J. Uggowitzer, Mater. Trans. JIM **43**, 1 (2002).

[10] *Metals Handbook*, Tenth Edition Vol. 2, 667 (ASM International, 1990).

[11] S. Mukherjee, Z. Zhou, J. Schroers, W. L. Johnson, and W. K. Rhim, Appl. Phys. Lett. **84**, 5010 (2004).

Chapter 5

Glass Forming Trend and Crystallization Pathways of Novel Bulk Amorphous Zr-Al-Co-(Cu) Alloys

Abstract

Crystallization behavior of bulk glass forming alloys in the Zr-Al-Co-(Cu) system is investigated using the electrostatic levitation technique. The compositions investigated are $Zr_{55}Al_{20}Co_{25}$, $Zr_{55}Al_{22.5}Co_{22.5}$ and $Zr_{55}Al_{19}Co_{19}Cu_7$. Free radiative cooling in the electrostatic levitator could vitrify all the three alloys. This allowed, for the first time, the determination of Time-Temperature-Transformation (TTT) curves for ternary metallic alloys over a wide temperature range between the liquidus and glass transition temperatures. While the TTT curve for $Zr_{55}Al_{22.5}Co_{22.5}$ shows the expected "C" shape with a single "nose", the TTT curves for the other two alloys show two noses. The crystallization pathways are investigated in these systems by X-ray diffraction measurements taken after isothermal annealing at different undercooling levels. The average critical cooling rate for vitrification of the Zr-Al-Co-(Cu) alloys estimated from the measured TTT curves is about 17 K/s. This value of critical cooling rate is supported by the trends in the melting temperature viscosity, fragility behavior, and volume change upon crystallization compared to other glass forming systems.

Keywords: Bulk Metallic Glass; X-ray Diffraction; Isothermal Crystallization

5.1 Introduction

Among the different metallic glass forming systems, it has been found that the increase in the number of components makes the process of glass formation easier [1]. This has been attributed to the fact that in complex multi-component alloys with large mismatches in the atomic sizes, the formation of crystals is more likely to be frustrated ("confusion principle" [1]). Thus, identification of good glass formers in lower order systems leaves the scope for further enhancement of glass forming ability (GFA) by the addition of more components. Recently, new glassy alloys in the ternary systems, Zr-Al-Fe and Zr-Al-Co have been found which have large supercooled liquid regions and good mechanical properties [2]. To date, the investigation of crystallization behavior in the deep undercooled liquid region has been limited to four or five component alloys (for detailed reviews, see References [3] and [4]). Thus, the new ternary alloys with large supercooled liquid region offer the opportunity for similar investigations and comparisons with the more established quaternary and quinary glass formers. This will greatly enhance the understanding of the glass formation process in metallic alloys as a function of the number of components.

In this chapter, crystallization behavior of two compositions in the Zr-Al-Co ternary alloy system is discussed. The effect of a small addition of a fourth element (copper) is also reported. The alloys investigated are: $Zr_{55}Al_{20}Co_{25}$ (ZAC), $Zr_{55}Al_{22.5}Co_{22.5}$ (ZAC+Al), and $Zr_{55}Al_{19}Co_{19}Cu_7$ (ZAC+Cu). The containerless electrostatic levitation (ESL) technique, as discussed in chapter 2, was used for the

measurements. Each of the three alloys could be vitrified by free radiative cooling in the ESL. This allowed for the first time the measurement of entire Time-Temperature-Transformation (TTT) curves of ternary metallic alloys in the deep undercooled liquid state. The thermal stability associated with glass formation and crystallization was examined by Differential Scanning Calorimetry (DSC). The crystallization pathways were investigated in these systems by x-ray diffraction (XRD) measurements taken after isothermal annealing at different undercooling levels. The combined XRD data and TTT curves are used to explain the crystallization process.

5.2 Experimental Details

The alloys were prepared from high purity starting materials in an arc melter. The glass transition temperatures (T_g), crystallization temperatures (T_x) and liquidus temperatures (T_L) were obtained for all of the alloys using graphite crucibles in a Differential Scanning Calorimeter (DSC) at a heating rate of 0.33 Ks^{-1}. The DSC Curves for the three alloys are shown in Figure 5.1. A distinct glass transition, followed by a large supercooled liquid region before crystallization, is observed for the three alloys. The T_g, T_x, T_L, T_g/T_L, and the supercooled liquid region defined by ΔT [$=T_x-T_g$] for the three alloys are listed in Table 5.1. The supercooled liquid region for ZAC and ZAC+Cu are about the same (65 K), while that for ZAC+Al is slightly lower (55 K). The narrow melting interval for ZAC+Cu suggests that it is close to an eutectic composition, while the larger difference between the liquidus and solidus temperatures for ZAC and ZAC+Al suggest that they are far from any eutectic. The T_g/T_L value, which is often used as an

indicator of GFA, is almost the same for the three alloys with an average value of 0.576 (Table 5.1).

Small samples (~ 15 mg) were levitated in the ESL and melted. By shutting off the laser completely, the sample could be cooled in a purely radiative way. To determine the TTT diagrams, isothermal experiments were performed. Therefore, the molten sample was cooled radiatively to a predetermined temperature by turning off the laser, which was turned back on to maintain the isothermal temperature. The crystalline phases obtained after isothermal annealing at different undercoolings were analyzed with X-ray diffraction (XRD) method using a Cu-Kα source. Since only a very small quantity of powder was obtained after crushing the 15 mg ESL processed samples, a zero-background silicon sample holder was used to obtain the XRD spectra.

The measured thermophysical properties for the three alloys are very similar. The experimental details and the results for one of the alloys (ZAC) are discussed in detail in chapter 3. The average critical cooling rate for vitrification of these alloys is about 17 K/s, as will be discussed in the next section. This value of critical cooling rate is supported by the trends in the melting temperature viscosity, fragility behavior, and volume change upon crystallization compared to other glass forming systems, as discussed in chapter 3.

Table 5.1: Characteristic temperatures and width of supercooled liquid region

BMG	T_g (K)	T_x (K)	ΔT [$=T_x-T_g$](K)	T_L (K)	T_g/T_L
ZAC	753	818	65	1293	0.582
ZAC+Al	753	808	55	1323	0.569
ZAC+Cu	733	798	65	1271	0.577

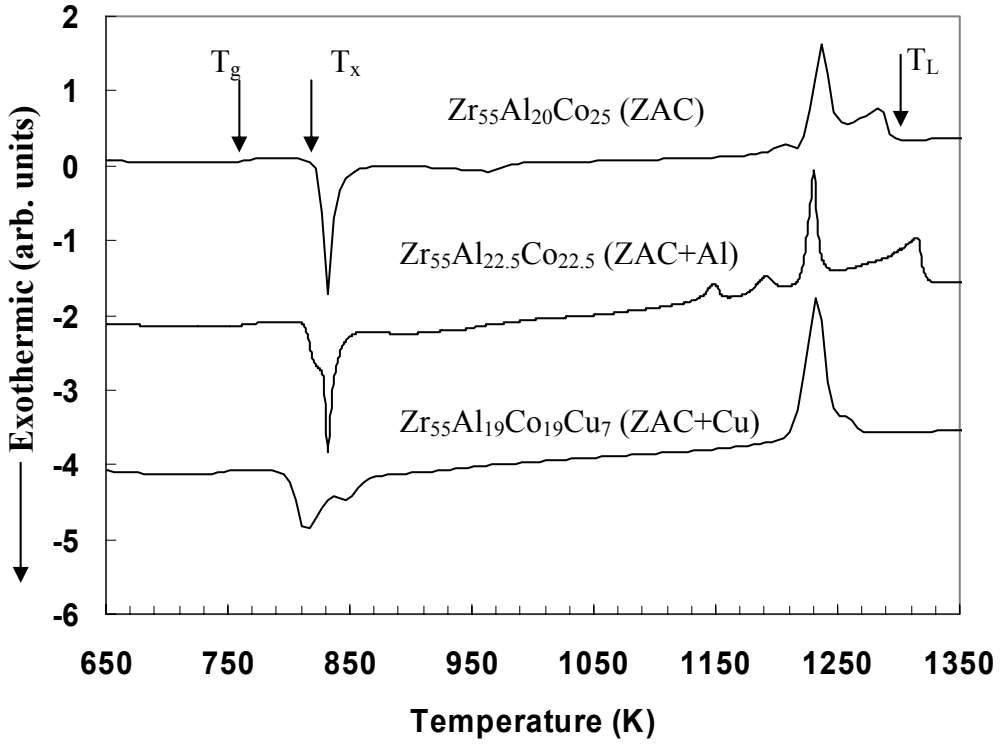

Figure 5.1: DSC plots for $Zr_{55}Al_{20}Co_{25}$ (ZAC), $Zr_{55}Al_{22.5}Co_{22.5}$ (ZAC+Al) and $Zr_{55}Al_{19}Co_{19}Cu_7$ (ZAC+Cu) obtained by heating amorphous samples at 0.33 K/s showing glass transition (T_g), crystallization (T_x) and liquidus (T_L) temperatures. The characteristic temperatures for one of the alloys are marked by arrows.

5.3 Results and Discussion

All of the three alloys could be vitrified by free radiative cooling from temperatures above their liquidus. A typical cooling curve obtained for ZAC+Al is shown in Figure 5.2, along with the variation in cooling rate. There is no heat-release event due to crystallization during the entire cooling process, and the alloy solidifies in an amorphous structure - confirmed by DSC measurement. To understand the crystallization behavior of the three alloys in the undercooled liquid state, TTT curves were obtained by isothermal annealing at different undercooling levels. Prior to each isothermal measurement, the sample was subjected to melting and radiative cooling. The temperature-time profiles for three different undercooling levels are shown in Figure 5.3 for one of the alloys, ZAC+Al. At the isothermal temperature of 1080 K (small undercooling), crystallization sets in after about 65 seconds and brings the sample to the solidus temperature as shown by the curve (a) in Figure 5.3. For deeper undercooling at a temperature of 970 K, the isothermal time is about 2 seconds as shown by curve (b), but the recalescence peak is very sharp. Finally, at a temperature of 845 K, the isothermal time is much longer and a broad crystallization peak is observed as shown by curve (c), suggesting a copious nucleation event, but slow growth kinetics. Unlike the cases in (a) and (b), the heat released during crystallization of the sample isothermally held at 845 K is not enough to raise the sample to the solidus temperature.

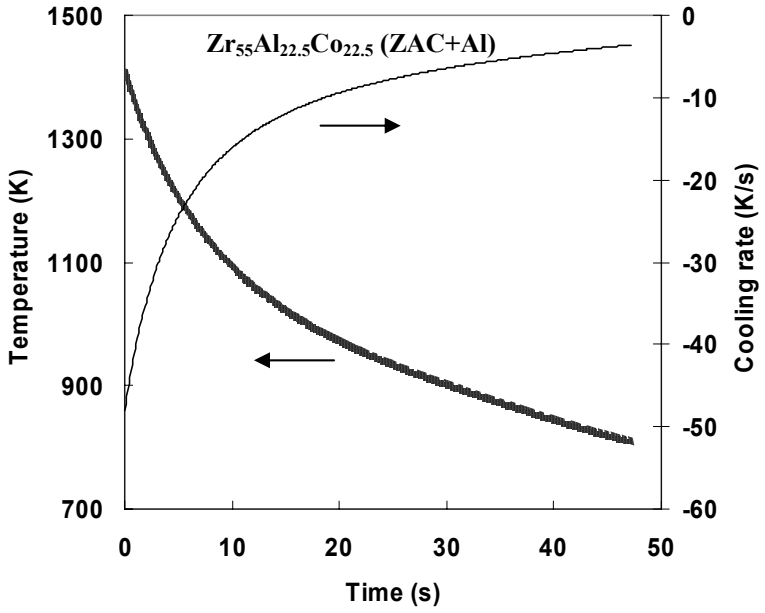

Figure 5.2: Typical thermogram for $Zr_{55}Al_{22.5}Co_{22.5}$ (ZAC+Al) alloy upon cooling. Cooling rate is obtained by taking derivative of temperature with respect to time.

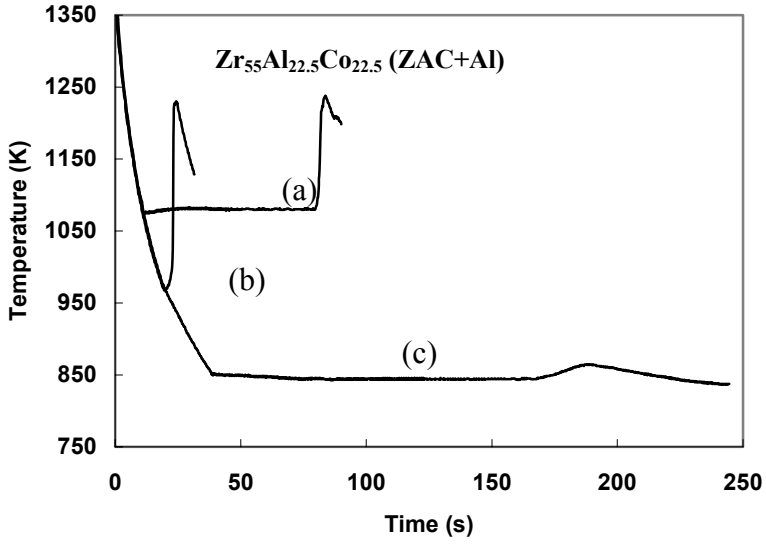

Figure 5.3: Isothermal treatments to obtain TTT curve for $Zr_{55}Al_{22.5}Co_{22.5}$ (ZAC+Al) for temperatures (a) 1080 K, (b) 970 K, and (c) 845 K.

The TTT curves measured for the three samples are summarized in Figure 5.4. The starting of the isothermal anneal time at each temperature was used as the time origin (t=0) for the TTT curves. The TTT curve for ZAC is shown in Figure 5.4 (a). The shortest time for crystallization ("nose" of TTT) is about 3 seconds and occurs at a temperature of 965 K. The isothermal crystallization time increases as the temperature is lowered from 965 K down to 930 K. Thereafter, the isothermal crystallization times decrease again, resulting in a second "nose" at a temperature of 890 K with isothermal time of about 5 seconds. The solidus, liquidus and glass transition temperatures are indicated on the figure. Figure 5.4 (b) is the TTT curve for ZAC+Al showing the typical "C" shape with a "nose" temperature of 970 K, with "nose" time of about 2 seconds. Thus, addition of a small amount of aluminum at the expense of cobalt eliminated the "double-nose" structure. The TTT curve for ZAC+Cu again shows two noses as depicted in Figure 5.4 (c). The shortest time for crystallization is about 3.5 seconds and occurs at a temperature of 943 K.

To gain insight into the nature of crystalline phases formed and the nature of the TTT curves, x-ray scans were performed for each of the samples crystallized after isothermal annealing at different undercoolings. The XRD spectra for ZAC and ZAC+Al are shown in Figures 5.5 and 5.6, respectively. The spectra for ZAC+Cu are very similar to that of ZAC and are not indicated. For ZAC (Figure 5.5), isothermal annealing at 1000 K, which is above the top nose, leads to formation of a mixture of Zr_6Al_2Co and $ZrAl_{0.6}Co_{1.4}$ crystalline phases, as shown by the peak positions. However, below the lower nose at a temperature of 850 K, only Zr_6Al_2Co phase is formed. The sample freely

cooled down to room temperature showed only broad diffraction maxima, typical of an amorphous structure, which is further confirmed by DSC measurement. The TTT curve for ZAC+Al shows a single nose. XRD spectra for ZAC+Al were obtained (as shown in Figure 5.6) after annealing at two different temperatures, one above the nose (1050 K) and the other, below the nose temperature (880 K). The same crystalline phases are formed for both the temperatures, consisting of a mixture of Zr_6Al_2Co, $ZrAl_{0.6}Co_{1.4}$ and other unidentified phases [5]. The amorphous nature of the freely cooled sample is again indicated by the broad diffraction maxima.

The TTT curve for ZAC+Al (Figure 5.4 (b)) has a single nose and the same crystalline phases are formed over the temperature range of the entire TTT curve as shown by the XRD studies at different undercoolings (Figure 5.6). However, a slight change in composition to ZAC or ZAC+Cu changes the crystallization pathways drastically. The “double-nose” TTT curves for these two compositions are the result of different crystalline phases being stable at different undercoolings, as shown by the XRD spectra in Figure 5.5. For ZAC and ZAC+Cu, the TTT curves for two different phases overlap - the lower TTT curve corresponding to the Zr_6Al_2Co crystalline phase, and the upper TTT curve corresponding to the mixture of Zr_6Al_2Co and $ZrAl_{0.6}Co_{1.4}$ crystalline phases. Thus, the combined XRD and TTT curve study suggests that the crystallization pathway for the Zr-Al-Co alloys is very sensitive to slight changes in composition. The critical cooling rates for vitrification are estimated from the TTT curves to be 16.5 K/s, 17.5 K/s and 16.0 K/s for ZAC, ZAC+Al, and ZAC+Cu, respectively. The GFA of the quaternary alloy, ZAC+Cu, is marginally better than the ternary alloys, which is in line with the “confusion principle” mentioned earlier [1].

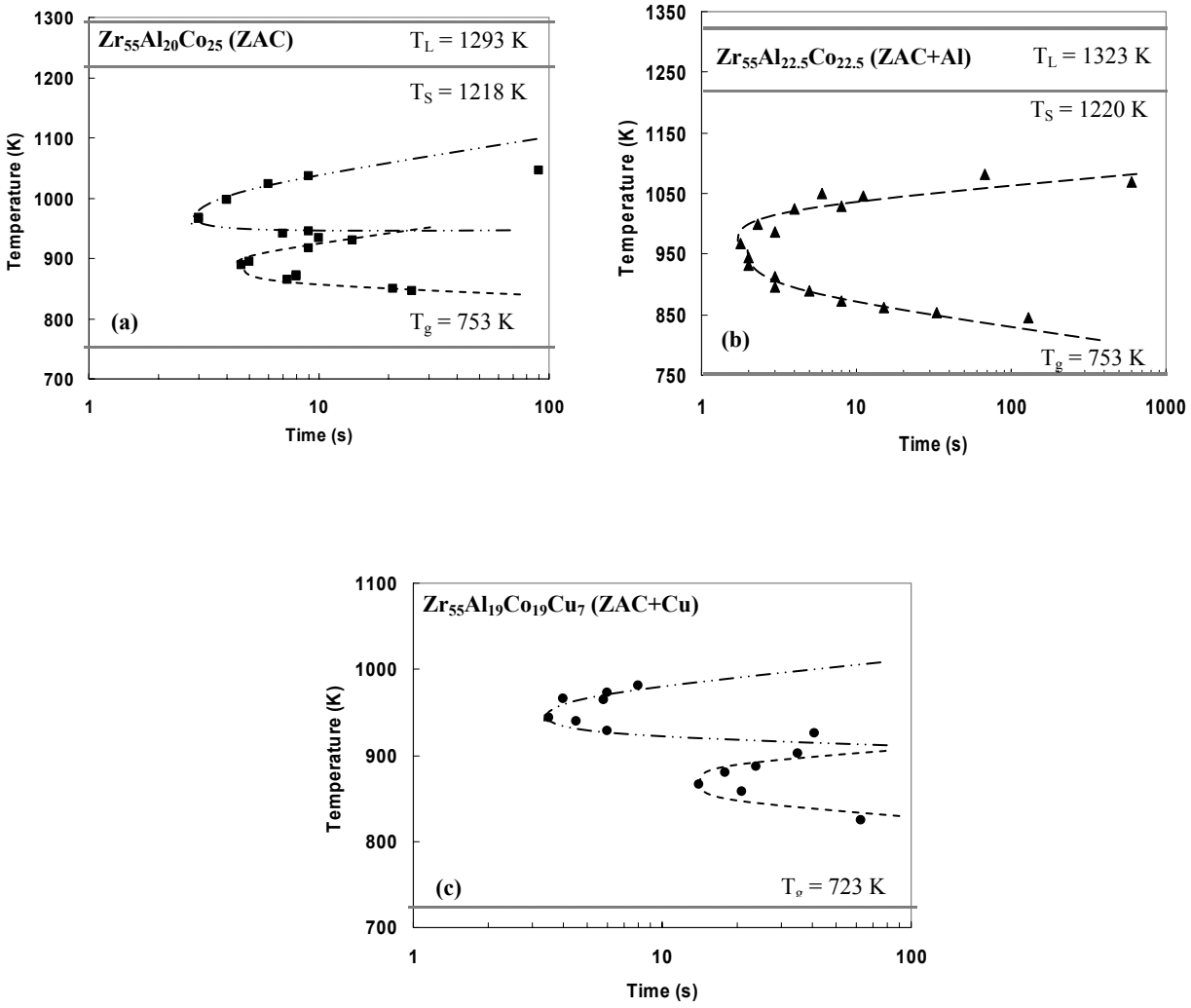

Figure 5.4: TTT Curves for (a) $Zr_{55}Al_{20}Co_{25}$ (ZAC), (b) $Zr_{55}Al_{22.5}Co_{22.5}$ (ZAC+Al), and (c) $Zr_{55}Al_{19}Co_{19}Cu_7$ (ZAC+Cu). The glass transition, solidus and liquidus temperatures are indicated on the figures. The lines connecting the data points are provided as a guide to the eye.

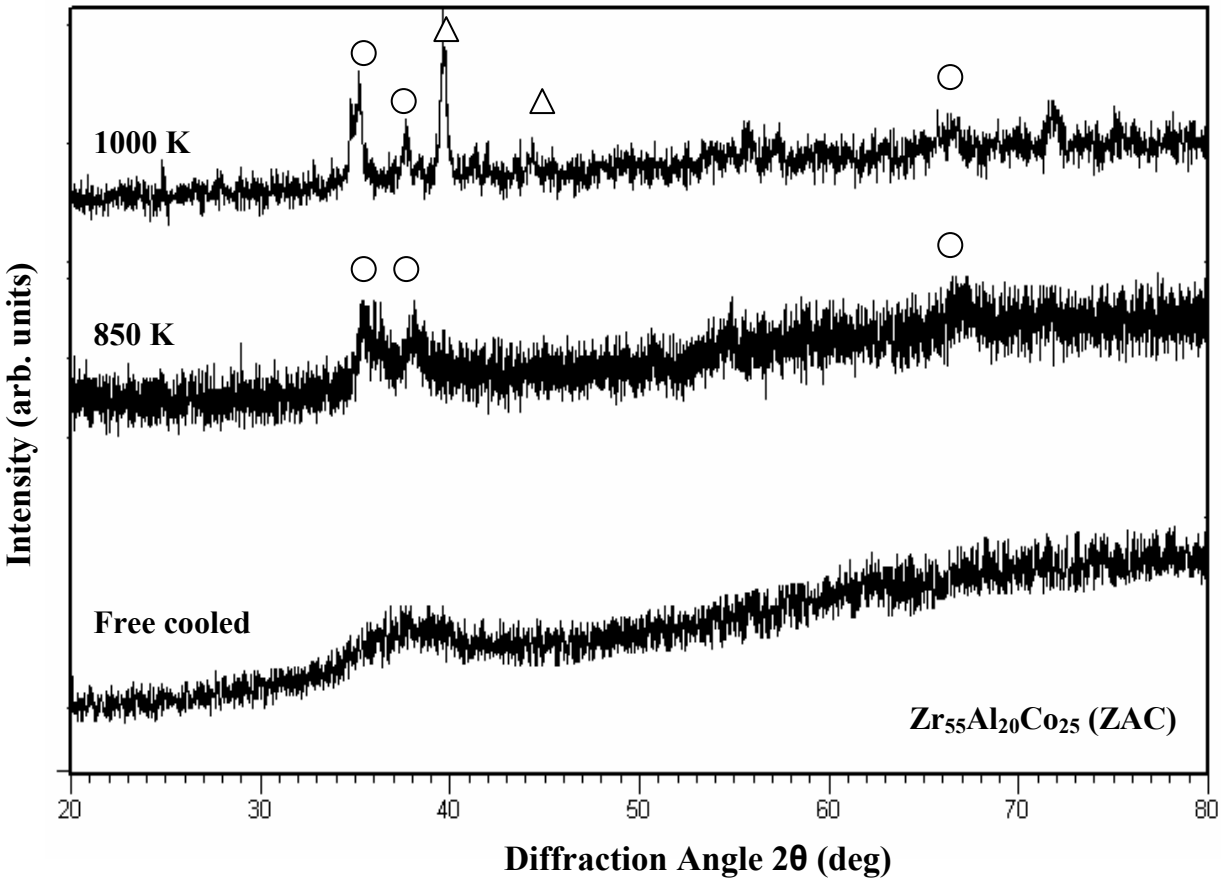

Figure 5.5: X-ray diffraction spectra taken on freely cooled samples and after isothermal anneals at two different undercoolings for $Zr_{55}Al_{20}Co_{25}$ (ZAC). The isothermal anneal temperatures are indicated on the figures. The open circles correspond to the diffraction peaks for Zr_6Al_2Co and the open triangles correspond to the diffraction peaks for $ZrAl_{0.6}Co_{1.4}$. Isothermal annealing at 1000 K leads to formation of a mixture of Zr_6Al_2Co and $ZrAl_{0.6}Co_{1.4}$ crystalline phases, and at 850 K, to formation of only Zr_6Al_2Co phase, explaining the "double-nose" TTT curve.

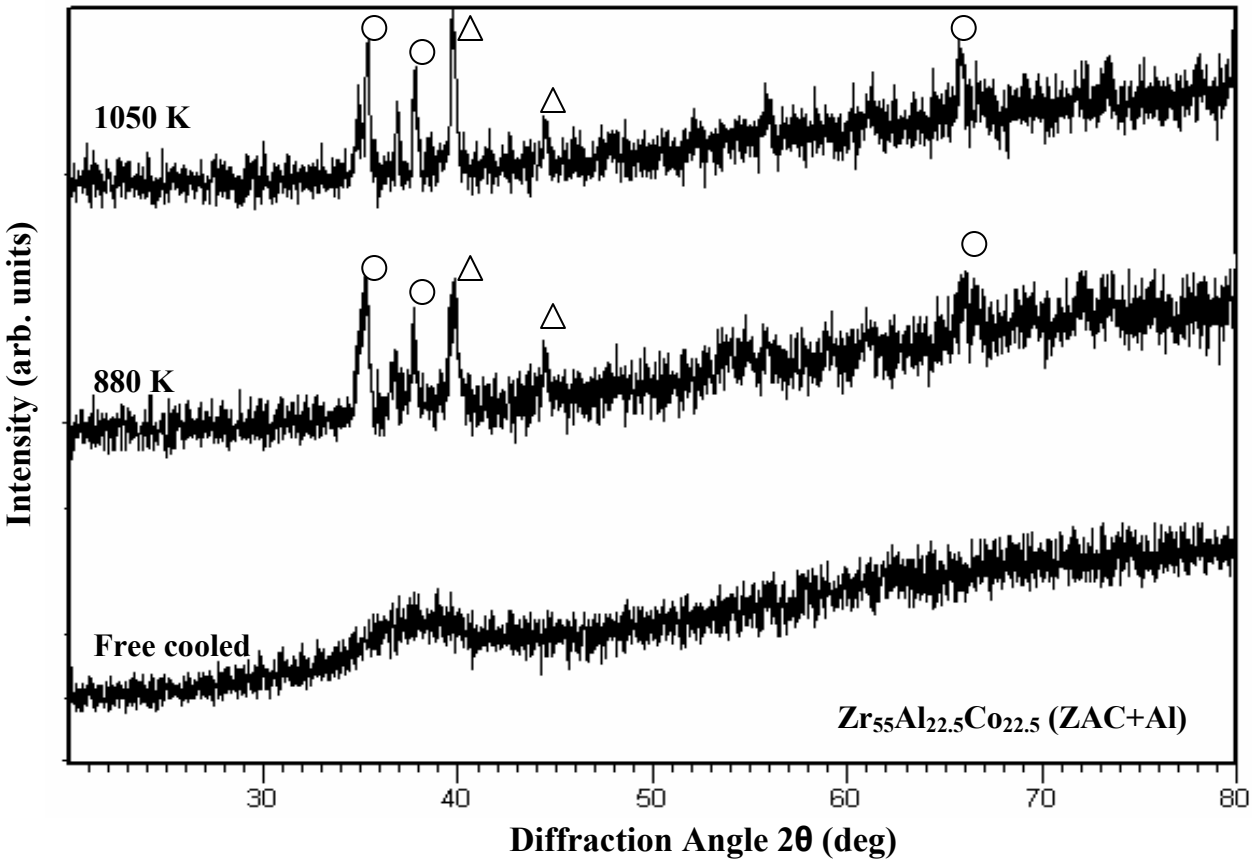

Figure 5.6: X-ray diffraction spectra taken on freely cooled samples and after isothermal anneals at two different undercoolings for $Zr_{55}Al_{22.5}Co_{22.5}$ (ZAC+Al). The isothermal anneal temperatures are indicated on the figures. The open circles correspond to the diffraction peaks for Zr_6Al_2Co and the open triangles correspond to the diffraction peaks for $ZrAl_{0.6}Co_{1.4}$. The same crystalline phases are formed for both undercooling levels, consisting of a mixture of Zr_6Al_2Co, $ZrAl_{0.6}Co_{1.4}$ and other unidentified phases, supporting the "single-nose" TTT curve.

5.4 Conclusions

The following conclusions can be drawn from the study of Zr-Al-Co-(Cu) bulk metallic glass forming alloys using the non-contact electrostatic levitation technique:

(1) Free radiative cooling in the electrostatic levitator could vitrify the three alloys in the Zr-Al-Co-(Cu) system: $Zr_{55}Al_{20}Co_{25}$, $Zr_{55}Al_{22.5}Co_{22.5}$ and $Zr_{55}Al_{19}Co_{19}Cu_7$. This allowed for the first time the determination of Time-Temperature-Transformation (TTT) curves for ternary metallic alloys by isothermal annealing over a wide temperature range between the liquidus and glass transition temperatures.

(2) Combined X-ray diffraction and TTT curve study suggest that the crystallization pathway for the Zr-Al-Co-(Cu) alloys is very sensitive to slight changes in composition. While the TTT curve for $Zr_{55}Al_{22.5}Co_{22.5}$ shows the expected "C" shape with a single "nose", the TTT curves for the other two alloys show two noses. X-ray diffraction study shows that the double-nose structure for $Zr_{55}Al_{20}Co_{25}$ and $Zr_{55}Al_{19}Co_{19}Cu_7$ is caused by the overlap of TTT curves for two different crystalline phases. The lower TTT curve corresponds to the Zr_6Al_2Co crystalline phase and the upper TTT curve corresponds to the mixture of Zr_6Al_2Co and $ZrAl_{0.6}Co_{1.4}$ crystalline phases. For $Zr_{55}Al_{22.5}Co_{22.5}$, the same crystalline phases (mixture of Zr_6Al_2Co, $ZrAl_{0.6}Co_{1.4}$ and other unidentified phases) are formed over the temperature range of the entire TTT curve, which is supported by the single nose.

(3) The average critical cooling rate for glass formation of the Zr-Al-Co-(Cu) alloys estimated from the measured TTT curves is about 17 K/s. This value of critical cooling rate is supported by the trends in the melting temperature viscosity, fragility behavior, and volume change upon crystallization compared to other glass forming systems as discussed in chapter 3.

5.5 References

[1] A. L. Greer, Nature (London) **366**, 303 (1993).

[2] T. Zhang and A. Inoue, Mater. Trans. JIM **43**, 267 (2002).

[3] W. L. Johnson, MRS Bulletin **10**, 42 (1999).

[4] A. Inoue, Acta Mater. **48**, 279 (2000).

[5] S. Mukherjee, H. –G. Kang, W. L. Johnson, and W. K. Rhim, Phys. Rev. B **70**, 174205 (2004).

Chapter 6

Correlation Between Crystal-Melt Interfacial Tension, Melt Viscosity, and Glass Forming Ability

Abstract

The Time-Temperature-Transformation (TTT) curves for three bulk metallic glass-forming alloys, $Zr_{41.2}Ti_{13.8}Cu_{12.5}Ni_{10}Be_{22.5}$ (Vit1), $Zr_{57}Cu_{15.4}Ni_{12.6}Al_{10}Nb_5$ (Vit106), $Zr_{55}Al_{22.5}Co_{22.5}$ (ZrAlCo), are analyzed within the framework of nucleation theory. These alloys are chosen because of their widely differing glass forming abilities, but otherwise similar properties. The critical cooling rate for vitrification obtained from the TTT curves is about 2 K/s for Vit1, 10 K/s for Vit106, and 18 K/s for ZrAlCo. The Gibbs free energy difference between liquid and crystal for the three alloys is similar and fails to explain the order of magnitude difference in their critical cooling rates. The times for crystallization in these zirconium-based alloys, and therefore their glass forming ability, scale with the melt viscosities. Fitting of the TTT curves shows that the better glass former actually has a lower crystal-melt interfacial tension. This observation is explained by the fact that the icosahedral short-range order of the undercooled liquid on the one hand, lowers the interfacial tension, and on the other, increases the melt viscosity due to denser packing of liquid atoms.

Keywords: Interfacial tension; Viscosity; Nucleation; Icosahedral Order

6.1 Introduction

The stability against crystallization in bulk metallic glass forming systems has been explained by both kinetic and thermodynamic principles [1-3]. From a kinetic point of view, the dynamic viscosity is an important parameter to describe the time scale for structural rearrangement of the liquid atoms in an undercooled state to form a crystal nucleus. From a thermodynamic point of view, the better glass former has a lower thermodynamic driving force for crystallization, which is given by the Gibbs free energy difference between the liquid and crystal, ΔG. Particularly, in classical nucleation theory [4,5], the activation barrier for nucleation, ΔG^* is expressed as:

$$\Delta G^* = \frac{16\pi\sigma^3}{3\Delta G^2}, \qquad (6.1)$$

where σ is the crystal-melt interfacial tension. It is clear from Eq. (6.1) that lower thermodynamic driving force and higher interfacial tension will lead to greater stability of the undercooled melt against crystallization. While both the thermodynamic and the kinetic driving forces govern the overall stability of the undercooled liquid, it is important to identify their relative importance. It is also vital to investigate the correlations between the various factors controlling glass forming ability (GFA) to see whether they stem from the same underlying property of the undercooled liquid.

In this chapter, the influences of ΔG, melt viscosity, and crystal-melt interfacial tension on glass forming ability of three alloys are discussed. The bulk amorphous alloys investigated in this study are: $Zr_{41.2}Ti_{13.8}Cu_{12.5}Ni_{10}Be_{22.5}$ (Vit1), $Zr_{57}Cu_{15.4}Ni_{12.6}Al_{10}Nb_5$

(Vit106), and $Zr_{55}Al_{22.5}Co_{22.5}$ (ZrAlCo). These alloys are chosen for a comparative study because of their widely differing glass forming abilities, but otherwise similar properties. Moreover, the melt viscosities were experimentally obtained as discussed in chapter 3, and the entire TTT curves were measured for these alloys as discussed in chapters 4 and 5. The ΔG was obtained from earlier studies on thermodynamics of these systems. The crystal-melt interfacial tension for each of the alloys was obtained by fitting of the TTT curves with classical nucleation theory.

6.2 Theoretical Background

According to classical nucleation theory (CNT), the time for isothermal crystallization of an undercooled melt, t_x, is given by [5,6]:

$$t_x = \left(\frac{3x}{\pi I_{SS} u^3} \right)^{\frac{1}{4}}, \tag{6.2}$$

where x is the detectable volume fraction during the starting of the crystallization process (a value of 10^{-3} is typically used), I_{SS} is the steady state nucleation rate, and u is the growth rate at a particular undercooling level. The steady state nucleation rate is given by:

$$\mathrm{I_{SS}} = \mathrm{AD_{eff}} \exp\left(- \frac{\Delta G^* f(\theta)}{k_B T} \right), \tag{6.3}$$

where D_{eff} is the effective diffusivity, A is a constant, k_B is the Boltzmann's constant, ΔG^* is the activation barrier for nucleation (Equation (6.1)), and $f(\theta)$ is the catalytic potency

factor which depends on the contact angle, θ, between the crystal nucleus and the catalyst. Assuming a diffusion controlled mechanism, the growth velocity, u, is given by:

$$u = \frac{D_{eff}}{a}\left[1 - \exp\left(-\frac{\Delta G}{k_B T}\right)\right], \tag{6.4}$$

where a is the inter-atomic spacing of the alloy. The effective diffusivity (D_{eff}) is estimated by the Stokes-Einstein equation, $D_{eff}=k_BT/(3\pi\eta a)$, where η is the dynamic viscosity of the liquid. All quantities required for the calculation of steady state nucleation rate (Equation (6.3)) and growth rate (Equation (6.4)) can be experimentally measured, except the interfacial tension (σ), the constant A, and the catalytic potency factor, $f(\theta)$.

To investigate the possible structural effects on the nucleation behavior of phases with different degrees of polytetrahedral order, the negentropic model by Spaepen [7] and Thompson [8] has been used. The interfacial tension following such an approach is given by [7,8]:

$$\sigma = \alpha \frac{T\,\Delta S}{\left(N_A V_{mol}^{\,2}\right)^{1/3}}, \tag{6.5}$$

where α is a factor that depends on the structure difference between the crystal nucleus and the melt, V_{mol} is the molar volume, ΔS is the entropy difference between liquid and crystal, and N_A is Avogadro's number. In earlier studies it was found that α has a value of 0.86 for face centered cubic (FCC) and hexagonal close-packed (HCP) structures, and a value of 0.71 for body centered cubic (BCC) structure [9]. However, α is much smaller (~ 0.3) for icosahedral quasicrystals [10,11] and increases from 0.3 to 0.7 for phases with decreasing polytetrahedral order.

6.3 Results and Discussion

TTT curves for the three alloys, Vit1, Vit106, and ZrAlCo as discussed in chapters 4 and 5 are shown together in Figure 6.1. The fits of the TTT curves using classical nucleation theory (CNT) are also shown in the figure and will be discussed later. All of the three TTT curves have the "C" shape which arises from the competition between increasing thermodynamic driving force for crystallization and decreasing atomic mobility with increasing undercooling. The critical cooling rate (*Rc*) for vitrification is calculated as $Rc = (T_L - T_{nose})/(t_{nose} - t_L + \Delta t_{nose})$, where t_{nose}, and t_L, are the times to reach the nose temperature (T_{nose}) and the liquidus temperature (T_L), respectively during the free radiative cooling, and Δt_{nose} is the isothermal time at the nose before crystallization. The critical cooling rates are about 2 K/s, 10 K/s, and 17 K/s for Vit1, Vit106, and ZrAlCo, respectively. The critical cooling rates vary about an order of magnitude, illustrating the wide range in glass forming abilities of these alloys.

The temperature-dependent Gibbs free energy difference for Vit1 and Vit106 was calculated in earlier publications by integrating the experimentally measured heat capacity differences between undercooled liquid and crystal [12,13]. The Gibbs free energy difference for the two alloys was found to be similar at the same relative undercooling level. The entropy of fusion is experimentally found to be almost identical for the three alloys (ΔS_f = 8.65, 8.5, and 8.7 J/mol/K for Vit1, Vit106 and ZrAlCo, respectively) and ΔG for ZrAlCo is estimated to be very similar to Vit1 and Vit106. Thus, the thermodynamic driving force fails to explain the order of magnitude difference

in the critical cooling rates of these Zr-based bulk amorphous alloys. Lu *et al.* [14] have reported a strong correlation between ΔG and glass forming ability for La-based bulk amorphous alloys. However, they note that Zr-based alloys do not follow the same trend and have larger thermodynamic driving force for crystallization even though they are better glass formers compared to the La-based alloys [14]. This further demonstrates that thermodynamics does not play a crucial role in determining the glass forming ability of Zr-based bulk amorphous alloys.

To study the influence of viscosity on crystallization time scales, the TTT curves for the three alloys are plotted in Figure 6.2 with the temperature axis normalized by their respective glass transition temperatures. For clarity, only the fitting curves are shown because there is reasonable agreement between experimental data and the classical nucleation theory (CNT) fits. The nose temperatures of the three alloys are at the same position of about 1.3 on the normalized temperature axis. On the secondary *y*-axis of Figure 6.2 are shown the dynamic viscosities of the three alloys at the nose temperatures which are obtained as described in chapter 3. The viscosities differ by almost two orders of magnitude. The almost two orders of magnitude difference in the crystallization times of the alloys can be explained by the two orders of magnitude difference in their viscosities ($t_x \sim \eta$). Thus, it is clear from Figure 6.2 that dynamic viscosity plays the most decisive role in determining the critical cooling rates of these alloys.

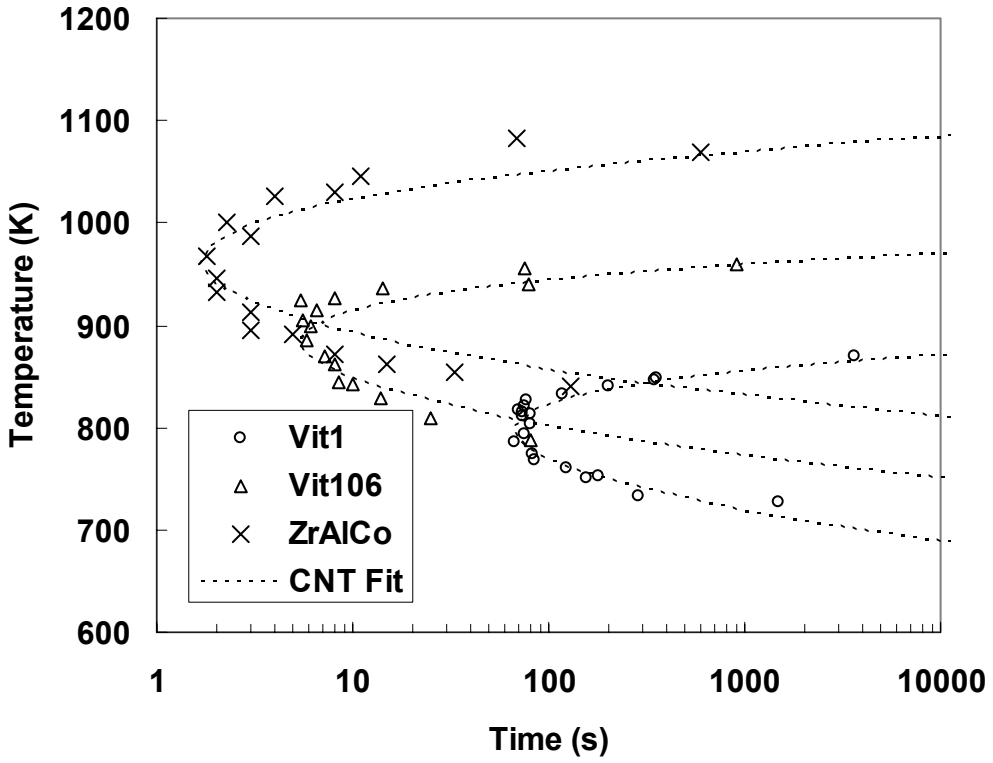

Figure 6.1: TTT curves of $Zr_{41.2}Ti_{13.8}Cu_{12.5}Ni_{10}Be_{22.5}$ (Vit1), $Zr_{57}Cu_{15.4}Ni_{12.6}Al_{10}Nb_5$ (Vit106), and $Zr_{55}Al_{22.5}Co_{22.5}$ (ZrAlCo) and the classical nucleation theory (CNT) fits.

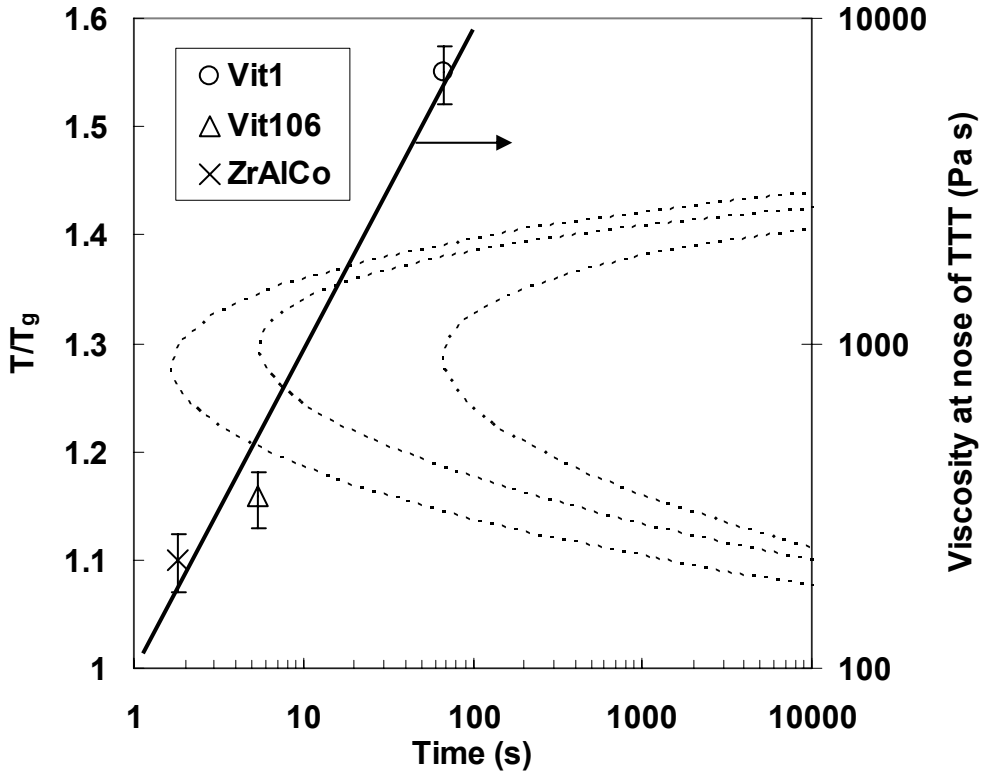

Figure 6.2: TTT fitting curves for the three alloys with temperature axis normalized by the glass transition temperature (T_g). In order of increasing nose times, the TTT curves correspond to $Zr_{55}Al_{22.5}Co_{22.5}$ (ZrAlCo), $Zr_{57}Cu_{15.4}Ni_{12.6}Al_{10}Nb_5$ (Vit106), and $Zr_{41.2}Ti_{13.8}Cu_{12.5}Ni_{10}Be_{22.5}$ (Vit1). The secondary *y*-axis shows the dynamic viscosities of the three alloys at the nose temperature of the TTT curves. Error bars in viscosity of ±20% are shown. The viscosity scales linearly with the crystallization time at the nose temperature.

To obtain the crystal-melt interfacial tension, the TTT curves are fitted with classical nucleation theory (CNT) Eq. (6.1) to Eq. (6.4). The inter-atomic spacing is estimated from the measured specific volumes as described in chapter 2, and an average value of 2.55 ^{o}A is used for all the three alloys. The data for temperature dependence of viscosity for the three alloys is discussed in chapter 3. The entropy difference between the liquid and crystal decreases with deeper undercooling until it vanishes at the Kauzmann temperature [15]. Microstructural investigations for Zr-based bulk amorphous alloys have revealed a high density of nanocrystals with greater refinement at deeper undercoolings which suggests drastic reduction in the nucleation barrier close to the glass transition temperature [16,17]. A number of mechanisms have been proposed to account for this experimental observation [18-20]. To incorporate this effect in CNT, we used temperature dependent entropy [12,13] in Eq. (6.5), which makes the interfacial tension disappear at the Kauzmann temperature. The TTT curves were fitted using α and A as the only variable parameters, while $f(\theta)$ is assumed to be 1. The values of A are 8×10^{28}, 7×10^{25}, and 5×10^{30} m^{-5} for Vit1, Vit106, and ZrAlCo, respectively. The values of α are 0.35, 0.47, and 0.52 for Vit1, Vit106, and ZrAlCo, respectively. The validity of assuming homogeneous nucleation ($f(\theta)$=1) for thermally fluxed, containerlessly processed samples is discussed elsewhere [21]. It was noted that the value of α was rather insensitive to large variations in other quantities involved in the CNT equations.

Vit1 has α value of 0.35 which indicates that the Vit1 melt would form icosahedral quasicrystals. This supports the experimental finding of Waniuk *et al.* [22] who reported the formation of metastable, icosahedral quasicrystals in Vit1 as the

intermediate step, prior to transformation of the melt to other stable crystalline phases. The two-step recalescence events observed for Vit1 in this study during isothermal anneals at deep undercoolings (chapter 4) is suggestive of the same behavior. The values of α for the other two alloys suggest the formation of intermediate phases with lower polytetrahedral order (α=0.47 and 0.52 for Vit106 and ZrAlCo respectively) compared to Vit1. However, the relatively faster kinetics in these two systems did not allow the identification of the intermediate metastable structures.

The low values of α in a glass forming alloy compared to pure metals, and the nucleation of icosahedral quasicrystals indicate a high degree of polytetrahedral order in the undercooled liquid. Recent *in situ* experiments [23] provide direct evidence of icosahedral short-range order (ISRO) in undercooled alloy melts. This high degree of ISRO lowers the interfacial tension and favors easy formation of quasicrystals and has in fact, been observed for a number of zirconium-based metallic glasses [24,25]. According to a recent paper by Xing *et al.* [26] on the Zr-Ti-Cu-Ni-Al system, "Given the local icosahedral coordination of the undercooled liquid, leading to easy formation of icosahedral clusters, it is surprising that these glasses can be cast at low cooling rates." Our results suggest that the explanation for these anomalous experimental findings is that the ISRO of the undercooled liquid affects its dynamic viscosity as well. The greater the degree of icosahedral order in the undercooled liquid (i.e., the smaller the value of α in Eq. (6.5)), the higher the packing density of atoms. In fact, an icosahedral packing of distorted tetrahedra is denser than FCC or HCP structures [25,27]. From free volume theory [28] and recent experimental results on bulk glass-forming melts [29], it is known that the lesser the free volume of the liquid, the higher its viscosity. The above trend in α

value ($\alpha^{Vit1}<\alpha^{Vit106}<\alpha^{ZrAlCo}$) suggests that the Vit1 melt has the highest degree of polytetrahedral order. The high degree of polytetrahedral order in the case of Vit1 contributes significantly towards its high viscosity and low critical cooling rate for vitrification compared to the other two alloys. Thus, this study suggests that ISRO has two opposing influences on the stability of the undercooled liquid. On the one hand, it lowers the interfacial tension for formation of icosahedral quasicrystals, while on the other, it increases the viscosity, thereby slowing down the kinetics. While it is difficult to quantify each influence, the lower interfacial tension caused by a high degree of ISRO does not seem to affect the glass forming ability of an alloy significantly. On the other hand, the higher melt viscosity plays the most decisive role in determining the glass forming ability of Zr-based bulk amorphous alloys. Roughly, the time for crystallization scales with the dynamic viscosity of the melt.

The steady state nucleation rate (I_{SS}) and growth rate (u) calculated by fitting of the TTT curve for one of the alloys, Vit1 is shown in Figure 6.3. The maximum in nucleation rate occurs at a much lower temperature (720 K), compared to the maximum in the growth rate (960 K). This asymmetry in the nucleation rate and growth rate explains the "C" nature of the TTT curve. The nose of the TTT curve for Vit1 is at a temperature of 800 K. The SEM backscatter images obtained for Vit1 in this study after isothermal crystallization in the ESL at two different undercoolings are shown in Figure 6.4. The microstructure obtained after isothermal annealing at a temperature of 850 K - above the nose of the TTT - is shown in Figure 6.4 (a). The morphology consists of multiphase eutectic structure. The crystallization starts at certain nucleation centers and this is followed by growth until there is impingement upon the neighboring embryos. On

the other hand, the nucleation density obtained after annealing at 740 K which is below the TTT nose is shown in Figure 6.4 (b). The morphology in this case is hard to identify, but the nucleation centers appear as dark spots (shown by arrows). However, there is very limited growth. It is clear from the two figures, by comparing the scale of the microstructure that the density of nucleation centers obtained at the higher temperature of 850 K is much less compared to that obtained at the lower temperature of 740 K. This clearly demonstrates the increase in the nucleation rate with deeper undercooling.

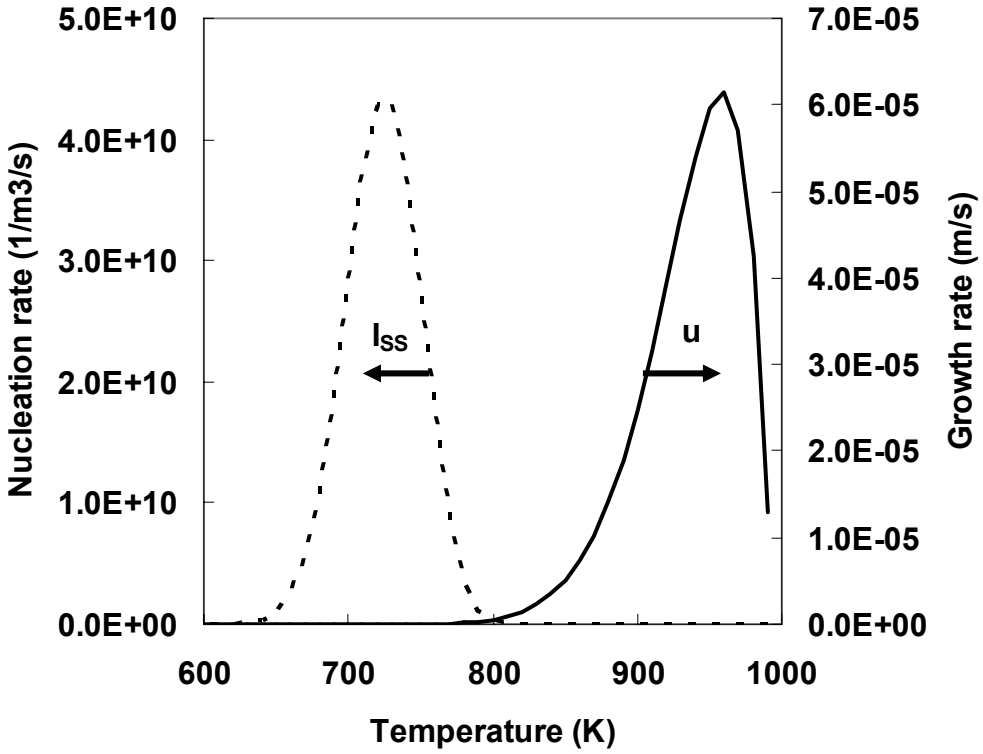

Figure 6.3: Nucleation rate and growth rate for Vit1, calculated using Eq. (6.3) and Eq. (6.4) by fitting the TTT curve. The peak in nucleation rate is at 720 K and in growth rate at 960 K. The nose of the TTT curve is at 800 K. This asymmetry in nucleation and growth rates gives rise to the "C" nature of the TTT curve.

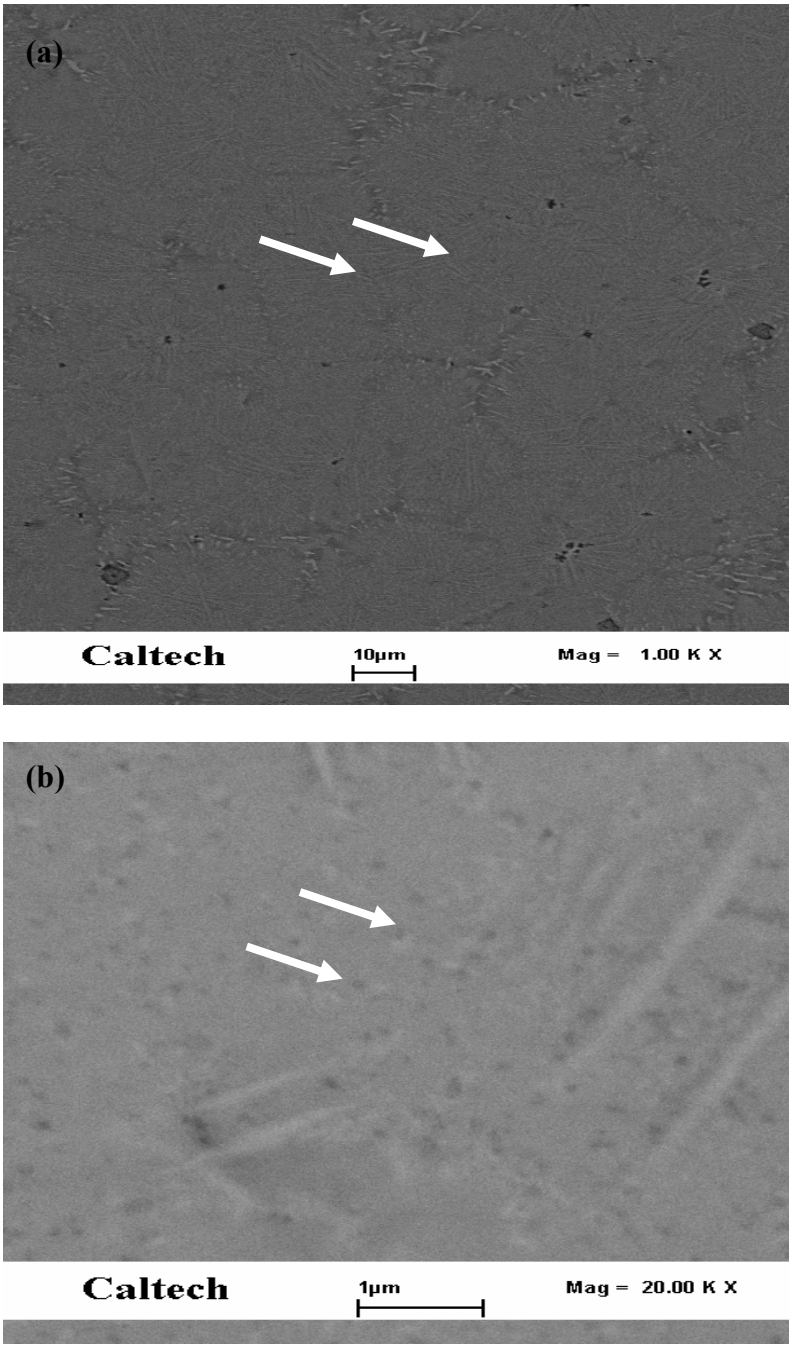

Figure 6.4: SEM backscatter images showing the nucleation density obtained in Vit1 after isothermal annealing at (a) 850 K (above the nose), and (b) 740 K (below the nose).

6.4 Conclusions

The following conclusions can be drawn by analyzing the Time-Temperature-Transformation curves of three bulk metallic glass-forming alloys, $Zr_{41.2}Ti_{13.8}Cu_{12.5}Ni_{10}Be_{22.5}$ (Vit1), $Zr_{57}Cu_{15.4}Ni_{12.6}Al_{10}Nb_5$ (Vit106), $Zr_{55}Al_{22.5}Co_{22.5}$ (ZrAlCo), within the framework of nucleation theory:

(1) The Gibbs free energy difference between liquid and crystal for the three alloys is similar, which fails to explain the order of magnitude difference in their critical cooling rates. The critical cooling rate for vitrification, obtained from the TTT curves, is about 2 K/s for Vit1, 10 K/s for Vit106, and 18 K/s for ZrAlCo. The time for crystal nucleation in these bulk metallic glasses, and therefore their glass forming ability, scales with the melt viscosity.

(2) Fitting of the TTT curves using classical nucleation theory and negentropic model shows that the better glass former actually has a lower crystal-melt interfacial tension. The trend in interfacial tension, $\alpha^{Vit1}<\alpha^{Vit106}<\alpha^{ZrAlCo}$, suggests that Vit1 melt has the highest degree of polytetrahedral order, while ZrAlCo has the lowest degree. Icosahedral quasi-crystal formation has been observed for a number of Zr-based bulk metallic glasses, suggesting a high degree of icosahedral coordination in the undercooled liquid. This observation is explained by the fact that the icosahedral short-range order of the undercooled liquid on the one hand, lowers the interfacial tension for formation of quasi-crystals, while on the other, increases the melt viscosity due to denser packing of liquid atoms.

(3) Fitting of the TTT curves with nucleation theory shows that the maximum in nucleation rate occurs at a much lower temperature compared to the maximum in growth rate, explaining the “C” nature of the TTT curve. The increase in nucleation density with increasing undercooling is confirmed from SEM study of the samples crystallized after isothermal annealing at different undercoolings.

6.5 References

[1] C. A. Angell, Science **267**,1924 (1995).

[2] W. L. Johnson, MRS Bulletin **10**, 42 (1999).

[3] G. Wilde, G. P. Gorler, R. Willnecker, and H. J. Fecht, J. Appl. Phys. **87**, 1141 (2000).

[4] J. W. Christian, *The Theory of Transformations in Metals and Alloys* (Pergamon, Oxford, 2002).

[5] K. F. Kelton, Solid State Phys. **45**, 75 (1991).

[6] D. R. Uhlmann, J. Non-Cryst. Solids **7**, 337 (1972).

[7] F. Spaepen, Acta Metall. **23**, 729 (1975).

[8] C. V. Thompson, Ph.D. Thesis, Harvard University, 1981.

[9] C. V. Thompson and F. Spaepen, Acta Metall. **31**, 2021 (1983).

[10] D. M. Herlach, F. Gillessen, T. Volkmann, M. Wollgarten, and K. Urban, Phys. Rev. B **46**, 5203 (1992).

[11] D. Holland-Moritz, J. Schroers, D. M. Herlach, B. Grushko, and K. Urban, Acta Mater. **46**, 1601 (1998).

[12] S. C. Glade, R. Busch, D. S. Lee, W. L. Johnson, R. K. Wunderlich, and H. J. Fecht, J. Appl. Phys. **87**, 7242 (2000).

[13] R. Busch, Y. J. Kim, and W. L. Johnson, J. Appl. Phys. **77**, 4039 (1995).

[14] Z. P. Lu, X. Hu, and Y. Li, Intermetallics **8**, 477 (2000).

[15] W. Kauzmann, Chem. Rev. **43**, 219 (1948).

[16] J. Schroers, R. Busch, A. Masuhr, and W. L. Johnson, Appl. Phys. Lett. **74**, 2806 (1999).

[17] A. Revesz, P. Donnadieu, J. P. Simon, P. Goyut, and P. Ochin, Phil. Mag. Lett. **81**, 767 (2001).

[18] W. -H. Wang, Q. Wei, S. Friedrich, M. P. Macht, N. Wanderka, and H. Wollenberger, Appl. Phys. Lett. **71**, 1053 (1997).

[19] C. T. Liu, M. F. Chisholm, and M. K. Miller, Intermetallics **10**, 1105 (2002).

[20] H. Assadi and J. Schroers, Acta Mater. **50**, 89 (2002)

[21] S. Mukherjee, Z. Zhou, J. Schroers, W. L. Johnson, and W. K. Rhim, Appl. Phys. Lett. **84**, 5010 (2004).

[22] T. Waniuk, J. Schroers, and W. L. Johnson, Phys. Rev. B **67**, 184203 (2003).

[23] K. F. Kelton, G. W. Lee, A. K. Gangopadhyay, R. W. Hyers, T. J. Rathz, J. R. Rogers, M. B. Robinson, and D. S. Robinson, Phys. Rev. Lett. **90**, 195504 (2003).

[24] N. Wanderka, M. –P. Macht, M. Seidel, S. Mechler, K. Stahl, and J. Z. Jiang, Appl. Phys. Lett. **77**, 3935 (2000).

[25] K. F. Kelton, J. Non-Cryst. Solids **334-335**, 253 (2004).

[26] L. Q. Xing, Y. T. Shen, and K. F. Kelton, Appl. Phys. Lett. **81**, 3371 (2002).

[27] D. Xu, G. Duan, and W. L. Johnson, Phys. Rev. Lett. **92**, 245504 (2004).

[28] M. H. Cohen and G. S. Grest, Phys. Rev. B **20**, 1077 (1979).

[29] S. Mukherjee, J. Schroers, Z. Zhou, W. L. Johnson, and W. K. Rhim, Acta Mater. **52**, 3689 (2004).

Chapter 7

Crystallization Behavior of an *in situ* Ductile Phase Reinforced Amorphous-Matrix Composite

Abstract

The crystallization behavior, microstructure, specific volume, and viscosity of the *in situ* ductile β phase reinforced amorphous-matrix composite, $Zr_{56.2}Ti_{13.8}Nb_{5.0}Cu_{6.9}Ni_{5.6}Be_{12.5}$, are investigated as a function of the processing temperature. The melting point of the ductile β phase which is much higher than the melting temperature of the matrix is obtained from the viscosity measurements to be around 1420 K. The viscosity of the β composite after melting of the β dendrites is much lower than the best BMG investigated in this study, $Zr_{41.2}Ti_{13.8}Cu_{12.5}Ni_{10}Be_{22.5}$ (Vit1). Upon cooling the β composite from temperatures above 1420 K, β dendrites nucleate at a certain undercooling and result in severe distortion of the sample as seen from the specific volume data. Also, there is non-uniform distribution of the β dendrites as seen from the microstructure. However, cooling from temperatures below 1420 K preserves the shape of the sample and results in uniform distribution of the β dendrites. Based on the experimental results, an optimum processing route is suggested.

Keywords: In situ Composite; Dendritic Microstructure; Viscosity

7.1 Introduction

Despite high strength and elastic limit, glassy alloys show very limited plasticity [1,2]. They fail by the formation of highly localized shear bands, leading to catastrophic failure under unconstrained conditions. To overcome this problem, a new class of ductile phase reinforced bulk metallic glass composites has been made by the *in situ* processing method [3,4]. The microstructure of the resulting material consists of a ductile crystalline phase embedded in a fully amorphous matrix [4]. This microstructure leads to remarkable improvements in impact toughness and plasticity. The mechanism that has been suggested to account for this improvement is the interaction of shear bands nucleated in the amorphous matrix with the *in situ* ductile phase acting against shear localization and critical crack propagation [5].

An *in situ* composite whose mechanical properties have been extensively studied is the zirconium based alloy, $Zr_{56.2}Ti_{13.8}Nb_{5.0}Cu_{6.9}Ni_{5.6}Be_{12.5}$ (referred to as β composite) [4-6] which exhibits much greater toughness and ductility compared to the monolithic bulk metallic glass (BMG) matrix. The microstructure for this composite consists of 25% by volume of a body-centered-cubic (bcc) phase (or β phase) of composition $Zr_{71}Ti_{16.3}Nb_{10}Cu_{1.8}Ni_{0.9}$ embedded in 75% by volume of an amorphous phase of composition $Zr_{47}Ti_{12.9}Nb_{2.8}Cu_{11}Ni_{9.6}Be_{16.7}$. The properties of the monolithic BMG matrix are very similar to $Zr_{41.2}Ti_{13.8}Cu_{12.5}Ni_{10}Be_{22.5}$ (Vit1). The mechanical properties of this composite have been well-studied [6]. However, data for thermophysical properties such as viscosity and specific volume are lacking. The measurement and characterization of

crystallization behavior and thermophysical properties are important for optimization of processing conditions.

In this chapter, the crystallization behavior, specific volume and viscosity of the *in situ* β composite, $Zr_{56.2}Ti_{13.8}Nb_{5.0}Cu_{6.9}Ni_{5.6}Be_{12.5}$, are investigated. The melting point of the ductile β phase dendrites which is much higher than the matrix melting temperature is obtained from the viscosity measurements. The influence of overheating to temperatures above and below the β phase melting point on volume, crystallization behavior, and microstructure of the alloy is discussed.

7.2 Results and Discussion

Samples of the β composite were levitated and melted in the electrostatic levitator (ESL). The free radiative cooling curves obtained for the composite under two different conditions are shown in Figure 7.1. Overheating the melt to temperatures greater than 1420 K prior to free radiative cooling results in two recalescence events - a sharp peak at 1055 K and a broad peak around 915 K. However, for overheating below 1420 K, only a single broad recalescence event is observed. The melting point of the matrix could be identified from the heating curve and matches with the value obtained from DSC measurement. However, the melting point of the ductile β phase which is much higher than the matrix melting point could not be identified from the heating and cooling curves. It was obtained indirectly from viscosity measurements.

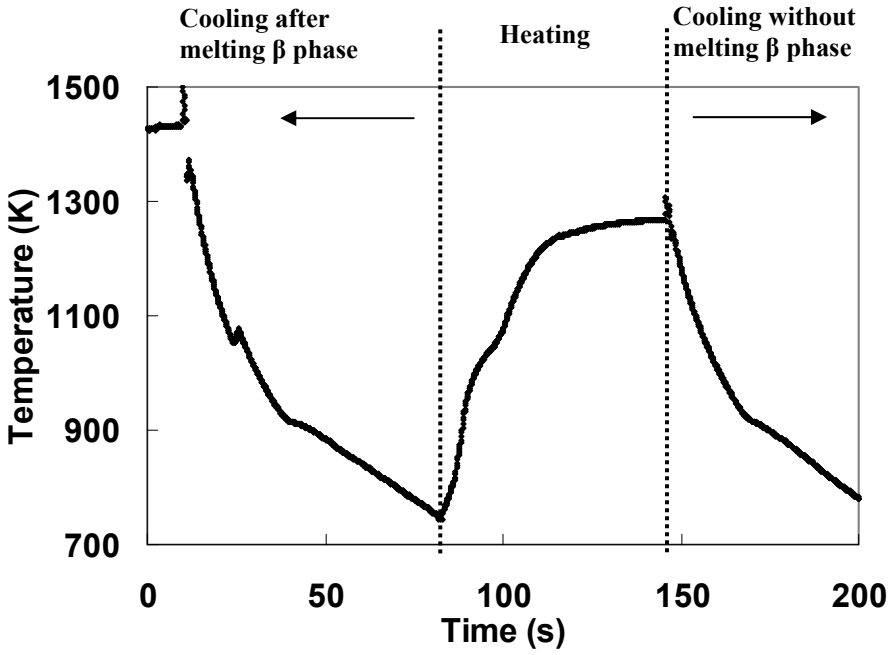

Figure 7.1: Free radiative cooling curves for the β composite obtained with and without melting of the β phase. The melting temperature of the β phase was obtained from viscosity measurements to be 1420 K.

On cooling down from above 1420 K, the viscosity could be measured down to 1080 K. However, upon heating up from room temperature, the sample could not be oscillated until the temperature was raised up to 1420 K, at which point, it started oscillating vigorously. During both heating up and cooling down, the same decay times were obtained at each temperature. From the viscosity measurement, the melting temperature of the β phase is estimated to be close to 1420 K. This agrees reasonably with the recent *in situ* X-ray diffraction studies on the β composite by Lee [7]. In the presence of the β phase dendrites, the sample is too stiff to be oscillated. But once the β dendrites are melted by going above 1420 K, the sample can be oscillated easily down to a temperature of 1055 K, at which point, the β phase nucleates. The viscosity values for the β composite are shown in Figure 7.2 in comparison with the values for Vit1. It is clear that the β composite melt without the β dendrites has much lower viscosity than Vit1. However, once the β dendrites are formed, the material becomes very stiff. This knowledge is very important in commercial processing of β composites.

The specific volume data obtained for the two different processing conditions, along with the cooling curves, are shown in Figures 7.3 and 7.4. For overheating level above the β phase melting temperature, there is severe distortion of the sample upon nucleation of the β phase (first sharp recalescence). For overheating level below the β phase melting temperature, the sample remains fairly spherical even after the broad recalescence. The nucleation of the highly directional β dendrites at the first recalescence peak causes the distortion of the sample, as shown by the large scatter in the volume data in Figure 7.3. The second broad recalescence peak suggests partial crystallization of the

matrix, although the amount crystallized is likely to be very small, judging by the amount of heat released. However, the second recalescence does not change the noise level in the volume data appreciably. In the case shown for Figure 7.4, the matrix is molten while the β dendrites remain in the melt and are uniformly distributed. Upon cooling, the matrix crystallizes partially as shown by the broad recalescence. The partial crystallization of the matrix causes a slight increase in the noise level for specific volume, although the distortion is much less compared to the case of Figure 7.3.

The microstructures obtained under the two different processing conditions are shown in Figure 7.5. With lower overheating, there is uniform distribution of dendrites, with the matrix forming an envelope as shown in Figure 7.5 (a). In the case of higher overheating, the β phase melts and then subsequently nucleates at a certain undercooling. There is extensive dendrite growth in patches as shown in Figure 7.5 (b). However, the distribution of dendrites is not uniform, as in the case of Figure 7.5 (a). Heating the β composite above the β phase melting temperature will result in significant lowering of the melt viscosity, thus making it much easier for processing. However, casting the alloy from this temperature will result in non-uniform distribution of the dendrites. Hence, this should be followed by raising the sample to a temperature between the matrix and β phase melting points to ensure uniform distribution of the dendrites and less volume distortion.

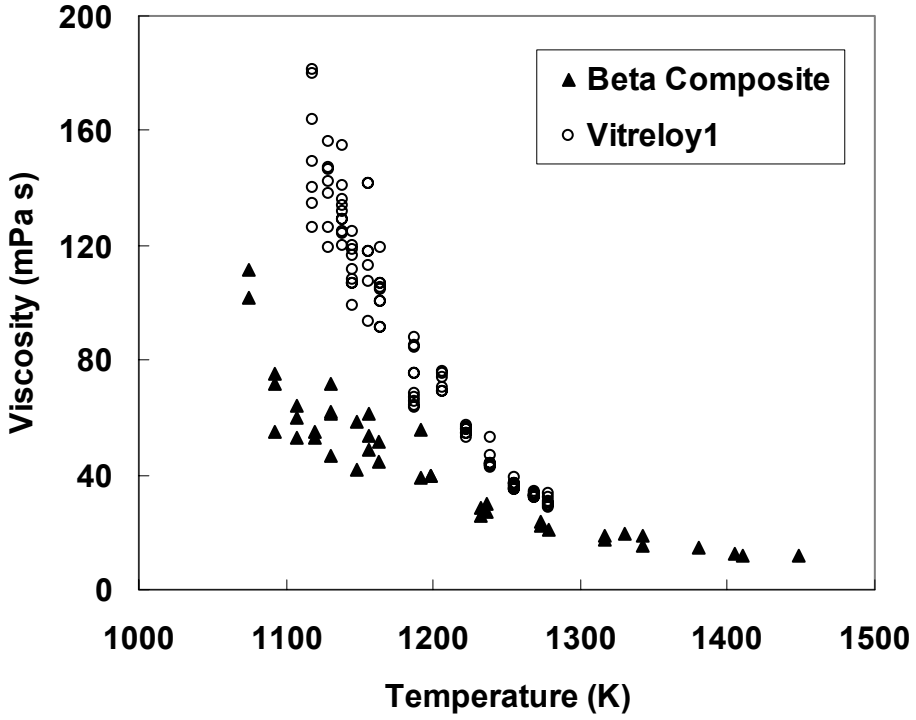

Figure 7.2: Viscosity of the β composite compared to Vit1. The viscosities were measured coming down from 1450 K down to 1080 K.

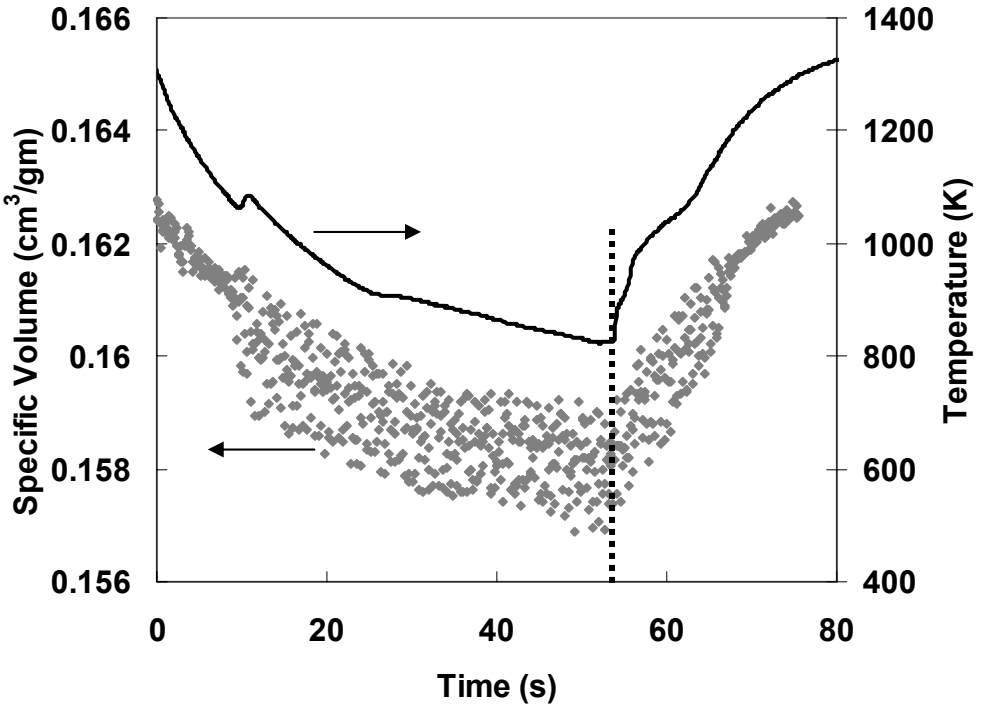

Figure 7.3: Cooling curve for overheating > 1420 K. The corresponding specific volume data is also shown. Two heat release events are evident from the cooling curve. The sample gets severely distorted after the first recalescence event, with no significant change in the noise level after the second recalescence.

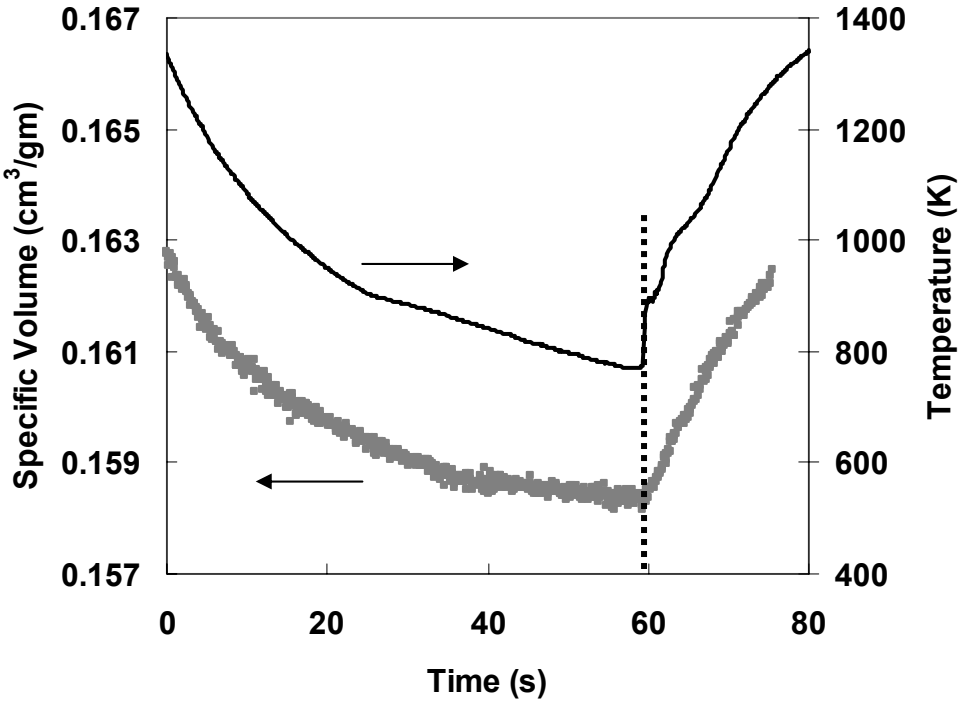

Figure 7.4: Cooling curve for overheating < 1420 K. The corresponding specific volume data is also shown. Only a single heat release event is evident from the cooling curve. The sample distortion is much less compared to the situation of overheating > 1420 K.

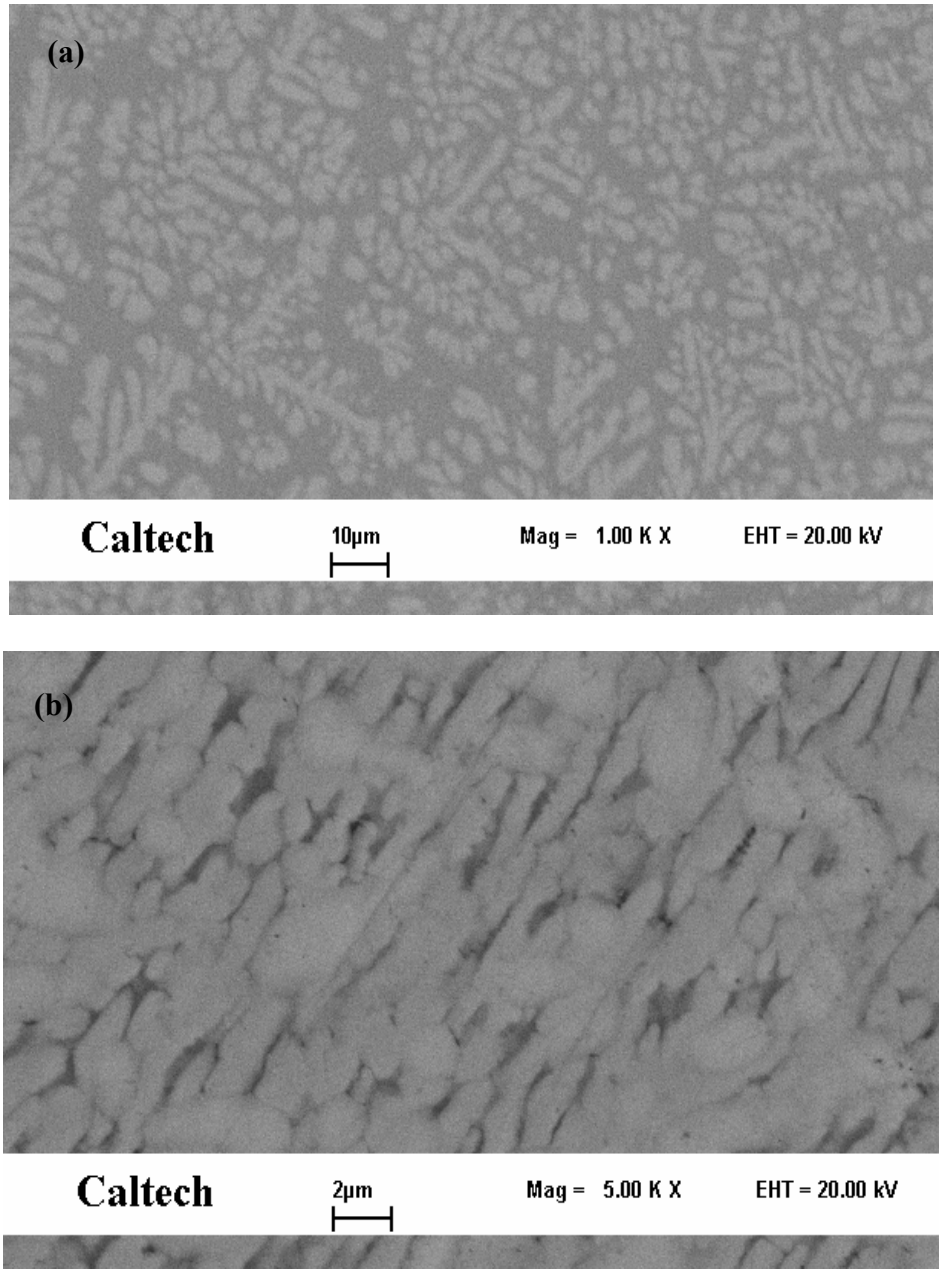

Figure 7.5: SEM back scattered images for samples cooled from (a) below 1420 K and (b) above 1420 K.

7.3 Conclusions

The following conclusions can be drawn from the ESL study of the *in situ* β composite, $Zr_{56.2}Ti_{13.8}Nb_{5.0}Cu_{6.9}Ni_{5.6}Be_{12.5}$, under different processing conditions:

(1) The melting point of the ductile β phase in the composite, which is much higher than the melting temperature of the matrix, is obtained from the viscosity measurements to be around 1420 K. The viscosity of the β composite, after melting of the β dendrites, is much lower than the best BMG investigated in this study, $Zr_{41.2}Ti_{13.8}Cu_{12.5}Ni_{10}Be_{22.5}$ (Vit1).

(2) Upon cooling the β composite from temperatures above 1420 K, β dendrites nucleate at a certain undercooling and result in severe distortion of the sample as seen from the volume measurements. The free radiative cooling curve shows two recalescence events: a sharp peak at 1055 K and a broad peak around 915 K. There is also non-uniform distribution of the β dendrites, as seen from the microstructure.

(3) Free radiative cooling from temperatures below 1420 K preserves the shape of the sample and results in uniform distribution of the β dendrites. There is only a single broad recalescence event during cooling, suggesting partial crystallization of the matrix. The partial crystallization of the matrix, however, causes only slight distortion of the sample.

(4) The knowledge of viscosity and the microstructure as a function of overheating temperature are important for optimization of processing conditions in

commercial applications. Heating the β composite above the β phase melting temperature will result in significant lowering of the melt viscosity, thus making it much easier for processing. However, cooling to room temperature should be followed by raising the melt to a temperature between the matrix and β phase melting points to ensure uniform distribution of the dendrites and less volume distortion.

7.4 References

[1] W. L. Johnson, MRS Bulletin **10**, 42 (1999).

[2] A. Inoue, Acta Mater. **48**, 279 (2000).

[3] C. C. Hays, C. P. Kim, and W. L. Johnson, Phys. Rev. Lett. **84**, 2901 (2000).

[4] C. P. Kim, Ph.D. Thesis, California Institute of Technology (2001).

[5] F. Szuecs, C. P. Kim, and W. L. Johnson, Acta Mater. **49**, 1507 (2001).

[6] J. Lu, G. Ravichandran, and W. L. Johnson, Acta Mater. **51**, 3429 (2003).

[7] S. Y. Lee, private communication.

APPENDIX

Non-Newtonian Viscosity Effects in Vit1

Among fluids, the one that shows the simplest constitutive behavior is a Newtonian fluid, in which strain rate is directly proportional to the applied stress. In such cases, viscosity is independent of the strain rate. However, viscosity of non-Newtonian fluids is shear rate dependent. The transition from Newtonian to non-Newtonian behavior of a fluid depends strongly on its temperature and strain rate. The mechanical behavior of metallic glasses can be classified as either inhomogeneous or homogeneous deformation. Inhomogeneous deformation typically occurs at temperatures way below the glass transition temperature (T_g) and is characterized by shear localization and catastrophic failure. On the other hand, homogeneous deformation which can be either Newtonian or non-Newtonian occurs at higher temperatures ($> 0.7T_g$) and the materials exhibit significant plasticity [1]. Recently, there is great interest in the study of homogeneous deformation of metallic glasses because commercial processing is typically done in this deformation regime.

The deformation behavior of a fluid changes from Newtonian to non-Newtonian when the internal structural relaxation is not able to keep up with the external loading rate. Non-Newtonian behavior has been experimentally observed for a number of metallic glasses at high strain rates. Kawamura *et al.* [2] studied the high temperature deformation behavior of $Zr_{65}Al_{10}Ni_{10}Cu_{15}$ metallic glass and attributed the non-Newtonian behavior to

the rapid deformation-induced free volume. Nieh *et al.* [1] investigated the plasticity of $Zr_{52.5}Cu_{17.9}Ni_{14.6}Al_{10}Ti_5$ (Vit105) and ascribed the non-Newtonian effects to the formation of nanocrystallites. The deformation behavior of $Zr_{41.2}Ti_{13.8}Cu_{12.5}Ni_{10}Be_{22.5}$ (Vit1) has been studied over a large range of strain rates and temperatures close to T_g by Lu *et al.* [3]. Johnson *et al.* [4] explained the non-Newtonian behavior of Vit1 by a dynamic model taking into account the rate of creation and annihilation of free-volume during flow. All of the experiments and models mentioned above are focused on the behavior close to T_g, while little is known about the behavior close to the melting temperature.

To investigate the possible influence of strain rate on the viscosity of glass forming alloys at high temperatures above the melting point, different oscillation frequencies were used for the alloys investigated in this study. To induce different resonance oscillations, samples of different sizes were used. The viscosities for Vit1 measured with two different resonance frequencies are shown in Figure A.1. The sample masses (69.6 mg and 23.9 mg) and the corresponding resonance frequencies are indicated in the figure. The frequency dependence of viscosity disappears above 1300 K. However, there is a clear diverging trend in viscosity below 1300 K. The viscosities are lower for measurements done with the higher resonance frequency of 270 Hz. Thus, higher strain rate of deformation leads to lowering of the viscosity of the liquid. A wider frequency range could not be investigated because of limits on the sample size that can be levitated in the HVESL. Figure A.2 shows the measurements done in the present study, together with the measurements done recently by Busch [5] using a Couette Viscometer with different strain rates (SR). A strong dependence of viscosity on strain rate is evident. The

strain rate in the Couette Viscometer can be accurately determined. However, an oscillating drop has a distribution of strain rates and it is difficult to ascertain it precisely. Therefore, only the resonance oscillation frequencies are indicated within the parentheses for the ESL measurements. The other alloys investigated in this study did not show behavior similar to Vit1.

Non-Newtonian behavior is observed for Vit1 at temperatures well above the melting temperature (up to 300 K above T_L in this case). The non-Newtonian behavior model for Vit1 [4], based on data close to T_g, predicts that at temperatures around 1200 K, a change from Newtonian to non-Newtonian behavior occurs at strain rates of the order of 10^8 s^{-1}. This is several orders of magnitude higher than those experimentally used in this study or by Busch [5]. This suggests that there may be additional relaxation phenomena which are not accounted for in the low temperature model. The stretching exponent used in the numerical models [4] should take into account the high temperature non-Newtonian behavior to simultaneously explain the results at glass transition as well as the melting temperature. Also, there may be deformation-induced structural changes in the Vit1 melt at high temperatures. Such changes may result in modification of the relaxation behavior. Systematic investigation with a wide range of strain rates and a wide variety of metallic glasses above their melting points is required to see if this behavior is limited to just Vit1 or is more prevalent. However, for the range in strain rate used during drop oscillation in the ESL, the other alloys investigated in this study did not show non-Newtonian behavior.

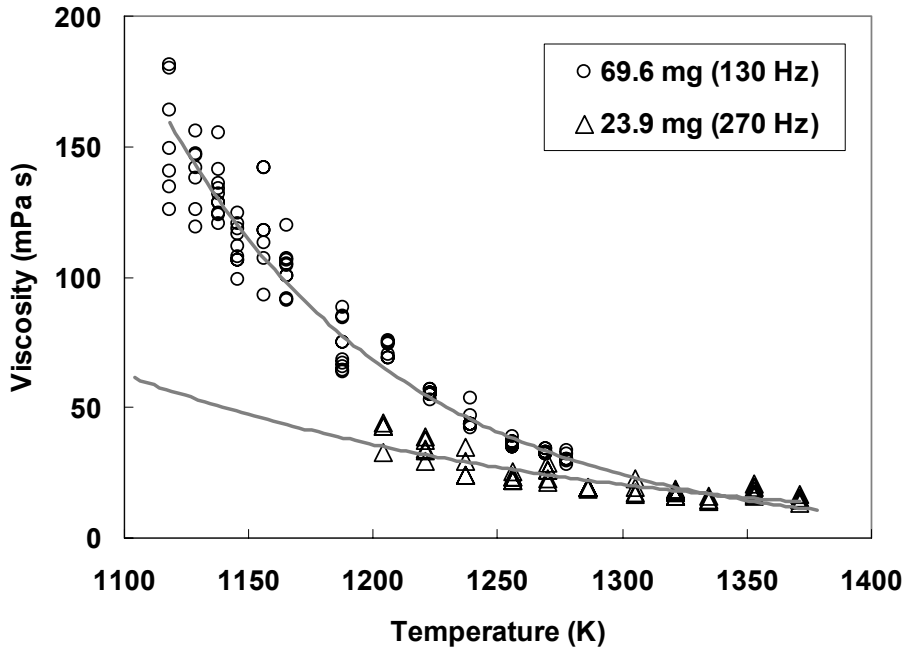

Figure A.1: Viscosity of $Zr_{41.2}Ti_{13.8}Cu_{12.5}Ni_{10}Be_{22.5}$ (Vit1) measured using the drop oscillation technique in ESL with two different resonance frequencies. The sample masses and the corresponding resonance frequencies are indicated. The viscosity is non-Newtonian below 1300 K for the strain rates used in drop oscillation.

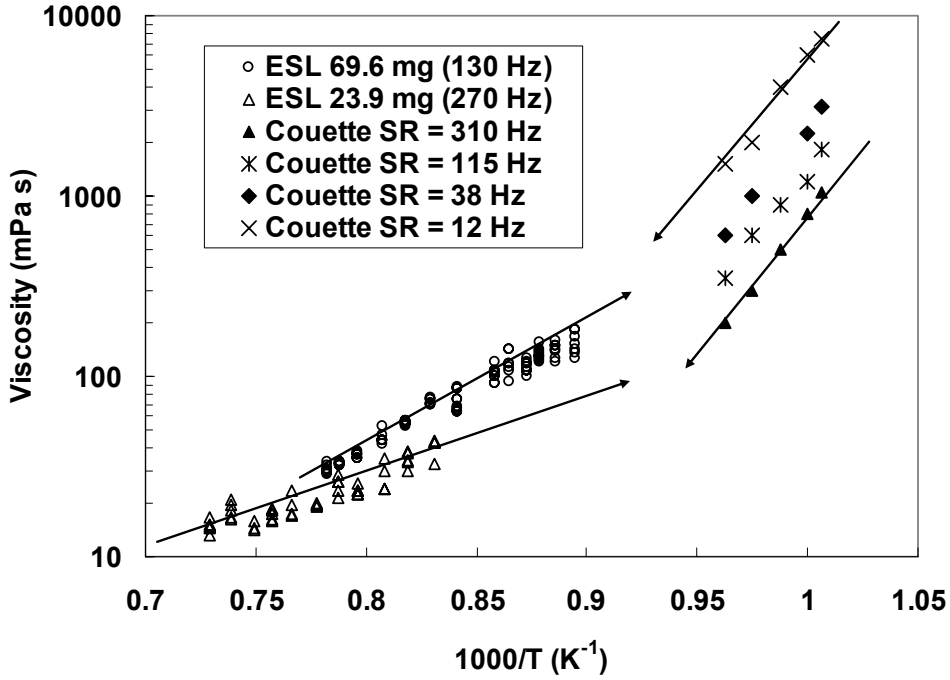

Figure A.2: Viscosities for $Zr_{41.2}Ti_{13.8}Cu_{12.5}Ni_{10}Be_{22.5}$ (Vit1) obtained in this study along with results obtained by Busch [5] using a Couette Viscometer at different strain rates (SR).

Appendix References

[1] T. G. Nieh, J. Wadsworth, C. T. Liu, T. Ohkubo, and Y. Hirotsu, Acta Mater. **49**, 2887 (2001).

[2] Y. Kawamura, T. Nakamura, and A. Inoue, Scripta Mater. **39**, 301 (1998).

[3] J. Lu, G. Ravichandran, and W. L. Johnson, Acta Mater. **51**, 3429 (2003).

[4] W. L. Johnson, J. Lu, and M. D. Demetriou, Intermetallics **10**, 1039 (2002).

[5] R. Busch, Private Communication.